Neutron Star Equations of State With a Phase Transition in a Relativistic Mean Field Approach at Finite Temperatures

Dissertation
zur Erlangung des Doktorgrades
der Naturwissenschaften

vorgelegt beim Fachbereich Physik
der Johann Wolfgang Goethe-Universität
in Frankfurt am Main

von
Jan-Erik Christian
aus Bad Homburg

Frankfurt am Main 2023
D30

Vom Fachbereich Physik der

Johann Wolfgang Goethe - Universität als Dissertation angenommen.

Dekan:	Prof. Dr. Roger Erb
Gutachter:	Prof. Dr. Jürgen Schaffner-Bielich Prof. Dr. Carsten Greiner
Datum der Disputation:	06.06.2023

Contents

List of Figures

List of Tables

1. Motivation

The sky and stars in particular have fascinated humanity since its very beginning. While cultures as ancient as the Babylonians tried to divine meaning from their constellation, modern humanity has not lost its interest in them, though the method in which we try to divine meaning has become more sophisticated. It is not their allurement alone that might motivate their investigation. An accurate description of matter under extreme circumstances, such as high temperatures and densities, is a highly coveted piece of information in multiple fields of physics. It is referred to as the equation of state (EoS) of high energy matter. The investigation of such matter comes with a plethora of complications not least of which is the creation of such extreme conditions in a terrestrial laboratory. While particle accelerators are a very successful method of investigating matter at high temperatures, the time frame in which this can be done is limited to the fractions of a second the particles collide, posing additional challenges. The high density regime is even harder to probe on earth.
One of the most promising remedies for our lack of knowledge in this regard is astrophysics. This is because high energy conditions that are impossible to achieve on earth are common place in the cosmos. Furthermore, most objects observed are stable and will not change much in a timescale relevant to us, especially in the case of neutron stars. Although it is difficult to precisely determine astrophysical observables with current technology next generation gravitational wave observatories like the Einstein telescope [Maggiore et al., 2020] and Cosmic Explorer [Evans et al., 2021] are likely to improve the constraints that can be put on the high density equation of state (EoS) drastically.

This thesis will aim to create an understanding of the place of neutron stars in the search for the description of high energy matter. A particular focus will be on so-called hybrid stars. To better illustrate how this thesis fits into the bigger picture of high energy physics we look at the phase diagram of quantum chromodynamics (QCD) in figure 1.1. It shows the state in which matter at high energies is observed and the corresponding

ways of probing its properties. As mentioned before, collider experiments like the Large Hadron Collider (LHC) at CERN or the Realistic Heavy-Ion Collider (RHIC) at the Brookhaven National Laboratory are well suited to investigate high temperature conditions at comparatively low densities.
It is well known that at high densities or temperatures a phase transition from the regular hadronic matter we are used to, to a quark-gluon plasma will take place. This is inevitable as it becomes energetically favorable for the quarks that make up hadrons to exist in a deconfined state under such extreme conditions. However, it is unknown where exactly this phase transition occurs and in what way. In particular, it is unknown, whether or not this phase transition is possible under conditions in the center of neutron stars. Determining the validity of this hypothesis would be an invaluable step in constraining the behavior of high energy matter.
In this thesis, we will explore the most important constraints provided by neutron star observations on the equation of state for ultra dense matter using a highly parameterizable description for the hadronic phase and an optimistic constant speed of sound approach for a potential quark phase. We are mostly concerned with possible indicators provided by current observables at low temperatures that might point towards the presence of a phase transition within neutron stars. However, we will also introduce some modifications to our hadronic description to expand our analysis to finite temperatures, which will allow us to investigate the mid-temperature region in the QCD phase diagram at the density of neutron stars via protoneutron stars or binary-merger simulations in the future.

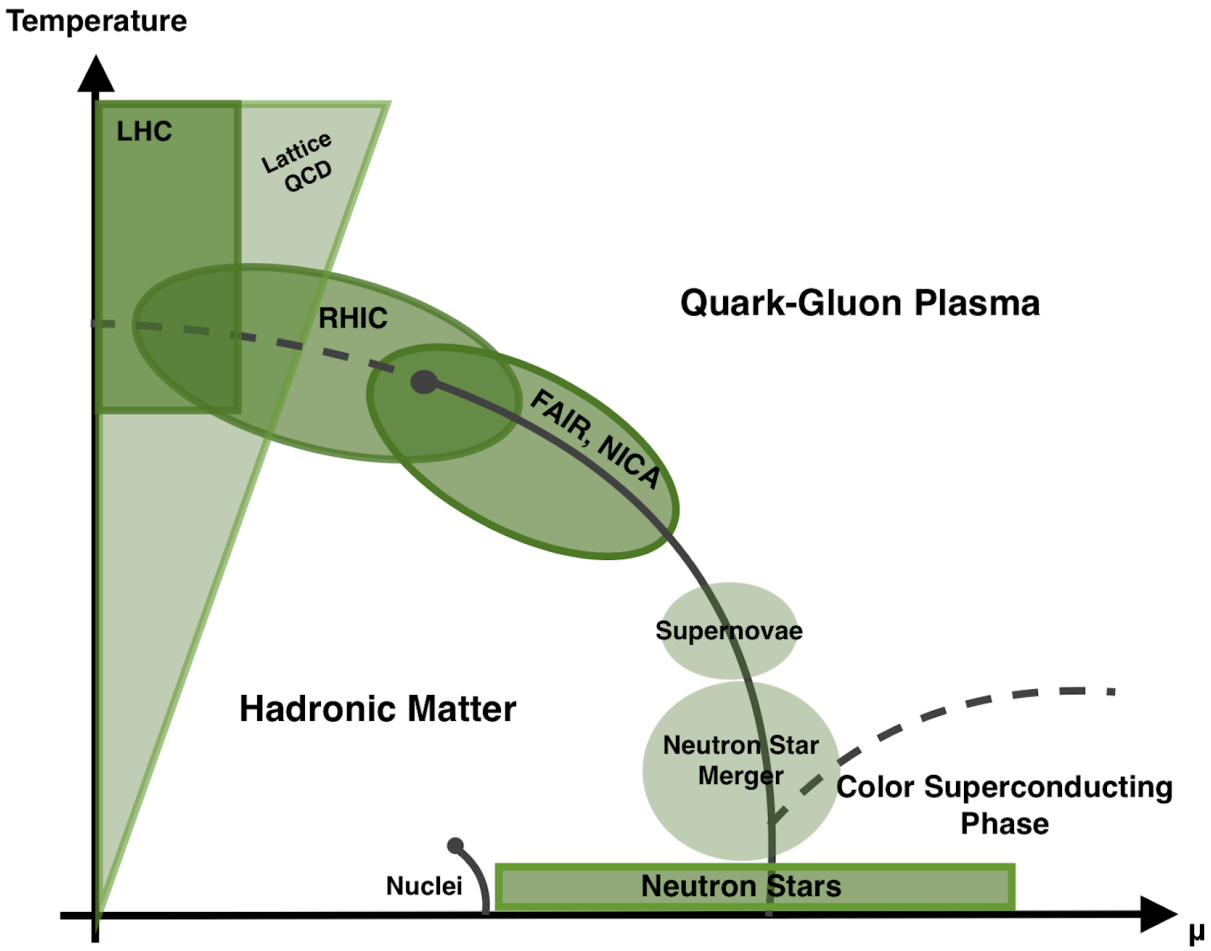

Figure 1.1.: A qualitative drawing of the temperature and baryon chemical potential axis of the QCD phase diagram. Methods of probing the border between hadronic and quark matter are shaded in green. The abbreviations are as follows: FAIR refers to the Facility for Antiproton and Ion Research at the GSI in Darmstadt and NICA refers to the Nucleon Based Ion Collider Facility being constructed in Dubna. The LHC is the Large Hadron Collider at CERN and RHIC the Relativistic Heavy-Ion Collider at Brookhaven.

2. Introduction

This thesis is structured in the following way: We will start in chapter 3 by examining the assumptions that go into our description of hadronic matter. The model we use is an equation of state that describes matter by modeling the interaction between particles as the exchange of mesons. It is a relativistic mean field equation of state [Johnson and Teller, 1955, Duerr, 1956, Walecka, 1974, Boguta and Bodmer, 1977, Serot and Walecka, 1986, Mueller and Serot, 1996, Typel et al., 2010, Hornick et al., 2018]. One of the main advantages of this type of EoS is its high parameterizability [Todd-Rutel and Piekarewicz, 2005, Chen and Piekarewicz, 2014, Hornick et al., 2018], allowing us to investigate a brought spectrum of the parameter space with a single consistent approach. We will construct this equation of state with the assumption of a negligible temperature and then expand it later in the chapter to finite temperatures.
Once we established the underlying hadronic equation, we can focus on neutron stars themselves in chapter 4. After a short summary of the field, the most common properties of a neutron star that can be calculated will be introduced and their derivation shown. This allows us to compare the results with state of the art astrophysical observables from NICER [Miller et al., 2019, Riley et al., 2019, Raaijmakers et al., 2019, Miller et al., 2021, Riley et al., 2021, Raaijmakers et al., 2021], LIGO/Virgo [Abbott et al., 2017, Abbott et al., 2018, Abbott et al., 2019, Abbott et al., 2020] and other groups [Demorest et al., 2010, Antoniadis et al., 2013, Fonseca et al., 2016, Cromartie et al., 2019, Romani et al., 2022, Doroshenko et al., 2022].
In chapter 5 we will introduce a phase transition into the hadronic equation of state, creating so-called hybrid stars [Ivanenko and Kurdgelaidze, 1965, Itoh, 1970, Alford et al., 2005, Coelho et al., 2010, Chen et al., 2011, Masuda et al., 2013, Yasutake et al., 2014, Zacchi et al., 2016]. They are referred to as such because they are part hadronic and part quark star. We will examine the influence a phase transition has on the previously discussed observables. Most notably the mass radius relation, where a strong indicator of a phase transition can be found in the form of twin stars; two stars with the

same mass but different radii [Kämpfer, 1981, Glendenning and Kettner, 2000, Schertler et al., 2000, Schaffner-Bielich et al., 2002, Zdunik and Haensel, 2013, Alford et al., 2015, Blaschke and Alvarez-Castillo, 2016, Zacchi et al., 2017, Alford and Sedrakian, 2017, Christian et al., 2018, Blaschke et al., 2020, Jakobus et al., 2021]. Such a configuration is only possible for neutron stars with a phase transition. We also will take the opportunity to discuss some topics that are only tangentially related to this work in chapter 5 when we take a look at production scenarios of hybrid stars and alternative explanations for potential data points.
We conclude in chapter 6 that given the current astrophysical data a phase transition in neutron stars is possible. We will see that, depending on the parameters under which this phase transition would take place[Christian et al., 2018, Christian and Schaffner-Bielich, 2021, Christian and Schaffner-Bielich, 2022], the presence of a phase transition in neutron stars will be either known or strongly constrained in the near future [Paschalidis et al., 2018, Alvarez-Castillo et al., 2019, Christian et al., 2019, Montana et al., 2019, Sieniawska et al., 2019, Christian and Schaffner-Bielich, 2020, Tsaloukidis et al., 2022, Landry and Chakravarti, 2022].

3. Our Equation of State

3.1. What is an Equation of State?

A fundamental concept in physics is the so-called equation of state (EoS). This equation describes the behavior of matter under specific conditions and assumptions. In astrophysics the EoS is generally displayed as the connection of pressure p and the energy density ϵ, for reasons that will become apparent in section 4.3. The most famous equation of state is most likely the ideal gas law ($pV = nRT$). In this famous case, it is assumed that the gas consists of point particles, that only interact with each other and the boundary via elastic collisions. However, this model is obviously insufficient in more complex or high density systems.
The equation of state of nuclear matter up to about saturation density n_0 is well constrained by terrestrial experiments [Li and Han, 2013, Lattimer and Lim, 2013, Roca-Maza et al., 2015, Hagen et al., 2015, Oertel et al., 2017, Birkhan et al., 2017] and effective theories [Machleidt and Entem, 2011, Gandolfi et al., 2012, Hebeler et al., 2013, Drischler et al., 2016], but the behavior at high densities is largely unknown. In theory, it is possible to constrain the equation of state using astrophysical observables, such as masses, radii and tidal deformation of neutron stars, which we will cover in great detail in later chapters. An aspect of the EoS that is of some importance to these constraints is the stiffness/softness of an equation of state. These terms refer to the increase of the binding energy per particle as a function of density. They are used as a tool for comparison between EoSs, where a stiff or hard equation of state has a stronger increase of the energy per particle than a soft one. This behavior can also be related to pressure and energy density, which are often more practical to use in astrophysics. A strong increase in pressure as a function of energy density would indicate a stiff equation of state.

In the following section, we will explore the intricacies of a particular high density equation of state that profits significantly from its ability to be parameterized and thus is capable of generating a good impression of the limits provided by a given constraint.

3.2. Relativistic Mean Field Equation of State

A relativistic mean field (RMF) equation of state is constructed by employing quantum field theory. It was first introduced by Johnson and Teller [Johnson and Teller, 1955], Duerr [Duerr, 1956] and Walecka [Walecka, 1974]. The general procedure involves deriving a Lagrangian containing all interactions necessary to reproduce nuclear matter. The specific interactions depend on the particles that are taken into consideration. The Lagrangian can then be used to find the equations of motion with the Euler-Lagrange formalism. From there it is possible to extract the equation of state. This formalism is described in multiple textbooks, see for an example specifically related to compact stars [Glendenning, 2000].
In a conventional relativistic mean field model the interaction between nucleons is described by including isovector ρ and isoscalar ω and σ mesons. The mesons are represented as Lorentz scalar fields σ and Lorentz vector fields ω_μ and $\vec{\rho}_\mu$, where σ is responsible for the long range attraction, ω_μ the short range repulsion and $\vec{\rho}_\mu$ the n/p asymmetry. Neutrons and protons can be understood as Dirac spinors $\psi_i (i = n, p)$. A Lagrangian can be found by combining the Lagrangians of the particles described, as well as their interaction terms. The free Lagrangian for baryons is given as:

$$\mathcal{L}_B = \overline{\psi}_B \left(i\gamma_\mu \partial^\mu - m_B \right) \psi_B \,, \tag{3.1}$$

with its mass m. The interaction Lagrangian for the mesons is described by employing the dimensionless coupling constants g_i with $i = \sigma, \omega, \rho$:

$$\mathcal{L}_{int} = \overline{\psi}_B \left(g_\sigma \sigma - g_\omega \gamma_\mu \omega^\mu - \frac{1}{2} g_{\vec{\rho}} \gamma_\mu \vec{\tau} \cdot \rho^\mu \right) \psi_B - \frac{1}{3} b m_n \left(g_\sigma \sigma \right)^3 - \frac{1}{4} c \left(g_\sigma \sigma \right)^4 \,, \tag{3.2}$$

where the last two terms describe the scalar self-interaction of the σ fields and $\vec{\tau}$ stands for the isospin Pauli matrices. Finally the free Lagrangians for the σ, ω and ρ mesons

are given as:

$$\mathcal{L}_\sigma = \frac{1}{2}\left(\partial_\mu\sigma\partial^\mu\sigma - m_\sigma^2\sigma^2\right), \tag{3.3}$$

$$\mathcal{L}_\omega = \frac{1}{2}m_\omega^2\omega_\mu\omega^\mu - \frac{1}{4}\omega_{\mu\nu}\omega^{\mu\nu}, \tag{3.4}$$

$$\mathcal{L}_\rho = \frac{1}{2}m_{\vec{\rho}}^2\vec{\rho}_\mu\cdot\rho^\mu - \frac{1}{4}\vec{\rho}_{\mu\nu}\cdot\vec{\rho}^{\mu\nu}. \tag{3.5}$$

Adding them up one finds a typical Lagrangian:

$$\begin{aligned}\mathcal{L} = &\sum_B \overline{\psi}_B\left(i\gamma_\mu\partial^\mu - m_B + g_{\sigma B}\sigma - g_{\omega B}\gamma_\mu\omega^\mu - \frac{1}{2}g_{\vec{\rho}B}\gamma_\mu\vec{\tau}\cdot\rho^\mu\right)\psi_B \\ &+ \frac{1}{2}\left(\partial_\mu\sigma\partial^\mu\sigma - m_\sigma^2\sigma^2\right) - \frac{1}{4}\omega_{\mu\nu}\omega^{\mu\nu} + \frac{1}{2}m_\omega^2\omega_\mu\omega^\mu \\ &- \frac{1}{4}\vec{\rho}_{\mu\nu}\cdot\vec{\rho}^{\mu\nu} + \frac{1}{2}m_{\vec{\rho}}^2\vec{\rho}_\mu\cdot\rho^\mu - \frac{1}{3}bm_n\left(g_\sigma\sigma\right)^3 - \frac{1}{4}c\left(g_\sigma\sigma\right)^4.\end{aligned} \tag{3.6}$$

This Lagrangian describes baryons with isovector ρ and isoscalar ω and σ mesons [Glendenning, 1985, Glendenning, 2000]. Unlike in DD RMF models (see for example [Typel et al., 2010]) the coupling constants g_σ, g_ω and g_ρ are not density dependent.
Following the work of previous groups [Serot and Walecka, 1986, Mueller and Serot, 1996, Hornick et al., 2018] we add the following interaction Lagrangian to the previous equation (3.6):

$$\mathcal{L}_{\text{int}} = \sum_N \overline{\psi}_i\left[-q_i\gamma^\mu A_\mu\right]\psi_i + \Lambda_\omega\left(g_\rho^2\vec{\rho}_\mu\vec{\rho}^\mu\right)\left(g_\omega^2\omega_\mu\omega^\mu\right) + \frac{\zeta}{4!}\left(g_\omega^2\omega_\mu\omega^\mu\right)^2, \tag{3.7}$$

with A_μ as the photon field. The interaction Lagrangian contains the additional term $-\overline{\psi}_i q_i\gamma^\mu A_\mu\psi_i$, as well as the last two terms describing a density dependence. This is accomplished with the density dependent $\rho-\omega$ coupling term Λ_ω and the quadratic self coupling ζ of the ω mesons [Mueller and Serot, 1996, Horowitz and Piekarewicz, 2001, Todd-Rutel and Piekarewicz, 2005].
With knowledge of the Lagrangian we can find the equations of motion for the participating fields and finally energy density ϵ and the pressure p.
The equations of motion for the nucleons can be obtained from the Dirac equation:

$$\left(i\gamma^\mu\partial_\mu - q_i\gamma^\mu A_\mu - m^* - g_\omega\gamma^0\omega_0 - \tfrac{g_\rho}{2}\tau_{3i}\gamma^0\rho_{3_0}\right)\psi_i = 0, \tag{3.8}$$

where $\tau_{3p} = +1$ and $m^* = m - g_\sigma\sigma$, the effective mass of the nucleon. The photons can be described using the Poisson equation, with the proton density as the source term. The mesonic equations of motion, which can be gained from the Euler-Lagrange equation, read as follows:

$$m_\sigma^2\overline{\sigma} + mbg_\sigma^3\overline{\sigma}^2 + cg_\sigma^4\overline{\sigma}^3 = g_\sigma n^s\,, \tag{3.9}$$

$$m_\omega^2\overline{\omega} + \frac{\zeta}{3!}g_\omega^4\overline{\omega}^3 + 2\Lambda_\omega g_\rho^2 g_\omega^2\overline{\rho}^2\overline{\omega} = g_\omega n\,, \tag{3.10}$$

$$m_\rho^2\overline{\rho} + 2\Lambda_\omega g_\rho^2 g_\omega^2\overline{\omega}^2\overline{\rho} = \frac{g_\rho}{2}n_3\,. \tag{3.11}$$

This is the point at which mean field theory earns its name. In high baryon density environments the meson fields can be replaced with their expectation values ($\overline{\omega} = \langle\omega\rangle$, $\overline{\sigma} = \langle\sigma^0\rangle$ and $\overline{\rho} = \langle\rho_3^0\rangle$), which enables us to simplify the otherwise highly complicated non-linear quantum field equations of motion. The quantities n and n^s represent the nuclear and scalar densities (i.e. the sum of the respective neutron and proton densities), while the quantity $n_3 = n_p - n_n$. The densities n_i and n_i^s can be defined as:

$$n_i = \frac{\gamma}{(2\pi)^3}\int_0^\infty d^3k\,\left[f(k) - f(\bar{k})\right]\,, \tag{3.12}$$

$$n_i^s = \frac{\gamma}{(2\pi)^3}\int_0^\infty d^3k\,\frac{m^*}{\sqrt{k^2+m^{*2}}}\left(f(k) + f(\bar{k})\right)\,, \tag{3.13}$$

with $f(k)$ being the distribution function depending on the momentum k and γ being the spin-isospin degeneracy. For now we will assume $T = 0$. Since the Fermi distribution behaves like a Heavyside-function at zero temperature with $\lim_{T\to 0} f(k) = \Theta(\mu - \epsilon(k))$ this simplifies to:

$$n_i^s = \frac{m^*}{2\pi^2}\left[E_{F_i}k_{F_i} - m^{*2}\ln\frac{k_{F_i}+E_{F_i}}{m^*}\right]\,, \tag{3.14}$$

$$n_i = \frac{k_{F_i}^3}{3\pi^2}\,, \tag{3.15}$$

where $E_{F_i} = \sqrt{k_{F_i}^2 + m^{*2}}$ is the Fermi energy and k_{F_i} the Fermi momentum. Lets now consider the energy-momentum tensor defined as:

$$T^{\mu\nu} \equiv \frac{\partial\mathcal{L}}{\partial(\partial_\mu\phi_i)}\partial^\nu\phi_i - \eta^{\mu\nu}\mathcal{L}\,. \tag{3.16}$$

With our Lagrangian and keeping in mind, that the meson fields are replaced with their expectation values this yields:

$$T^{\mu\nu} = i\bar{\psi}\gamma^{\mu}\partial^{\nu}\psi - [\frac{1}{2}m_{\omega}^{2}\bar{\omega}^{2} - \frac{1}{2}m_{\sigma}^{2}\bar{\sigma}^{2} + \frac{1}{2}m_{\rho}^{2}\bar{\rho}^{2} - \frac{1}{3}bm_{n}\left(g_{\sigma}\bar{\sigma}\right)^{3} - \frac{1}{4}c\left(g_{\sigma}\bar{\sigma}\right)^{4} + \Lambda_{\omega}\left(g_{\rho}g_{\omega}\bar{\rho}\bar{\omega}\right)^{2} + \frac{\zeta}{4!}\left(g_{\omega}\bar{\omega}\right)^{4}]\eta^{\mu\nu}. \tag{3.17}$$

The energy-momentum tensor of a perfect fluid of a uniform system can be expressed as:

$$T^{\mu\nu} = -p\eta^{\mu\nu} + (p+\epsilon)u^{\mu}u^{\nu}\,, \tag{3.18}$$

with u^{μ} the four-velocity. This means in the local rest frame the energy-momentum tensor can be depicted as:

$$T^{\mu\nu} = \begin{pmatrix} \epsilon & 0 & 0 & 0 \\ 0 & p & 0 & 0 \\ 0 & 0 & p & 0 \\ 0 & 0 & 0 & p \end{pmatrix}, \tag{3.19}$$

which then makes it easy to see, that we can express ϵ and p as:

$$\epsilon = \langle\bar{\psi}\gamma_{0}k_{0}\psi\rangle - \langle\mathcal{L}\rangle\,, \tag{3.20}$$

$$p = \langle\bar{\psi}\gamma_{i}k_{i}\psi\rangle + \frac{1}{3}\langle\mathcal{L}\rangle\,, \tag{3.21}$$

where we used that $i\partial_{\nu}\psi = k_{\nu}\psi$ and $\langle\mathcal{L}\rangle$ is the term in brackets of equation (3.17). Now we only need to determine $\langle\bar{\psi}\gamma_{0}k_{0}\psi\rangle$ and $\langle\bar{\psi}\gamma_{i}k_{i}\psi\rangle$ and we are done. We assume again zero temperature and find:

$$\langle\bar{\psi}\gamma_{0}k_{0}\psi\rangle = \frac{1}{\pi^{2}}\sum_{I_{3}}\int_{0}^{\infty}k^{2}dke(k)\Theta(\mu - e(k))\,, \tag{3.22}$$

where $e_{i}(k) = \left(g_{\omega}\bar{\omega} + g_{\rho}\bar{\rho}I_{3}\right)n_{i} + E(k))$ describes the eigenvalues of the Dirac operators for the particles i, which in our case are protons and neutrons. Furthermore, is $E_{i}(k) =$

$\sqrt{k^2+(m-g_\sigma\sigma)^2}$ the energy and I_3 the isospin. This means:

$$\begin{aligned}\langle\bar{\psi}\gamma_0 k_0\psi\rangle =&\frac{1}{\pi^2}\int_0^{k_{fp}} k^2 dk\left[(g_\omega\bar{\omega}+\frac{1}{2}g_\rho\bar{\rho})\,n_p+\sqrt{k^2+(m-g_\sigma\sigma)^2}\right]\\ &+\frac{1}{\pi^2}\int_0^{k_{fn}} k^2 dk\left[(g_\omega\bar{\omega}-\frac{1}{2}g_\rho\bar{\rho})\,n_n+\sqrt{k^2+(m-g_\sigma\sigma)^2}\right]\\ =&\frac{1}{\pi^2}\left[g_\omega\bar{\omega}\,n+\frac{g_\rho}{2}\bar{\rho}\,n_3+\sum_i\int_0^{k_{f_i}} k^2\sqrt{k^2+(m-g_\sigma\sigma)^2}dk\right].\end{aligned} \tag{3.23}$$

We used here that $n = n_n + n_p$ and $n_3 = n_p - n_n$. It is now possible to employ the equations of motion (3.9)-(3.11) to substitute n and n_3 and subtract $\langle\mathcal{L}\rangle$ from the result. This finally allows us to express the energy density:

$$\begin{aligned}\varepsilon=\langle\bar{\psi}\gamma_0 k_0\psi\rangle-\langle\mathcal{L}\rangle=&\sum_i\frac{1}{8\pi^2}\left[k_{F_i}E_{F_i}^3+k_{F_i}^3E_{F_i}-m^{*4}\ln\frac{k_{F_i}+E_{F_i}}{m^*}\right]\\ &+\frac{1}{2}m_\sigma^2\bar{\sigma}^2+\frac{1}{2}m_\omega^2\bar{\omega}^2+\frac{1}{2}m_\rho^2\bar{\rho}^2 l+\frac{1}{3}bm\,(g_\sigma\bar{\sigma})^3+\frac{1}{4}c\,(g_\sigma\bar{\sigma})^4\\ &+\frac{\zeta}{8}\,(g_\omega\bar{\omega})^4+3\Lambda_\omega\left(g_\rho g_\omega\bar{\rho}\bar{\omega}\right)^2.\end{aligned} \tag{3.24}$$

For the pressure we proceed analogously and find:

$$\langle\bar{\psi}\gamma\mathbf{k}\psi\rangle=\frac{1}{\pi^2}\sum_i\int_0^{k_{f_i}}\frac{k^4}{\sqrt{k+m^*}}dk\,, \tag{3.25}$$

which then again can be used to find an expression for the pressure. Alternatively, one could use the connection of pressure and energy density to determine the former using:

$$p=\sum_i\mu_i n_i-\varepsilon\,, \tag{3.26}$$

where μ_i is the chemical potential of particle i with:

$$\mu_i=E_{f_i}+g_\omega\bar{\omega}+\frac{g_\rho}{2}\tau_{3i}\bar{\rho}\,. \tag{3.27}$$

3.3. Parameterization

In the previous section, we found expressions for the pressure and energy density. If one now desires to actually use these equations, they will find, that there is a significant amount of parameters that have not been fixed yet. RMF equations of state are phenomenological models, where the parameters have to be fitted to experimental nuclear data. Most notably the meson coupling constants g_σ, g_ω and g_ρ, but also the $\omega - \sigma$ coupling Λ_ω, quadratic self coupling of the ω mesons ζ and other parameters can be derived from nuclear matter properties such as the saturation density n_0, the binding energy per nucleon E/A, the incompressibility coefficient K and the effective nucleon mass m^*/m at saturation.
There are various constraints on this large list of parameters, especially because many of them are closely interlinked. For a recent study pertaining to these values in the framework of a relativistic mean field equation see [Ghosh et al., 2022].
The isoscalar coupling constants (g_σ, g_ω, b and c) can be determined by fixing n_0 as well as E/A, K and m^*/m. For a detailed description of this calculation see for example [Glendenning, 2000]. In the EoS used here we fix $n_0 = 0.16\ \mathrm{fm}^{-3}$, $E/A(n_0) = -16.3\,\mathrm{MeV}$ and $K(n_0) = 240\,\mathrm{MeV}$ unless mentioned otherwise. This is based on [Shlomo et al., 2006] and within the accepted values reported in [Oertel et al., 2017].
Furthermore, we follow the procedure described in [Chen and Piekarewicz, 2014] to fix the isovector couplings (g_ρ and Λ_ω) as a function of symmetry energy J and the slope of the symmetry energy L at saturation density. Note that we set the quadratic ω meson coupling $\zeta = 0$, which generates the stiffest equation of state. The density-dependent symmetry energy can be expressed as:

$$S(n) = S_0(n) + S_1(n) = \frac{k_F^2}{6E_F} + \frac{g_\rho^2 n}{8m_\rho^{*2}}\,, \tag{3.28}$$

$$\text{with}\ \ \frac{m_\rho^{*2}}{g_\rho^2} = \frac{m_\rho^2}{g_\rho^2} + 2\Lambda_\omega g_\omega^2 \bar{\omega}^2 \tag{3.29}$$

and $S_0(n)$ and $S_1(n)$ as the isoscalar and isovector. Since all isoscalar parameters have been fixed, $S_0(n)$ and its derivatives are known. However, $S_1(n)$ is unknown as g_ρ and Λ_ω are not determined yet. It is known, that $J = S(n_0)$ and $L = 3n_0 \left(\frac{dS}{dn}\right)_0$, which we

can use. We start with J:

$$
\begin{aligned}
J &= S(n_0) = J_0 + J_1\,, && (3.30)\\
J_0 &= S_0(n_0) = \left(\frac{k_F^2}{6E_F}\right)_0\,, && (3.31)\\
J_1 &= S_1(n_0) = \left(\frac{g_\rho^2 n}{8m_\rho^{*2}}\right)_0\,. && (3.32)
\end{aligned}
$$

For a given effective mass at saturation density, we can compute J_0, which yields J_1 as well, since we fix J. The slope parameter L can be written as

$$
L = 3n_0\left(\frac{dS}{dn}\right)_0 = L_0 + L_1\,, \tag{3.33}
$$

where

$$
\begin{aligned}
L_0 &= 3n_0\left(\frac{dS_0}{dn}\right)_0 = 3n_0\left[\left(\frac{\partial S_0}{\partial n}\right) + \left(\frac{\partial S_0}{\partial m^*}\right)\left(\frac{\partial m^*}{\partial n}\right)\right]_0\,,\\
L_1 &= 3n_0\left(\frac{dS_1}{dn}\right)_0 = 3n_0\left[\left(\frac{\partial S_1}{\partial n}\right) + \left(\frac{\partial S_1}{\partial \bar{\omega}}\right)\left(\frac{\partial \bar{\omega}}{\partial n}\right)\right]_0\,. && (3.34)
\end{aligned}
$$

This can be recast, as shown in [Chen and Piekarewicz, 2014], as:

$$
L_0 = J_0\left\{1 + \frac{m^{*2}}{E_F^2}\left[1 - \frac{3n}{m^*}\left(\frac{\partial m^*}{\partial n}\right)\right]\right\}_0\,, \tag{3.35}
$$

with

$$
\left(\frac{\partial m^*}{\partial n}\right) = -\frac{m^*}{E_F}\left[\frac{m_{\sigma^*}^2}{g_{\sigma^*}^2} + \frac{\partial n^s}{\partial m^*}\right]^{-1} \tag{3.36}
$$

and

$$\begin{aligned} \frac{m_{\sigma^*}^2}{g_\sigma^2} &= \frac{m_\sigma^2}{g_\sigma^2} + 2\,b\,m\,g_\sigma\,\bar{\sigma} + 3\,c\,g_\sigma^2\,\bar{\sigma}^2\,, \\ \frac{\partial n^s}{\partial m^*} &= \frac{1}{\pi^2}\left[\frac{k_F}{E_F}\left(E_F^2 + 2m^{*2}\right) - 3\,m^{*2}\ln\left(\frac{k_F + E_F}{m^*}\right)\right]. \end{aligned} \tag{3.37}$$

As one can see all parameters contributing to L_0 are known and fixed. This leaves L_1:

$$L_1 = 3J_1\left[1 - 32\left(\frac{g_\omega^2}{m_\omega^{*2}}\right) g_\omega\,\bar{\omega}\,\Lambda_\omega\,J_1\right]_0, \tag{3.38}$$

with $m_\omega^* = m_\omega$. With L, L_0 and L_1 it is easy to calculate Λ_ω. Using Λ_ω we can find g_ρ by combining equations (3.38), (3.29) and (3.32):

$$\frac{g_\rho^2}{m_\rho^2} = \left[\frac{n}{8J_1} - 2\Lambda_\omega g_\omega^2 \bar{\omega}^2\right]_0^{-1}. \tag{3.39}$$

3.4. Effects of Parameter Variation

One of the biggest advantages of the relativistic mean field approach is also one of its greatest downsides. The EoS is highly parameterizable and can include a variety of interactions and particles. In our model, the ability to vary the equation of state's stiffness is at the forefront of our consideration, which we accomplish by varying the effective masses at saturation density (see section 3.3). We therefore keep the complexity of the Lagrangian at a minimum and only include neutrons, protons, electrons, muons and their anti particles, as outlined in the construction of our Lagrangian in section 3.2, and disregard more exotic possibilities like hyperons or delta mesons. This leaves us with the symmetry energy J, the slope parameter L and the effective mass as input parameters for our equation of state. It has been known for some time that the stiffness of an equation of state is related to the effective mass at saturation density, where small values of m^*/m lead to stiff EoSs and high values to soft ones [Boguta and Stöcker, 1983].

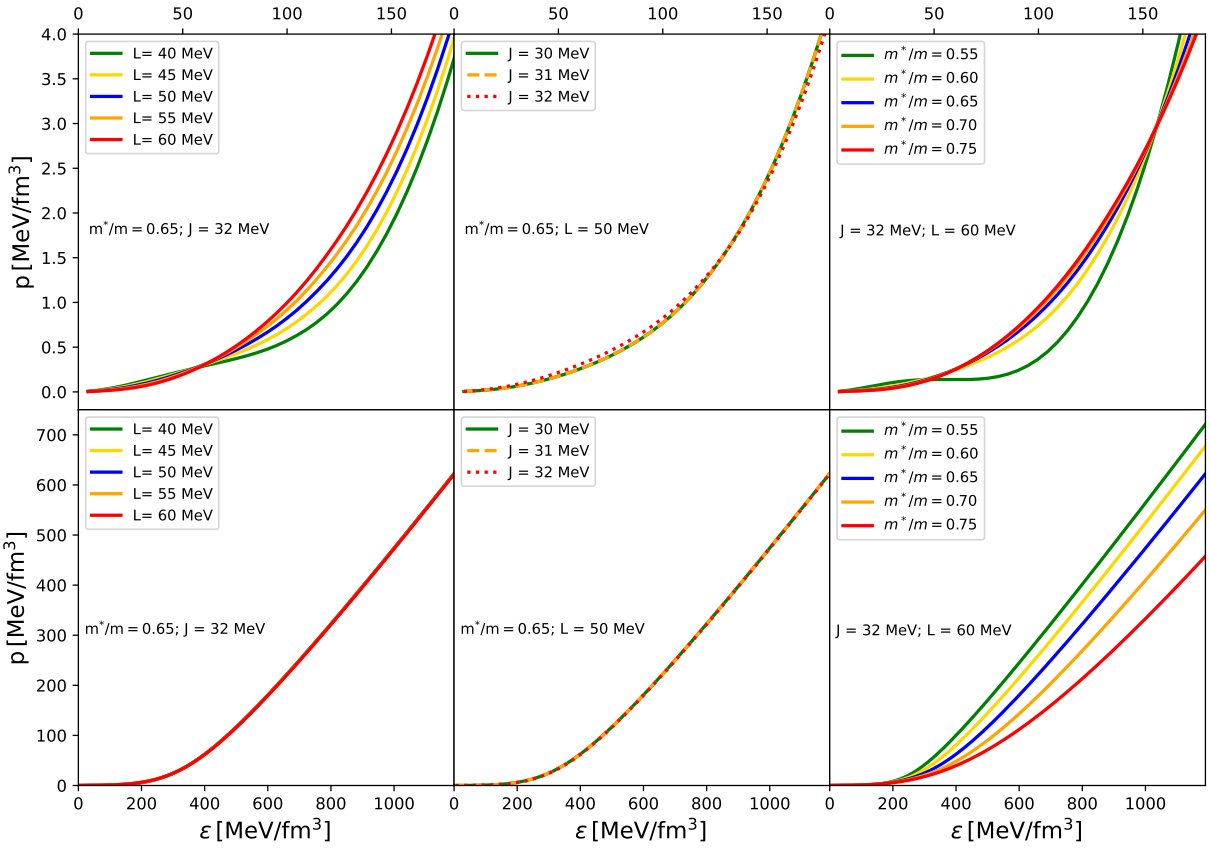

Figure 3.1.: The effects of changing the parameters J, L and m^*/m on the equation of state are shown, where one parameter is varied, and the other two are kept constant. The upper three plots are at small pressures close to saturation density. The bottom plots show the range that is relevant at the core of neutron stars, which is significantly denser. The variation of J shows no significant effect on the EoS in any regime, while L causes a visible change at small densities but has little effect in the full range. The only parameter variation that causes the EoS to significantly change at high densities is m^*/m, which varies the stiffness.

With the slope parameter L being constraint to values of about $L = 40 - 60$ MeV and the symmetry energy to values of $J = 30 - 32$ MeV [Li and Han, 2013, Lattimer and Lim, 2013, Roca-Maza et al., 2015, Hagen et al., 2015, Oertel et al., 2017, Birkhan et al., 2017, Adhikari et al., 2022, Zhang and Chen, 2022] the effective mass has the greatest range of values in our approach. We vary it in steps of 0.05 from $0.55 - 0.75$, though it should be noted that usually the best fit to nuclei is accomplished for values around $m^*/m = 0.61 \pm 0.03$ [Furnstahl and Serot, 2000]. Shirke et al. [Shirke et al., 2022] published a very insightful recent study on this RMF EoS, where they investigate the constraints using multidisciplinary physics. The values we use in this thesis are within their allowed parameters.

The effects on the EoS of varying our three parameters are shown in figure 3.1. In this figure, the upper three subplots show the pressure as a function of the energy density in the small density range close to saturation density and the whole range required for neutron star calculation in the bottom three plots. For each plot, one parameter is varied while the others stay constant. From the middle plot, it is clear that varying the symmetry energy in such small intervals has little effect on the equation of state. This is true for both density regimes. This is in contrast to the difference generated by varying the effective mass in the right two plots. At low densities effective masses fixed to small values generate EoS with smaller pressure values at the same energy density than higher effective masses. This behavior changes at saturation density. As can be seen in the bottom right, changing the effective mass at saturation density has a large impact on the equation of state at high densities. This leaves the variation of L in the two sections on the left. Like the J variation, there is no impact on the equation of state at high densities from changing L. This is reflected in the fact that L does not effect the maximal mass of an equation of state significantly [Tolos et al., 2017a, Tolos et al., 2017b] and has little effect on the mass radius relation of neutron stars as a whole [Hornick et al., 2018]. However, at low densities close to saturation density L has a distinct influence on the equation of state, where small values of L soften the equation of state. This makes L a crucial parameter when fitting the equation of state to low density constraints (see section 3.5).

When discussing the stiffness of the model, the quadratic self coupling of the ω mesons ζ should be mentioned as well. In this work, we set $\zeta = 0$, which leads to stiff equations of state. However, it is well known even small values of ζ soften the EoS drastically. From astrophysical constraints this puts an upper bound of 0.03 on ζ as Pradhan et al. [Pradhan et al., 2023] show. The difference between those two methods of controlling

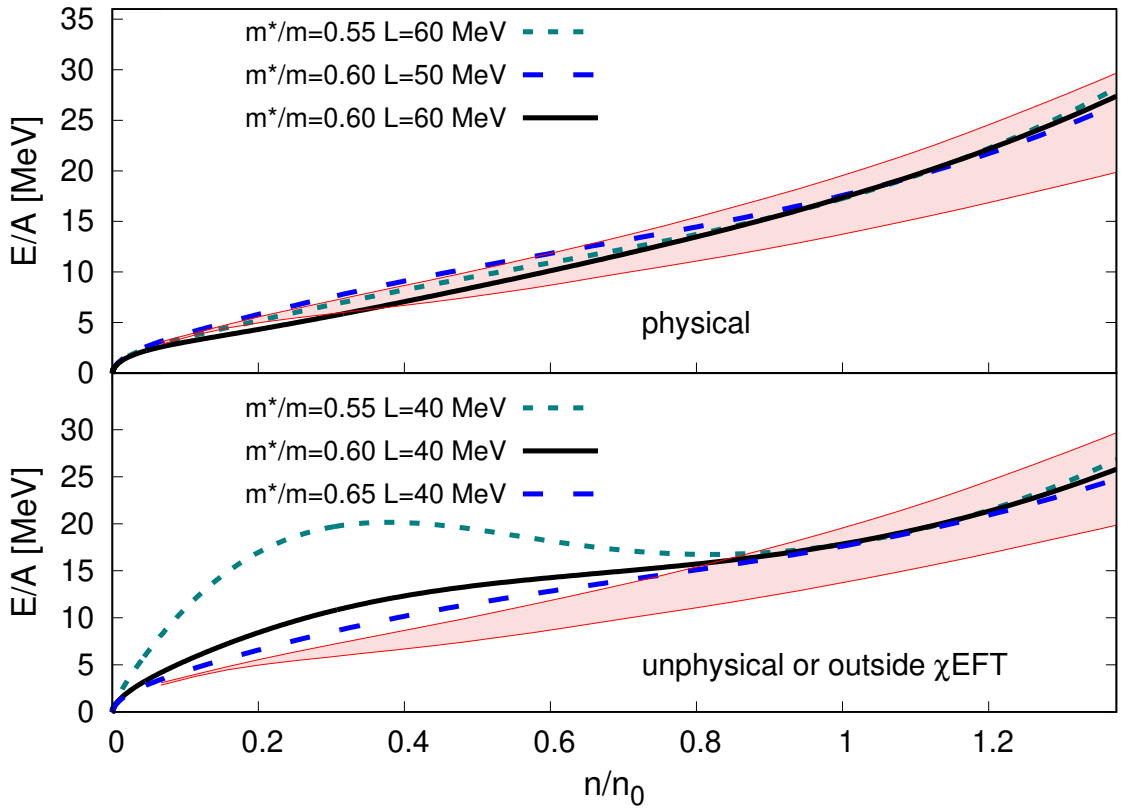

Figure 3.2.: χ_{EFT} constraints compared to some choice examples of parameter sets. The upper plot shows cases where all constraints are met, the lower plot shows cases that do not fit χ_{EFT} or are unphysical. The symmetry energy is set to $J = 32$ MeV, the slope parameter and effective masses are stated in the plot. This figure was published in [Hornick et al., 2018].

the stiffness of an EoS can be seen in the mass radius diagram, where non-zero ζ mass radius relations feature similar radii and only diverge at higher central pressures, while the softening caused by the effective mass also leads to a visible softening of the mass-radius relation (see figure 4.1), where the mass radius relation diverge sooner.

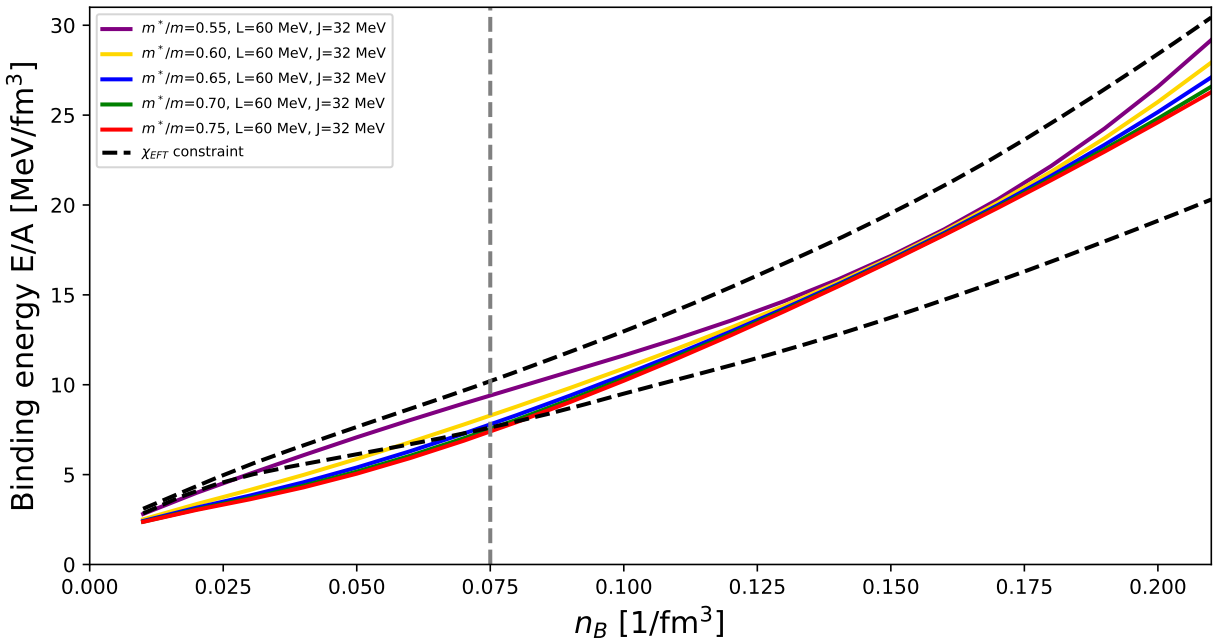

Figure 3.3.: χ_{EFT} limits compared with the RMF parameter sets we will use for the majority of this work. The gray dashed line indicates the end point of the crust EoS. Note that the RMF part after the crust is completely within χ_{EFT} predictions.

3.5. Low Density Constraints on the Hadronic Equation of State

Later in this work, we will discuss astrophysical constraints on the equation of state in great detail. However, these constraints are most useful in a high density region. We therefore need additional constraints to ensure that the equation of state describes the low density region as well. Very generally speaking, there are two main ways in which low density constraints are put on the equation of state. Firstly, there are constraints from terrestrial experiments like finite nuclei data. Observables such as nuclei masses, excitations and nuclear resonances can be determined with high accuracy. With these parameters it is possible to constrain parameters at saturation density, like the binding energy and the symmetry energy, as well as the value of n_0 itself, which usually ranges from $n_0 \approx 0.15 - 0.16$ [Oertel et al., 2017]. In the relativistic mean field approach, these parameters are used to calculate the coupling constants (as seen in section 3.3). This way, the RMF EoS is compatible with finite nuclei constraints by construction. We orient our values on the range deemed acceptable in the work by Oertel et al. [Oertel et al.,

2017], who provide a detailed overview over various constraints on the equation of state of compact stars.

The second main method of constraining the equation of state at low densities is the consideration of pure neutron matter. Due to the low temperature, it is possible to describe neutron matter using an effective field theory instead of the much more resource intensive lattice QCD, which becomes necessary at higher energies. For this effective theory, the breaking of chiral symmetry in the QCD Lagrangian is considered and gives upper and lower limits on the band describable by χ_{EFT}. For χ_{EFT} pions and nucleons are used as degrees of freedom instead of the quarks and gluons one would expect for a theory dealing with strong interactions. The χ_{EFT} Lagrangian is constructed by taking the most general QCD Lagrangian containing the broken symmetries. This dictate a soft and a hard scale based on the pion mass and the ρ meson mass. The QCD Lagrangian obviously would contain an infinite number of components, therefore only the most impactful terms are taken into account when constructing the χ_{EFT} Lagrangian. This is a complex task that numerous groups are working on. Usually pion-neutron (πN), two body nucleon (NN) and further interactions are considered to different degrees of order. We cannot scratch the surface of this topic here, as it is a vast field. Many more ab initio approaches exist to describe nuclear matter up to about saturation density. A very helpful review of the field from 2011 that also describes some of the underlying concepts was compiled by Machleid and Entem [Machleidt and Entem, 2011].

For our model, we fit the EoS to the next-to-next-to-next-to leading order three nucleon interaction N^{3}LO NNN constraints calculated by Drischler et al. [Drischler et al., 2016]. This fit was done in our publication [Hornick et al., 2018] where the parameters J, L and m^*/m were varied as discussed in section 3.4. The publication by Drischler et al. [Drischler et al., 2016] provides the χ_{EFT} results for the binding energy of neutron matter as a function of the particle density. These constraints are visualized in figure 3.2 for a selection of parameter sets. The upper examples are within the χ_{EFT} band and physically sound. The bottom plot contains results that are either unphysical or do not fit the χ_{EFT} constraint. In this context unphysical refers to equations of state with negative pressure. Hornick et al. provide an overview over the possible parameter sets that result in χ_{EFT} compliant EoSs, which are summarized in table 3.1 and 3.2. Here the abbreviations u, n and y are used for unphysical, not compatible and compatible solutions. One might notice that unphysical solutions only appear at $m^*/m = 0.55$ and even for those cases only for small slope parameters. This can likely be attributed to

L [MeV]	40	45	50	55	60
$m^*/m = 0.55$	u	u	n	y	y
$m^*/m = 0.60$	n	y	y	y	n
$m^*/m = 0.65$	y	y	y	y	n
$m^*/m = 0.70$	y	y	y	y	n
$m^*/m = 0.75$	y	y	y	y	n

Table 3.1.: Compatibility of $J = 30\,\text{MeV}$ parameter sets with chiral effective field theory results form [Drischler et al., 2016]. The abbreviation u, n and y indicate a unphysical, not fitting and fitting solution respectively. A slope parameter of $L = 55\,\text{MeV}$ allows all effective masses.

the Hugenholtz-van-Hove theorem [Boguta and Stöcker, 1983, Boguta, 1981] which states: the Fermi energy at saturation has to be equal to the binding energy per nucleon. This means, if we set the effective mass at saturation density to small values the ω field has to strengthen and the equation of state has to stiffen. As established in section 3.4 lowering L softens the EoS. This means the stiffening of the lowered effective mass and the softening from lowering L compete with each other, leading to unphysical solutions. We can further tell from tables 3.1 and 3.2 that there are only two combinations of J and L that support the entire range of effective masses. Since we are interested in investigating the effects of varying the EoS stiffness, which is tied to the effective mass, it is most useful for us to employ one of these sets. We therefore set $J = 32\,\text{MeV}$ and $L = 60\,\text{MeV}$ for the remainder of the work, unless stated otherwise. The EoS for varied effective masses with these parameters are compared to the χ_{EFT} band in figure 3.3. Apart from the $m^*/m = 0.55$ all EoS are slightly outside the constraint at low densities. However, this is not a concern as the deviation is acceptable. Furthermore, when we start investigating astrophysical constraints in the next chapter, we will employ a crust equation of state up to about half saturation density. This point is indicated by a gray dashed line in figure 3.3 at which all equations of state are wholly within the constraints.

L [MeV]	40	45	50	55	60
$m^*/m = 0.55$	u	u	u	n	y
$m^*/m = 0.60$	n	n	y	y	y
$m^*/m = 0.65$	n	y	y	y	y
$m^*/m = 0.70$	y	y	y	y	y
$m^*/m = 0.75$	y	y	y	y	y

Table 3.2.: Analogous to table 3.1 with $J = 32\,\text{MeV}$. A slope parameter of $L = 60\,\text{MeV}$ allows all effective masses.

3.6. Extending to Finite Temperatures

In cooled down neutron stars the Fermi momentum is much larger than the temperature, as a result it is sufficient to use an equation of state at zero temperatures for their description. However, shortly after a supernova, the newly born neutron star is still extremely hot and not yet in equilibrium. For these so-called protoneutron stars, it is necessary to consider the effect on the temperature as well. This is also true for neutron star mergers, where immense heat is generated in the inspiral. In order to extend our equation of state to finite temperatures, we need to reconsider the particle contributions for the included particles. If we consider the distribution function at finite temperatures, it does not reduce to a Heavyside-function at k_F like in section 3.2. Instead, we have to integrate over the entire parameter space.
We start with the pressure contribution for particle i and its corresponding antiparticle, which we have to solve. It can be expressed as:

$$p_i = \frac{\gamma_i}{3(2\pi)^3} \int_0^\infty dk^3 \frac{k^2}{E(k)} (f(k) - f(\bar{k}))\,, \tag{3.40}$$

where $f(k)$ is the distribution function. In our case we have fermions and therefore use the Fermi distribution:

$$f(k) = \left[e^{\frac{\sqrt{k^2+m^{*2}}-\mu^*}{T}} + 1 \right]^{-1}, \tag{3.41}$$

$$f(\bar{k}) = \left[e^{\frac{\sqrt{k^2+m^{*2}}+\mu^*}{T}} + 1 \right]^{-1}. \tag{3.42}$$

Here T is the temperature, m^* the effective mass of the particle and $\mu^* = \mu + B(g_\omega \bar{\omega} \pm g_\rho \bar{\rho})$ the effective chemical potential with the baryon number B.
This means equation (3.40) reads explicitly:

$$p_i = \frac{\gamma_i 4\pi}{3(2\pi)^3} \int_0^\infty dk \frac{k^4}{E(k)} \left(\left[e^{\frac{E(k)-\mu^*}{T}} + 1 \right]^{-1} - \left[e^{\frac{E(k)+\mu^*}{T}} + 1 \right]^{-1} \right) , \tag{3.43}$$

where we used, that the energy is $E(k) = \sqrt{k^2 + m^{*2}}$ and integrated over the angles. We now substitute $x = (E(k) - \mu^*)/T$, which leads to $k^2 = (xT + m^*)^2 - m^{*2}$, allowing us to simplify k in the following way:

$$k = \sqrt{x^2T^2 + 2xTm^*} = \sqrt{2xTm^*} \sqrt{\frac{1}{2}\frac{T}{m^*}x + 1} = \sqrt{2m^*T}\sqrt{x}\sqrt{1 + \frac{1}{2}\beta x} . \tag{3.44}$$

We used the relation $\beta = \frac{T}{m^*}$ here. Furthermore, we find:

$$\begin{aligned} \frac{dx}{dk} &= \frac{k}{T\sqrt{k^2 + m^{*2}}} , \\ dk &= dx \frac{\sqrt{k^2 + m^{*2}}}{k} T = dx \frac{E}{k} T , \\ E &= \sqrt{k^2 + m^{*2}} = xT + m^* . \end{aligned} \tag{3.45}$$

Inserting this substitution in equation (3.43) we find:

$$p_i = \frac{\gamma_i}{6\pi^2} \int_0^\infty dx\, k^3 T \left(\left[e^{x + \frac{m^*}{T} - \frac{\mu^*}{T}} + 1 \right]^{-1} - \left[e^{x + \frac{m^*}{T} + \frac{\mu^*}{T}} + 1 \right]^{-1} \right) \tag{3.46}$$

We now define $\eta = (\mu^* - m^*)/T$ and $\bar{\eta} = (\mu^* + m^*)/T$, which gives us:

$$p_i = \frac{\gamma_i}{6\pi^2} \int_0^\infty dx \left(\sqrt{2m^*T}\sqrt{x}\sqrt{1 + \frac{1}{2}\beta x} \right)^3 T \left[\frac{1}{exp(x - \eta) + 1} - \frac{1}{exp(x - \bar{\eta}) + 1} \right] \tag{3.47}$$

$$= \frac{\gamma_i}{6\pi^2} T \int_0^\infty dx \left(2m^*Tx \left(1 + \frac{1}{2}\beta x \right) \right) \sqrt{2m^*T}\sqrt{x}\sqrt{1 + \frac{1}{2}\beta x} \left[f(x, \eta) - f(\bar{x, \eta}) \right] \tag{3.48}$$

$$= \frac{\gamma_i m^{*4} \beta^{\frac{5}{2}}}{3\pi^2} \int_0^\infty dx \left(x^{\frac{3}{2}} + \frac{\beta}{2} x^{\frac{5}{2}} \right) \sqrt{1 + \frac{1}{2}\beta x} \left[f(x, \eta) - f(\bar{x, \eta}) \right] . \tag{3.49}$$

In this last step we replaced all instances of T with β and simplified the remaining expressions. This equation is numerically solvable. It is especially useful, that the addends are so similar. Gong et al. [Gong et al., 2001] provide a suitable numerical method of solving the following integral:

$$F_{\mathrm{k}}(\eta,\beta) = \int_0^\infty \frac{x^{\mathrm{k}}\sqrt{1+\frac{\beta}{2}x}}{\exp(x-\eta)+1}\,dx\,, \tag{3.50}$$

which is the well known Fermi-Dirac integral. It can be identified with the addends in equation (3.49). Note that $k \neq \mathrm{k}$, as k is the momentum and k is an index. Now we can write p_i as a numerically solvable expression:

$$p_i = \frac{m^{*4}}{\pi^2}\frac{\gamma_i\sqrt{2}}{3}\beta^{\frac{5}{2}}\left[\left(F_{3/2}(\eta,\beta)+\frac{\beta}{2}F_{5/2}(\eta,\beta)\right)-\left(F_{3/2}(\bar{\eta},\beta)+\frac{\beta}{2}F_{5/2}(\bar{\eta},\beta)\right)\right]. \tag{3.51}$$

Analogously, we can find the expressions for the energy density, scalar density and vector density at finite temperatures, which results in the following equations:

$$\begin{aligned} n &= \frac{\gamma}{2\pi^2}\int_0^\infty dk\,k^2\left[f(k)-f(\bar{k})\right] \\ &= \frac{\gamma\sqrt{2}}{2\pi^2}m^{*3}\beta^{\frac{3}{2}}\int_0^\infty dx\left[(\beta F_{3/2}(\eta,\beta)+F_{1/2}(\eta,\beta))-(\beta F_{3/2}(\bar{\eta},\beta)+F_{1/2}(\bar{\eta},\beta))\right], \end{aligned} \tag{3.52}$$

$$\begin{aligned} n^s &= \frac{\gamma}{(2\pi)^3}\int_0^\infty d^3k\frac{m^*}{\sqrt{k^2+m^{*2}}}\left(f(k)+f(\bar{k})\right) \\ &= \frac{\gamma\sqrt{2}}{2\pi^2}m^{*3}\beta^{\frac{3}{2}}\int_0^\infty dx\left[F_{1/2}(\eta,\beta)+F_{1/2}(\bar{\eta},\beta)\right], \end{aligned} \tag{3.53}$$

$$\begin{aligned} \epsilon_i = \frac{4m^{*4}}{\sqrt{2}\pi}\beta^{\frac{5}{2}}\Big[&\left(F_{3/2}(\eta,\beta)+\frac{\beta}{2}F_{5/2}(\eta,\beta)+\beta^{-1}F_{1/2}(\eta,\beta)\right) \\ &+\left(F_{3/2}(\bar{\eta},\beta)+\frac{\beta}{2}F_{5/2}(\bar{\eta},\beta)+\beta^{-1}F_{1/2}(\bar{\eta},\beta)\right)\Big]. \end{aligned} \tag{3.54}$$

For all these equations the substitution $x = (E(k)-\mu^*)/T$ was used.

3.7. Thermal Index for Relativistic Mean Field Results

With the extension to finite temperatures complete, we can investigate the effect of varying the effective mass at saturation density on the behavior of the equation of state with increasing temperature. A relevant quantity in this regard is the thermal index Γ_{th}, which can be defined as:

$$\Gamma_{th} = 1 + \frac{p_{th}}{\epsilon_{th}}, \tag{3.55}$$

where p_{th} is the thermal pressure contribution and ϵ_{th} the thermal contribution to the energy density, i.e.:

$$p(T) = p(T=0) + p_{th}, \tag{3.56}$$
$$\epsilon(T) = \epsilon(T=0) + \epsilon_{th}. \tag{3.57}$$

Γ_{th} can be identified with the adiabatic index for an ideal gas and has a value of $5/3$ in the non-relativistic regime. The value for an ultra-relativistic ideal gas is $4/3$. It is expected that the thermal index of our relativistic mean field equation of state remains close to these values ($5/3$ at low and $4/3$ at high densities) but does not match them exactly, as we are not assuming an ideal gas. In Figure 3.4 these limits are indicated with dashed gray lines. The thermal index for three different effective masses is shown, with two temperatures each. In all cases the thermal index approaches $4/3$ asymptotically for high densities and is close to $5/3$ at smaller densities. The green lines indicating a temperature of 20 MeV have higher maxima than the red lines indicating 50 MeV. Although not shown in this figure we investigated the behavior of $0 - 50$ MeV cases and noticed that this trend holds true where smaller temperatures generate higher Γ_{th} at their peak. It is further noticeable that smaller effective masses, i.e. stiffer EoSs, lead to higher maximal values of Γ_{th} as well. This is in line with our expectation, since the pressure of a stiff EoS increases faster with the energy density than in a soft EoS, which implies $(p/\epsilon)_{\text{stiff}} > (p/\epsilon)_{\text{soft}}$.

The equations of state thus far were all constructed under the assumption of β equilibrium, where $\mu_n = \mu_p + \mu_e$ holds. However, this assumption is only valid for comparatively small temperatures and when one considers for example protoneutron stars it is often necessary to abandon β equilibrium and explicitly set the proton fraction Y_p to a specific value, instead. This is not a result of the high temperatures themselves, but

a result of the short timescale at which protoneutron stars and neutron star mergers operate. In this time β equilibrium cannot be established as the dynamical timescale is much shorter than the equilibrium timescale. The proton fraction is the percentage of positively charged baryonic particles, in most cases:

$$Y_p = \frac{n_p}{n_B} = \frac{n_p}{n_p + n_n}, \quad \text{with the proton/baryon/neutron densities } n_{p/B/n}. \tag{3.58}$$

In addition to the thermal index in β equilibrium, the Γ_{th} for constant $Y_p = 10\%$ and $Y_p = 50\%$ are shown in figure 3.4, for the different effective masses and temperatures. We find that an increase in Y_p leads to a smaller deviation from the 5/3 ideal gas estimate. In other words: higher proton fractions lead to smaller Γ_{th}, if the proton fraction is fixed for the entire EoS. However, the thermal index of the equation of state in β equilibrium appears to be smaller than the thermal index for any explicitly set Y_p. This is surprising, as the proton fraction in β equilibrium is close to about 0.1 for the majority of the EoS, especially for small temperatures and one would therefore expect the Γ_{th} in β equilibrium to behave similarly as the $Y_p = 10\%$ case. In figure 3.5 we take a look at the proton fraction as a function of density for different temperatures in β equilibrium. The same effective masses as in figure 3.4 are used. At high densities all EoSs approach a value of about 0.15, but at low densities the influence of the temperature becomes apparent. Hot matter has a significantly higher proton fraction than cold matter at low densities. This is because at low densities the electron chemical potential is much smaller than the temperature. This means the EoS is dominated by thermal equilibrium and charge neutrality is not a large concern. When the density increases, so does the electron chemical potential and accordingly the proton fraction drops. The lowest temperature where the proton fraction at low densities exceeds Y_p at high densities is the $T = 30\,\text{MeV}$ case. Even though the proton fraction in β equilibrium at $T = 20\,\text{MeV}$ never has values larger than 0.15, the thermal index of this EoS is noticeably below the $Y_p = 0.5$ case for fixed proton fraction.

However, it should be noted that our results for the β equilibrium case are in line with similar works using a relativistic mean field equation, like Kochankovski et al. [Kochankovski et al., 2022]. This is shown in the right-hand plot of figure 3.6, where the EoS in β equilibrium used by Kochankovski et al. is shown in red and compared with our results for $m^*/m = 0.65$ in green. The peaks of both equations of state are at the same value of Γ_{th}, with our EoS featuring a slightly narrower curve, owing to the different approaches. The figure also includes the $Y_p = 0.2$ and $Y_p = 0.4$ cases found by

Kochankovski et al., as dashed and dotted red lines, respectively. These EoSs exhibit the same behavior seen in our equations, where a fixed Y_p generates higher Γ values than the β equilibrium case.
A possible explanation for this phenomenon can be found when looking at the thermal contributions from pressure and energy density separately. This is done in the left and center plot of figure 3.6 for the $m^*/m = 0.65$ case at $T = 20\,\mathrm{MeV}$. For fixed proton fraction, the pressure contribution p_{th} increases notably with the increase of Y_p, which can be seen by comparing the orange line ($Y_p = 0.5$) with the blue line ($Y_p = 0.1$.) This is not the case for the β equilibrium (green line) where the proton fraction is higher than $Y_p = 0.1$, but p_{th} is smaller than in the fixed $Y_p = 0.1$ case. In contrast, the thermal contribution to the energy density always increases with increased Y_p. Here, the β equilibrium case contributes a larger value of ϵ_{th} than the $Y_p = 0.1$ case. This could explain why the thermal index in β equilibrium is smaller than for fixed proton fraction. An even more in depth investigation of the causes for the increased pressure contribution for the explicitly set Y_p cases, as well as comparisons with other approaches, such as temperature dependent χ_{EFT} results [Carbone and Schwenk, 2019, Keller et al., 2022] has to be postponed to future works. Nevertheless, this equation of state explored here should be usable for protoneutron star and neutron star merger simulations with minimal adjustments.

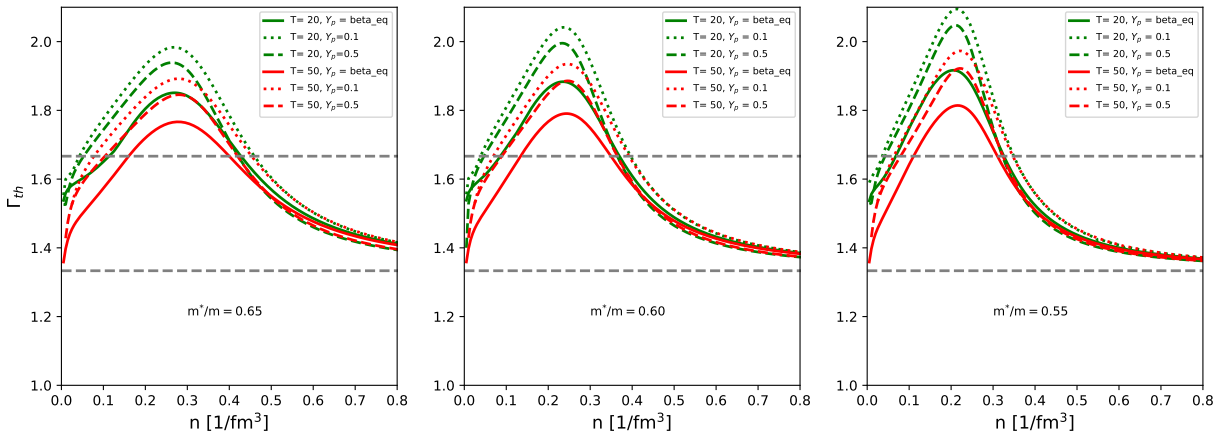

Figure 3.4.: From left to right: Decreasing effective masses at saturation density. The green lines indicate a temperature of 20 MeV, the red lines indicate 50 MeV. The proton fraction Y_p is varied, where smaller values of Y_p lead to larger peaks. If Y_p is not fixed to a specific value β equilibrium is assumed (continuous lines), which results in a lower peak, even though the proton fraction in β equilibrium is small.

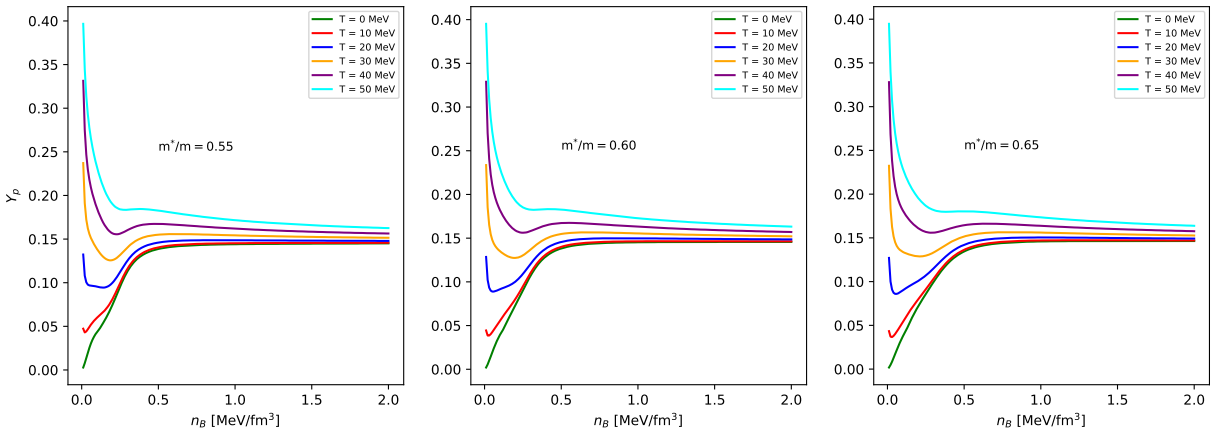

Figure 3.5.: The proton fraction Y_p in β equilibrium as a function of the baryon density n_B for temperatures from $T = 0 - 50$ MeV. All cases approach a value of about 0.15 at high densities, but increased temperatures lead to much larger proton fractions at small densities.

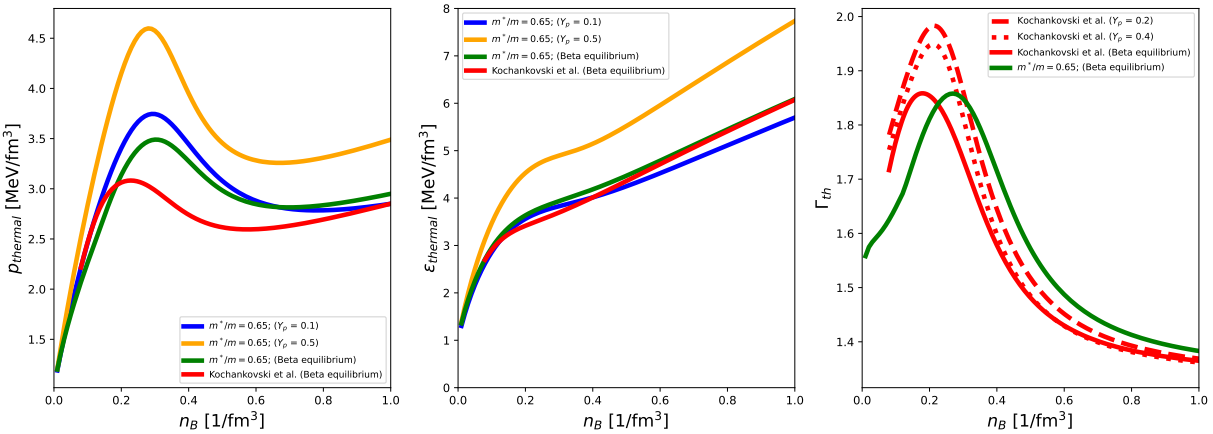

Figure 3.6.: Left: The thermal contribution to the pressure for the $m^*/m = 0.65$ in β equilibrium and for fixed Y_p case at $T = 20$ MeV. Additionally, the β equilibrium case of Kochankovski et al. [Kochankovski et al., 2022] is shown for comparison. Center: The thermal contribution ϵ_{th} for the same cases. Right: Comparison between the Γ_{th} in β equilibrium EoS of [Kochankovski et al., 2022] with the $m^*/m = 0.65$ case, as well as the behavior of fixed proton fraction in the EoS of [Kochankovski et al., 2022].

4. Neutron Stars

4.1. What are Neutron Stars?

Neutron stars are compact celestial objects that are produced by main sequence stars undergoing a supernova. In fact, neutron stars are the densest objects in the known universe, disregarding black holes. In contrast to the latter, neutron stars still contain ordinary matter. Main sequence stars are stabilized by their thermal pressure, which is generated by nuclear fusion. Once no more fusion material is left, the dense core of the star collapses, since the gravitational pull has no counteracting force. For particularly high masses of the initial star (about 20 $M_\odot$ or more) this collapse cannot be stopped, in which case the star will end as a black hole. Less massive stars can be stabilized through various processes. The least massive stars ($M_{inital} \lesssim 8M_\odot$) collapse to white dwarfs, which are kept in hydro static equilibrium by the degeneracy pressure of the electrons. This pressure is caused by the Pauli principle, which states that two fermions cannot occupy the same state in a system. Neutron stars are the remnants of stars that fill the gap between those that result in black holes and white dwarfs. A useful summary on neutron star core collapse supernovae can be found here [Cerdá-Durán and Elias-Rosa, 2018].
The high densities during a core collapse supernova cause the electrons to be absorbed by protons in the nuclei, increasing their neutron richness. Once a stable neutron and proton ratio for a certain density is reached, we achieved β equilibrium. The neutron fraction per nucleon increases with the density until a critical density is reached at about $4 \times 10^{11} g cm^{-3}$. Here, no additional neutrons can be bound. This causes a so-called neutron drip, resulting in a neutron liquid that surrounds the nuclei. This critical density would be considered "astronomically" high on earth; however, in a neutron star it is already reached about 0.1 km below the surface. Unlike white dwarfs, neutron stars cannot be stabilized by degeneracy pressure alone. Instead, hydrodynamic equilibrium

is kept by the repulsive interaction of the nuclei as well as the Pauli principle acting on the neutron liquid.
A particularly important type of neutron star are pulsars. These **puls**ating **r**adio sources emit extremely regular radio signals. They are powered by their fast rotation and due to them emitting radio waves are the only type of neutron star we can observe. The precision of a pulsars rotation period is astonishing and has been used to define standard time [Hobbs et al., 2012] with results comparable to atomic clocks.
Pulsars are the only type of neutron star with a detectable signal. Despite not directly observing them, this is enough to enables us to determine their masses, if they are found in a binary system. Here, the trajectory of pulsars companion can be used to calculate its mass. Especially binary systems containing two neutron stars yield masses to a very high degree of certainty, as we will see in subsection 4.4.1. Neutron star radii are much harder to determine, because they are too compact to directly observe. As a result, other effects such as luminosity observations or gravitational light deflections have to be used to estimate the radii in some form. This can be accomplished for example by utilizing hot spots on the neutron star surface, as we discuss in subsection 4.4.2. In any case, it is possible to put a theoretical upper limit on the mass of a neutron star, in analogy to the famous Chandrasekhar mass for white dwarfs. Depending on the mass of its original star, it ranges from 2-3 $M_\odot$. This is supported by astrophysical observations, where multiple stars with at least 2 $M_\odot$ are known [Demorest et al., 2010, Antoniadis et al., 2013, Fonseca et al., 2016, Cromartie et al., 2019]. It is also possible to put a lower limit on the mass of neutron stars. This is due to the production scenario of neutron stars that require the supernova of a massive main sequence star. This limit is in the range of about one solar mass [Ozel et al., 2012, Ozel and Freire, 2016, Müller et al., 2019, Suwa et al., 2018]. Some good resource for an introduction to compact star physics are [Glendenning, 2000, Sagert et al., 2006, Schaffner-Bielich, 2020].
The extreme conditions in a neutron star make them ideal to investigate the equation of state in an ultra dense regime. While the compactness of neutron stars is what makes them attractive for equation of state research, it also poses a significant hurdle. This is because neutron stars are too compact to be observed directly, with their radii ranging from about 10 km to 15 km. It is possible to make precise calculations of mass, radius and other quantities with only the equation of state and general relativity as underlying assumptions. This will be shown in section 4.3. In theory, this assumed equation of state could then be verified or falsified by comparing the precisely calculated quantities to the known astrophysical constraints. However, current technology is severely limited in

acquiring most astrophysical parameters, apart from mass. This means, that the amount of equations of state not ruled out by the data is still vast. Despite these difficulties, there have been significant recent advancements in observing neutron star quantities by numerous mass measurements (see sections 4.4.1) or groups such as NICER (see section4.4.2) and LIGO/Virgo (see section 4.4.3). In the near future, astrophysical constraints are expected to be more robust, especially with the third generation of gravitational wave detectors like the Einstein telescope [Maggiore et al., 2020] and Cosmic Explorer [Evans et al., 2021] on the horizon. This dynamic between constantly improving data and the constraints that can be obtained from it makes compact star science a very active field, but it is worth taking a short look at its history before we continue with its current state.

4.2. A (Very) Short History of Neutron Stars

Unlike many other astrophysical phenomena, neutron stars were conceptualized long before their first detection. In 1932 Landau published an article about the maximal mass of dense objects [Landau, 1932]. At the time, this only encompassed white dwarfs. However, the article contained an idea for stars that are similar to giant atomic nuclei. Rosenfeld [Rosenfeld, 1974] recalls a discussion between Bohr and Landau in 1932 in Copenhagen, allegedly shortly after the discovery of the neutron was reported. This has led to the assumption, that there is a correlation between these two publications. However, there is evidence, that the conversation between Landau and Bohr already took place in 1931 (see the article by Yakovlev et al. for a detailed examination of this history [Yakovlev et al., 2012].). The term neutron star was first coined by Baade and Zwicky [Baade and Zwicky, 1934b, Baade and Zwicky, 1934a], who suggested the collapse of a massive star to a neutron star as the cause of a supernova. Neutron stars were further investigated by Oppenheimer and Volkoff, who worked together with Tolman using general relativity. They determined the maximal mass of neutron stars to be $0.7 M_\odot$, assuming of a spherical object composed of a free fermion gas [Oppenheimer and Volkoff, 1939, Tolman, 1939]. The equations of state became more sophisticated by assuming a mixture of nuclei, electrons and a free Fermi gas of neutrons in beta equilibrium. By using the Skyrme model for the interaction of the nuclei [Skyrme, 1958], Cameron [Cameron, 1959] could increase the maximal mass drastically to $2.0 M_\odot$. There

are many more important models with different predictions, which we will not cover here. Again, we refer the reader to relevant textbooks like [Schaffner-Bielich, 2020], which contains a more in depth, but still brief review of the history of neutron stars. After the concept of a neutron star as the origin of a supernova was theorized for at least 35 years, the first pulsar was discovered in 1967 by Jocelyn Bell-Burnell [Hewish et al., 1968], who at the time was a Ph.D. student in the group of Anthony Hewish. The regularity of the observed signal was so precise, that an intelligent origin, i.e. extraterrestrials, was suspected at first. This led to them referring to the object as LGM, little green men, jokingly. The signal was discovered in the crab nebular, the position of which can be related to an event in the year 1054, where a "guest star" was recorded by Japanese and Chinese observers [Duyvendak, 1942]. This "guest star" was very likely the light from the supernova resulting in the pulsar discovered by Bell-Burnell.

4.3. Neutron Star Quantities Calculated with the Equation of State

The three most commonly used quantities to constrain the equation of state of neutron stars are mass M, radius R and tidal deformability Λ. The former two can be calculated by solving the Tolman–Oppenheimer–Volkoff (TOV) equations, which describe a spherically symmetric and non-rotating star in general relativity. The TOV equations will be derived in the next subsection. The tidal deformability can be determined by solving a second order differential equation alongside the TOV equations, this procedure will be explained in subsection 4.3.2. A rudimentary understanding of general relativity on the reader's part is assumed. We use geometrized units with $c = G = M_\odot = 1$.

4.3.1. Mass and Radius

In this subsection, the TOV equations will be derived. They follow directly from general relativity and produce the mass and radius of a relativistic star with a given central pressure $p_{central}$. Furthermore, they require an equation of state connecting pressure and

energy density. A more in depth derivation of the TOV equations than is to follow can be found in most related textbooks, such as [Glendenning, 2000] or [Schaffner-Bielich, 2020]. We start by considering the scalar curvature:

$$R = g^{\mu\nu}R_{\mu\nu} = e^{-2\nu}R_{00} - e^{-2\lambda}R_{11} - \frac{2}{r^2}R_{22} \tag{4.1}$$

$$= e^{-2\lambda}(-2\nu'' + 2\lambda'\nu' - 2\nu'^2 - \frac{2}{r^2} + 4\frac{\lambda'}{r} - 4\frac{\nu'}{r}) + \frac{2}{r^2}\,. \tag{4.2}$$

For convenience Einsteins field equation can be displayed with mixed tensors, for example:

$$G_0{}^0 = R_0{}^0 - \frac{1}{2}R = kT_0{}^0\,. \tag{4.3}$$

This leads to the entries of the Einstein tensor:

$$r^2G_0{}^0 \equiv e^{-2\lambda}(1 - 2r\lambda') - 1 = -\frac{d}{dr}[r(1 - e^{-2\lambda})]\,, \tag{4.4}$$

$$r^2G_1{}^1 \equiv e^{-2\lambda}(1 - 2r\nu') - 1\,, \tag{4.5}$$

$$G_2{}^2 \equiv e^{-2\lambda}(\nu'' + \nu'^2 - \lambda'\nu' + \frac{\nu' - \lambda'}{r})\,, \tag{4.6}$$

$$G_3{}^3 \equiv G_2{}^2\,. \tag{4.7}$$

By assuming a static star the energy-momentum tensor simplifies to the following nonzero entries:

$$T_0{}^0 = \epsilon \text{ and } T_\mu{}^\mu = -p \text{ where } \mu \neq 0\,, \tag{4.8}$$

with ϵ being the energy density and p the pressure, using this information on (4.4) one finds:

$$r^2G_0{}^0 = -\frac{d}{dr}[r(1 - e^{-2\lambda})] = kr^2T_0{}^0 = kr^2\epsilon(r)\,. \tag{4.9}$$

This expression can be integrated in order to yield:

$$e^{-2\lambda(r)} = 1 + \frac{k}{r}\int_0^r \epsilon(r)r^2dr\,. \tag{4.10}$$

By defining

$$M(r) \equiv 4\pi \int_0^r \epsilon(r) r^2 dr \tag{4.11}$$

and comparing (4.11) with g_{00}, keeping in mind that $g_{00} = e^{2\nu} = e^{-2\lambda} = 1 - \frac{2GM(r)}{r}$, one can find $k = -8\pi G$, in agreement with the Newtonian limit. This enables us to write the Einstein tensor's entries in the following differential equations interpreting $M(r)$ as the gravitational mass:

$$G_0{}^0 = e^{-2\lambda}(\frac{1}{r^2} - \frac{2\lambda'}{r}) - \frac{1}{r^2} = -8\pi G\epsilon(r)\,, \tag{4.12}$$

$$G_1{}^1 \equiv e^{-2\lambda}(\frac{1}{r^2} - \frac{2\nu'}{r}) - \frac{1}{r^2} = 8\pi G p(r)\,, \tag{4.13}$$

$$G_2{}^2 \equiv e^{-2\lambda}(\nu'' + \nu'^2 - \lambda'\nu' + \frac{\nu' - \lambda'}{r}) = 8\pi G p(r)\,, \tag{4.14}$$

$$G_3{}^3 \equiv G_2{}^2 = 8\pi G p(r)\,. \tag{4.15}$$

Equation (4.15) contains no new information compared to (4.14), but it is possible to derive expressions for λ', ν', ν'^2 and ν'' from equation (4.12) and (4.13). These expressions can be inserted into (4.14) resulting in an expression for the pressure, which in conjunction with (4.11) can be displayed as the well known TOV equations:

$$\begin{aligned} \frac{dM(r)}{dr} &= 4\pi\epsilon(r)r^2\,, \\ \frac{dp(r)}{dr} &= -\frac{[p(r)+\epsilon(r)]\left[M(r)+4\pi r^3 p(r)\right]}{r(r-2M(r))}\,. \end{aligned} \tag{4.16}$$

It is straight forward to solve these equations numerically. The initial conditions usually used are $r = 0$, $M(r = 0) = 0$ and $p(r = 0) = p_{central}$, integrating outward over the radial coordinate to the star's surface, where $p(r = R) = 0$. There is a slight complication with these initial conditions due to the apparent singularity at $r = 0$. This problem is solved by substituting a very small value of $r_{initial}$ instead. Alternatively, it is possible to recast the TOV equations in a way that one integrates over the pressure p instead of r, which also avoids the singularity. However, this practice is uncommon.

4.3.2. Tidal Deformability

Another data point of great interest to modern astrophysics is the tidal deformability of compact stars. It is an intrinsic quantity of an object describing how easy it is to deform it with tidal forces. Early works regarding the relativistic tidal deformability came from Flanagan, Hinderer et al. [Flanagan and Hinderer, 2008, Hinderer, 2008, Hinderer et al., 2010] and Postnikov et al. [Postnikov et al., 2010].
Especially [Hinderer, 2008] contains an in-depth discussion of the derivation of the tidal deformability and the Love-number. When two objects orbit each other, they induce a quadrupole moment Q_{ij} on each other. This takes the following form:

$$Q_{ij} = -\lambda E_{ij}\,, \tag{4.17}$$

where E_{ij} is the tidal field of the companion star and λ is the tidal deformability of the star on which Q_{ij} is induced. It should be kept in mind that λ is an innate property of the object and independent from the tidal field that causes the deformation. The tidal deformability λ can be calculated using the relation:

$$\lambda = k_2 \frac{2R^5}{3G}\,, \tag{4.18}$$

where k_2 is the so-called tidal Love-number, R the radius of the deformed object and G the gravitational constant. Note that k_2 is a constant that results from the perturbation, where the index refers to the $l = 2$ mode of the oscillations eigenfunctions [Regge and Wheeler, 1957, Hinderer, 2008]. It is clear that we need to determine k_2 in order to find λ. When a static tidal field E_{ij} induces a quadrupole moment on a spherically symmetric, static mass M one can write the metric coefficient g_{tt} at large r in asymptotically mass centered Cartesian coordinates as:

$$\frac{(1-g_{tt})}{2} = -\frac{M}{r} - \frac{3Q_{ij}}{2r^3}\left(n^i n^j - \frac{1}{3}\delta^{ij}\right) + O\left(\frac{1}{r^3}\right) + \frac{1}{2}E_{ij}x^i x^j + O\left(r^3\right)\,, \tag{4.19}$$

(see [Thorne, 1998]), where $n^i = x^i/r$. With this expansion one can define E_{ij} and Q_{ij}. One can write down the line element for the geometry of space-time of a spherical, static star as follows:

$$ds_0^2 = g^{(0)}_{\alpha\beta} dx^\alpha dx^\beta = -e^{\nu(r)}dt^2 + e^{\lambda(r)}dr^2 + r^2\left(d\theta^2 + \sin^2\theta d\phi^2\right) \tag{4.20}$$

and the star's stress-tensor as:

$$T_{\alpha\beta} = (\rho + p)u_\alpha u_\beta + p g^{(0)}_{\alpha\beta}\,, \tag{4.21}$$

with ρ and p being the density and the pressure. Introduction of a perturbation $h_{\alpha\beta}$ results in the full metric of the space-time:

$$g_{\alpha\beta} = g^{(0)}_{\alpha\beta} + h_{\alpha\beta}\,, \tag{4.22}$$

where a linearized metric perturbation is introduced. The specifications are static, even-parity perturbations with $l = 2$ in the Regge-Wheeler gauge [Regge and Wheeler, 1957]. This means $h_{\alpha\beta}$ can be written as:

$$h_{\alpha\beta} = \mathrm{diag}\left[e^{-\nu(r)}H_0(r), e^{\lambda(r)}H_2(r), r^2K(r), r^2\sin^2\theta K(r)\right] Y_{2m}(\theta,\varphi)\,, \tag{4.23}$$

with $K(r)$ being related to $H(r)$ by $K'(r) = H'(r) + 2H(r)\Phi'(r)$, where the prime indicates a derivative with respect to r. In addition Y_{lm} represents the spherical harmonics. One can insert this expression and the non vanishing components of the perturbation of the energy-stress tensor into the linearized Einstein equation $\delta G^\beta_\alpha = 8\pi\delta T^\beta_\alpha$. From $\delta G^\theta_\theta - \delta G^\phi_\phi = 0$ one can gather that $H_2 = H_0 \equiv H$. A differential equation describing H(r) is obtained:

$$\begin{array}{l} H'' + H'\left[\frac{2}{r} + e^\lambda\left(\frac{2m(r)}{r^2} + 4\pi r(p-\rho)\right)\right] \\ +H\left[-\frac{6e^\lambda}{r^2} + 4\pi e^\lambda\left(5\rho + 9p + \frac{\rho+p}{(dp/d\rho)}\right) - \nu'^2\right] = 0 \end{array}\,. \tag{4.24}$$

In order to obtain the boundary conditions of (4.24) one can solve for H near $r = 0$, which leads to:

$$H(r) = a_0 r^2\left[1 - \frac{2\pi}{7}\left(5\rho(0) + 9p(0) + \frac{\rho(0)+p(0)}{(dp/d\rho)(0)}\right)r^2 + O\left(r^3\right)\right]\,, \tag{4.25}$$

where a_0 is a constant. Furthermore, equation (4.24) reduces outside the star to:

$$H'' + \left(\frac{2}{r} - \lambda'\right)H' - \left(\frac{6e^\lambda}{r^2} + \lambda'^2\right)H = 0\,, \tag{4.26}$$

which can be transformed into a form utilizing the associated Legendre equation with $l = m = 2$:

$$\left(x^2 - 1\right) H'' + 2xH' - \left(6 + \frac{4}{x^2 - 1}\right) H = 0\,. \tag{4.27}$$

This is achieved by substituting the variable $x = (r/M - 1)$. A general solution to equation (4.27) in terms of the Legendre functions Q_2^2 and P_2^2 can take the following form:

$$H = c_1 Q_2^2\left(\frac{r}{M} - 1\right) + c_2 P_2^2\left(\frac{r}{M} - 1\right)\,. \tag{4.28}$$

The coefficients $c_{1,2}$ have to be determined. This can be accomplished by substituting the expressions for Q_2^2 and P_2^2, which yields:

$$\begin{aligned} H =& c_1\left(\frac{r}{M}\right)^2\left(1 - \frac{2M}{r}\right)\left[-\frac{M(M-r)\left(2M^2 + 6Mr - 3r^2\right)}{r^2(2M-r)^2} + \frac{3}{2}\log\left(\frac{r}{r-2M}\right)\right] \\ &+ 30_2\left(\frac{r}{M}\right)^2\left(1 - \frac{2M}{r}\right)\,. \end{aligned} \tag{4.29}$$

This equation has the following asymptotic behavior at large r:

$$H = \frac{8}{5}\left(\frac{M}{r}\right)^3 c_1 + O\left(\frac{M}{r}\right)^4 + 3\left(\frac{r}{M}\right)^2 c_2 + O\left(\frac{r}{M}\right)\,. \tag{4.30}$$

It is now possible to determine c_1 and c_2 by matching equation (4.30) to the expansion (4.19) using (4.17):

$$c_1 = \frac{15}{8}\frac{1}{M^3}\lambda\mathcal{E}\,, \quad c_2 = \frac{1}{3}M^2\mathcal{E}\,. \tag{4.31}$$

This can be solved for λ in terms of H and its derivative. Using equation (4.18) k_2 can be expressed in those terms as well. However, it is helpful to use the quantity y, instead of H(r). The quantity y is defined as

$$y \equiv RH'(R)/H(R)\,. \tag{4.32}$$

We can write k_2 as:

$$\begin{aligned} k_2 = & \tfrac{8C^5}{5}(1-2C)^2[2+2C(y-1)-y]\times \\ & \left\{2C(6-3y+3C(5y-8))+4C^3\left[13-11y+C(3y-2)+2C^2(1+y)\right]\right. \\ & \left.+3(1-2C)^2[2-y+2C(y-1)]\log(1-2C)\right\}^{-1}. \end{aligned} \tag{4.33}$$

Where C is the compactness of the examined star, which is defined as $C = M/R$.
In order to find the explicit value of k_2, one can calculate H and use that to find y, following the method outlined in [Hinderer et al., 2010]. Consider the line element of the space-time under perturbation:

$$\begin{aligned} ds^2 = & -e^{2\Phi(r)}\left[1+H(r)Y_{20}(\theta,\varphi)\right]dt^2 \\ & +e^{2\Lambda(r)}\left[1-H(r)Y_{20}(\theta,\varphi)\right]dr^2 \\ & +r^2\left[1-K(r)Y_{20}(\theta,\varphi)\right]\left(d\theta^2+\sin^2\theta d\varphi^2\right), \end{aligned} \tag{4.34}$$

where, as above, $K(r)$ is related to $H(r)$ by $K'(r) = H'(r) + 2H(r)\Phi'(r)$. It is possible to restate equation (4.24) in the following way:

$$\begin{aligned} & \left(-\tfrac{6e^{2\Lambda}}{r^2}-2\left(\Phi'\right)^2+2\Phi''+\tfrac{3}{r}\Lambda'\right. \\ & \left.+\tfrac{7}{r}\Phi'-2\Phi'\Lambda'+\tfrac{f}{r}\left(\Phi'+\Lambda'\right)\right)H \\ & +\left(\tfrac{2}{r}+\Phi'-\Lambda'\right)H'+H''=0, \end{aligned} \tag{4.35}$$

where f is defined as $f(p) = \delta\epsilon/\delta p$.The second-order differential equation for H can be separated in a first-order ordinary differential equation (ODE) system:

$$e^{2\Lambda} = \left(1-\frac{2m_r}{r}\right)^{-1}, \tag{4.36}$$

$$\frac{d\Phi}{dr} = -\frac{1}{\epsilon+p}\frac{dp}{dr}, \tag{4.37}$$

$$\frac{dp}{dr} = -(\epsilon+p)\frac{m_r+4\pi r^3 p}{r\left(r-2m_r\right)}, \tag{4.38}$$

$$\frac{dm_r}{dr} = 4\pi r^2 \epsilon \,. \tag{4.39}$$

Equation (4.36)-(4.39) contain the same information as the TOV equations (4.16), with two additional functions $H(r)$ and $\beta(r)$:

$$\frac{dH}{dr} = \beta \tag{4.40}$$

$$\begin{aligned}\frac{d\beta}{dr} =& 2\left(1-2\frac{m_r}{r}\right)^{-1} H\{-2\pi[5\epsilon+9p+f(\epsilon+p)] \\ &+\frac{3}{r^2}+2\left(1-2\frac{m_r}{r}\right)^{-1}\left(\frac{m_r}{r^2}+4\pi r p\right)^2\} \\ &+\frac{2\beta}{r}\left(1-2\frac{m_r}{r}\right)^{-1}\left\{-1+\frac{m_r}{r}+2\pi r^2(\epsilon-p)\right\}\,.\end{aligned} \tag{4.41}$$

This can easily be integrated numerically. The boundary conditions for β and $H(r)$ are found with the expansions $\beta = 2a_0 r$ and $H(r) = a_0 r^2$ for r close to 0. The value of a_0 can be chosen arbitrarily, since it cancels out in the expression for k_2. The value of y can now be determined via equation (4.32), $y = R\beta(R)/H(R)$.
Later in this work, we will discuss an equation of state with a jump in energy density at constant pressure. If there is a discontinuity in energy density, the speed of sound c_s has a discontinuity as well, which effects k_2. At the point of transition f (which is related to c_s) can be written as:

$$f = \frac{d\epsilon}{dp} = \frac{1}{c_s^2} = \left.\frac{d\epsilon}{dp}\right|_{p\neq p_{trans}} + \Delta\epsilon\delta\left(p-p_{trans}\right)\,. \tag{4.42}$$

Due to this behavior, the value of y has to be matched accordingly. In the model described in section 5.1 this is already implicit with the constant speed of sound. However, if one is considering a pure quark star the discontinuity in energy density at its surface has to be taken into account in the following way:

$$y = \frac{R\beta(R)}{H(R)} - \frac{4\pi R^3 \epsilon_-}{M}\,, \tag{4.43}$$

where ϵ_- is the energy density inside the star. Damour and Nagar [Damour and Nagar, 2009] discussed the situation of a discontinuity in far more detail.

A short note on nomenclature: the quantity Λ, which can be defined as

$$\Lambda = \frac{\lambda}{M^5} = \frac{3}{2} k_2 C^{-5}, \tag{4.44}$$

is usually referred to as tidal deformability. However, in some publications λ is assigned that name instead. In both cases, the quantity describes the ability of the object to be deformed by tidal forces; we will differentiate between the two in the following chapters where necessary.

4.4. Constraints on Pure Neutron Star Equations of State

In this section, we examine the most relevant data points from astrophysical observations. Those are the mass constraints (subsection 4.4.1), the radius constraints (subsection 4.4.2) and the constraints from tidal deformability, which can be estimated using gravitational wave signals from neutron star mergers (subsection 4.4.3). We then apply the constraints to the equations of state presented in chapter 3. This is done by comparing the precise predictions from theory (section 4.3) with the astrophysical data points. It must be noted that our EoS is not suited to describe the crust of a neutron star. Instead, we use an approach introduced by Baym, Pethick and Sutherland (BPS) [Baym et al., 1971] that Negele and Vautherin expanded upon [Negele and Vautherin, 1973], which is valid up to half saturation density. For higher densities, we use our relativistic mean field approach.

4.4.1. Mass Constraints on Neutron Stars

One of the most constraining neutron star quantities we can determine is its mass. This quantity, alongside an estimate of the radius can be extracted from the observation of binary star systems that contain neutron stars. There is a variety of methods and observables that aid in this endeavor, which can be found in relevant textbooks like [Schaffner-Bielich, 2020]. In this context one might find the summary on masses and radii of neutron stars by Özel and Freire useful as well [Ozel and Freire, 2016]. It is possible to determine the mass of a pulsar with much greater accuracy than its radius due to its small size. However, the rigorosity of the mass constraint is strongly

dependent on the companion star in the system. For example, neutron stars in a x-ray binary accrete mass from their companion, which complicates the determination of its mass. A specific variation of such binaries are so-called black widow pulsars, which slowly destroy their companion, earning them their sobriquet. This may even destabilize or deform the neutron star and usually leads to large mass estimates with significant uncertainties. The most reliable mass constraints can be derived from double neutron star binaries, of which the most famous is the Hulse-Taylor binary [Hulse and Taylor, 1975], the first binary pulsar system detected. For our purposes, the most massive neutron stars are of particular interest. They provide a limit that every equation of state aiming to describe reality has to account for. If an EoS cannot generate a neutron star meeting the mass constraint, it is not a viable theory. It is well established, that the maximal mass of neutron stars is at least $2\,M_\odot$ [Demorest et al., 2010, Antoniadis et al., 2013, Fonseca et al., 2016]. However, newer observations report even higher masses, such as the pulsar PSR J0740+6620 with $2.14^{+0.10}_{-0.09}\,M_\odot$ [Cromartie et al., 2019] and even more recently PSR J0952-0607 with $2.35 \pm 0.17\,M_\odot$ [Romani et al., 2022]. One should note, that the latter finding is a black widow pulsar, which casts slight uncertainty on the result. The gravitational wave event GW190814 needs to be mentioned in this context as well, as it was determined to originate from a merger of a $23.2^{+1.0}_{-1.0}\,M_\odot$ black hole with a $2.59^{+0.08}_{-0.09}\,M_\odot$ unknown object [Abbott et al., 2020]. This unknown object would either be the most massive neutron star ever observed or the least massive black hole. It is located in the mass gap between black holes and neutron stars. The consensus on the issue seem to be that a black hole is the most likely explanation [Fattoyev et al., 2020, Tews et al., 2021], but the possibility of a neutron star [Most et al., 2020, Dexheimer et al., 2021, Nathanail et al., 2021, Godzieba et al., 2021] or more exotic compact object [Tan et al., 2020, Bombaci et al., 2021, Wystub et al., 2021] cannot be ruled out completely.
Using the TOV equations discussed in section 4.3 we can determine the mass radius relation for a given equation of state. In our case we examine the RMF equations of state from chapter 3, where $J = 32\,\text{MeV}$, $L = 60\,\text{MeV}$ and the effective mass is varied in bins of 0.05 from $m^*/m = 0.55$ to $m^*/m = 0.75$ at zero temperature. The constraints and mass radius relations are visualized on the left-hand side of figure 4.1. We find that only the softest case, $m^*/m = 0.75$, falls short of the mass limit, if we consider only the masses of known neutron stars. If we consider the unknown object of GW190814 as well, only the cases $m^*/m = 0.55$ and $m^*/m = 0.60$ remain valid. This points towards GW190814 not being a neutron star, as the constraint from GW170817 [Abbott et al., 2017, Abbott et al., 2018, Abbott et al., 2019] rules out these exact cases, which we will

see in subsection 4.4.3.

4.4.2. Radius Constraints on Neutron Stars

The precise measurement of a neutron star's radius is as important to determining the equation of state as the mass. However, it is much more difficult to determine the radius from the dynamics of binary systems. The "Neutron star Interior Composition ExploreR" (NICER) mission takes a different approach, where the X-ray signal of the observed pulsar is examined in search for hot spots [Gendreau et al., 2012, Watts et al., 2016]. The visibility of a hot spot would increase the X-ray intensity. In a Newtonian picture, the rotation of the pulsar should move the hot spots into and out of view. However, the high compactness of neutron stars requires that general relativity is applied, which means, that light is bend around the neutron star. Therefore, the hot spot is in view for a longer time. This effect is intensified by a more compact object, enabling the observer to relate the time the hot spots are visible with the compactness of the neutron star and therefore its radius. This underlying concept of NICER is presented by Gendreau et al. [Gendreau et al., 2012, Watts et al., 2016] when the mission was proposed. At the time of this work NICER has investigated two pulsars PSR J0030+0451 [Miller et al., 2019, Riley et al., 2019, Raaijmakers et al., 2019] and PSR J0740+6620 [Miller et al., 2021, Riley et al., 2021, Raaijmakers et al., 2021], which at the time was the most massive neutron star [Cromartie et al., 2019]. Even though NICER falls short of their initially stated goal of reaching 5% certainty [Gendreau et al., 2012] the radius estimates from these observations can be used to constrain the equations of state to great effect, especially for hybrid star equations of state, as we will show in chapter 5. A significant hurdle is the model used to describe the hot spots, which lead to two different radii estimates for both measurements, one by Riley et al. [Riley et al., 2019, Riley et al., 2021] and one by Miller et al. [Miller et al., 2019, Miller et al., 2021] using different models. The data gained by NICER can be translated into regions in a mass radius diagram that a mass radius relation has to pass through in order to be viable. These regions take the form of likelihood ellipses, that are orientated along the compactness of the observed neutron star. Particularly, the compactness of PSR J0030+0451 was well constrained to $C = 0.16 \pm 0.01$ [Raaijmakers et al., 2019].
Additionally, constraints could be put on the radius from gravitational wave observation. It is possible to infer a radius estimate from the value of $\tilde{\Lambda}$ [Abbott et al., 2017], which is

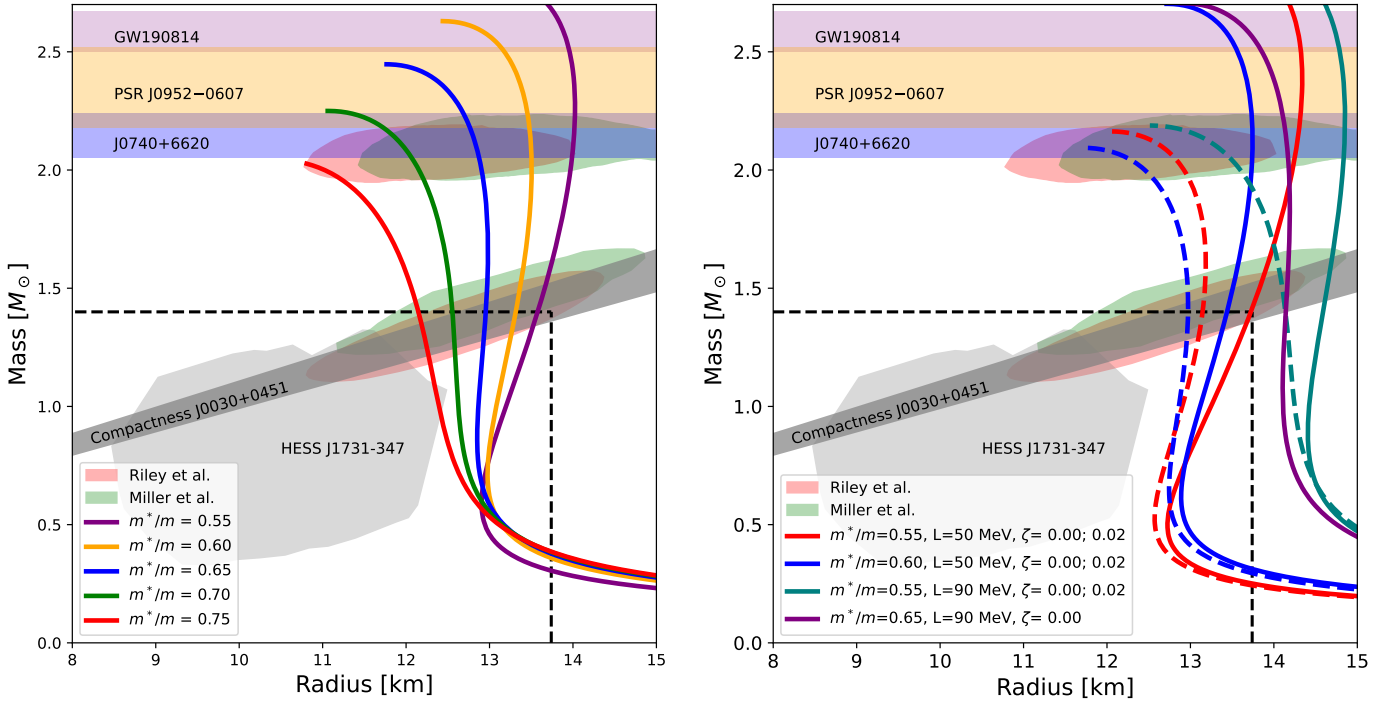

Figure 4.1.: The 1σ NICER constraints from Riley [Riley et al., 2019, Riley et al., 2021] (shaded red) and Miller [Miller et al., 2019, Miller et al., 2021] (shaded green) do not rule out any of the EoSs presented in chapter 3 (left). However, the softest case, $m^*/m = 0.75$, is not compatible with the black widow pulsar mass constraint [Romani et al., 2022] (shaded orange). Only the stiffest cases reach the hypothetical limit from GW190814 [Abbott et al., 2020]. The black dashed line indicate the upper estimate for a 1.4 $M_\odot$ neutron star from GW170817 [Most et al., 2018]. The same constraints are applied to a similar RMF EoS provided by Farrukh Fattoyev [Fattoyev, 2022], where the quadratic self interaction ζ is used to adjust the stiffness of the EoS (right). For these EoSs the slope parameter is varied as well, where a higher value of L leads the mass radius relation to be located at higher radii, placing them outside the GW170817 constraint.

a quantity we discuss in the next subsection (see equation (4.45)). Radius estimates for GW170817 [Abbott et al., 2017, Abbott et al., 2018, Abbott et al., 2019] were determined by numerous groups (see for example: [Annala et al., 2018, Most et al., 2018, Tews et al., 2018]). The results range between $8.53\,\mathrm{km} < R_{1.4M_\odot} < 13.74\,\mathrm{km}$ as Most et al. report [Most et al., 2018]. GW170817 provides a stronger constraint on the upper limit of the radius, where NICER features a strong constraint for the lower limit as well.
On the right side of figure 4.1 the mass radius relations of the equation of state from chapter 3 is compared with the 1σ NICER results, as well as the mass constraints from the previous subsection. We vary the effective mass and keep the symmetry energy and slope parameter identical between the cases. The NICER constraints are depicted as a red ellipse for the estimates by Riley et al. [Riley et al., 2019, Riley et al., 2021] and green for the estimates by Miller et al. [Miller et al., 2019, Miller et al., 2021]. In addition, the upper radius estimate for a $1.4\,M_\odot$ neutron star suggested by Most et al. [Most et al., 2018] based on GW170817 is included as a dashed black line. However, it should be noted that the tidal deformability can be used directly to constraint the EoS to a stronger degree than the radius, which will be shown in the next subsection. None of the parameter sets used here can be ruled out by either the radius constraints from NICER or GW170817. However, it is notable that the softest EoS is located at the lowest possible radius in the Riley constraint for J0740+6620 [Riley et al., 2021], while the stiffest EoS is nearly outside the same constraint at the upper radius limit. On the left side of the figure, a few mass radius relations based on a similar relativistic mean field equations of state are shown. They were helpfully provided by Farrukh Fattoyev [Fattoyev, 2022] and are strongly constrained from finite nuclei. As a result of this, the effective mass cannot be varied in a spectrum as large as we do. The softness of the equation of state is varied instead via the ω mesons quadratic self coupling ζ. Varying ζ has the advantage over varying m^*/m when it comes to fitting the equation of state to low density constraints, as ζ only effects the EoS at high densities. However, as is shown in figure 4.1 the increase in softness does not result in significantly different radii. The mass radius relation in this model can still be adjusted by varying the slope parameter, where greater values of L lead to a placement of the mass radius relation at higher radii. This comes with the additional problem that high values of L are not compatible with χ_{EFT} constraints. In this work, we only vary m^*/m, which gives us a greater range in radii that we can cover within chiral and astrophysical constraints. However, it might prove interesting to investigate a varied ζs influence on the possibility of phase transitions as well, especially because a phase transition might circumvent some of the

astrophysical constraints high values of L are challenged by, such as GW170817. A short overview of the $L = 90\,\mathrm{MeV}$ EoSs used in figure 4.1 can be found in subsection 5.4.4
During the later stages of this work, a neutron star with a surprisingly small mass was detected in a supernova remnant [Doroshenko et al., 2022]. A mass of $M = 0.77^{+0.20}_{-0.17}\,M_\odot$ was reported for this remnant HESS J1731-347, which is below most estimates for the smallest neutron star masses generated by supernovae [Ozel et al., 2012, Ozel and Freire, 2016, Müller et al., 2019, Suwa et al., 2018]. Furthermore, a radius of $10.4^{+0.86}_{-0.78}\,\mathrm{km}$ was claimed, which is such a small value that nearly all but the softest pure hadronic equations of state would be ruled out by this observation. To illustrate this point, the 2σ constraint from Doroshenko et al. [Doroshenko et al., 2022] is included in figure 4.1, where only the $m^*/m = 0.75$ case comes close. This has lead to some speculation if this object might be something more exotic than a pure neutron star [Di Clemente et al., 2022, Tsaloukidis et al., 2022]. We will touch upon this hypothesis in chapter 5.

4.4.3. Tidal Deformability from Gravitational Waves

Despite the well known dependence of the equation of state on the tidal deformability Λ[1] the possibility to constrain it using Λ is a comparatively new development. This is because there needs to be a tidal field present that deforms the neutron star we wish to observe. In other words, it is impossible to determine the tidal deformability of a neutron star in isolation, we have to observe merger events instead. Such an event still has to be in the frequency range of the gravitational wave detector, which means that compact binary inspirals are required. This is also favorable because a stronger gravitational field provided by compact objects causes a stronger deformation, which in turn will lead to a stronger impact in the gravitational wave signal emitted. However, this is only the case if the two objects are of similar size. For example, the merger of a neutron star and a black hole does produce a detectable gravitational wave signal, in fact we might have observed such an event already in GW190814 [Abbott et al., 2020, Tsokaros et al., 2020, Most et al., 2020, Godzieba et al., 2021, Fattoyev et al., 2020, Dexheimer et al., 2021, Lim et al., 2021, Tews et al., 2021, Tan et al., 2020, Zhang and Li, 2020, Nunes et al., 2020, Blaschke and Cierniak, 2021, Nathanail et al., 2021].

1 see for example the previously discussed works: [Hinderer, 2008, Hinderer et al., 2010, Postnikov et al., 2010]

However, it is unlikely that the deformation of the neutron star would leave an impact significant enough to be visible in the signal, which means that neutron star - black hole mergers are not suitable to determine the tidal deformability. This leaves us with the neutron star - neutron star merger scenario. Since two neutron stars are required and both are deformed by the tidal field of the other, we cannot determine the tidal deformability of just one companion star. Instead, we can extract a combined quantity $\tilde{\Lambda}$:

$$\tilde{\Lambda} = \frac{16}{13} \frac{(m_1 + 12m_2)\, m_1^4 \Lambda_1 + (m_2 + 12m_1)\, m_2^4 \Lambda_2}{(m_1 + m_2)^5}, \tag{4.45}$$

where Λ_1 is the tidal deformability of the more massive star and Λ_2 the tidal deformability of its companion. Additionally, it is possible to determine the so-called chirp mass $\mathcal{M}$ from the gravitational wave phase. This chirp mass describes the inspiral phase of the gravitational wave emission. It can be expressed as:

$$\mathcal{M} = \left(\frac{q}{(1+q)^2} \right)^{\frac{3}{5}} M_{\text{total}}\ , \tag{4.46}$$

with q as the mass ratio between the two companions and M_{total} their combined masses. The mass of a singular companion cannot be measured precisely in an inspiral. Instead, one has to assume the values for the spin priors of the neutron stars $|\chi|$. Using these an estimate for the mass ratio can be determined, where low spin priors lead to smaller uncertainties in q.

Currently, only one reliable neutron-neutron star merger event has been observed [Abbott et al., 2017]. This event called GW170817 was determined to have a chirp mass of $\mathcal{M} = 1.1977^{+0.0008}_{-0.0003}$ [Abbott et al., 2017], which accounting for cosmological redshift translates to $\mathcal{M} = 1.186^{+0.001}_{-0.001}$ [Abbott et al., 2019]. For low spin priors $|\chi|$ they determine a mass ratio $1 < q < 1.4$ [Abbott et al., 2017]. The parameter $\tilde{\Lambda}$ can be constrained to $\tilde{\Lambda} < 800$, which in turn can be used to find a likely upper value for the tidal deformability of a $1.4 M_\odot$ neutron star, which [Abbott et al., 2017] initially stated to be $\Lambda_{1.4M_\odot} < 800$. This was later updated to $\Lambda_{1.4M_\odot} = 190^{+390}_{-120}$ [Abbott et al., 2018].

In addition to the gravitational wave event a corresponding electromagnetic signal was observed, which can be used to constrain $\tilde{\Lambda}$ further, as Radice et al. [Radice et al., 2018] and Coughlin et al. [Coughlin et al., 2018] did. Radice et al. found values of $\tilde{\Lambda} \geq 400$, where Coughlin et al. using a different approach, find a lower limit of $\tilde{\Lambda} \geq 197$.

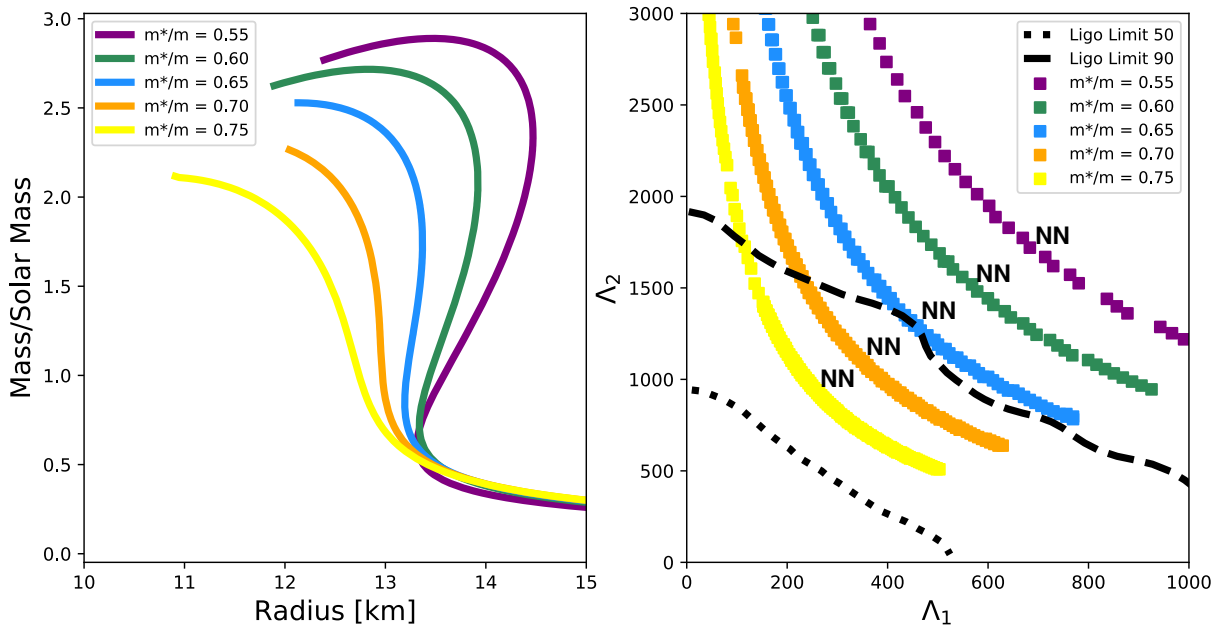

Figure 4.2.: Left: Mass radius relation of EoSs with different effective mass m^*/m. Right: The corresponding lines in a $\Lambda_1 - \Lambda_1$ plot, where the LIGO/Virgo credibility limits from [Abbott et al., 2019] are replicated as a dotted black line (50%) and a dashed black line (90%). Higher effective masses are more suitable to the gravitational wave data. This figure is from [Christian and Schaffner-Bielich, 2020].

An intuitive way of visualizing the constraints put on an equation of state by $\tilde{\Lambda}$ is a $\Lambda_1 - \Lambda_2$ plot. In such a plot, the value of $\tilde{\Lambda}$ can be translated to an area indicating the confidence intervals of the measurement. The validity of an equation of state can then be tested, by finding all possible combinations of neutron stars described by the EoS, that add up to the chirp mass. Marking the point generated by such a combination in the $\Lambda_1 - \Lambda_2$ plot will generate a line unique to the EoS. If the line is within the credibility limit, the EoS is compatible with the data from GW170817. We use such a plot to investigate the compatibility of our EoS with the gravitational wave data in figure 4.2. On the left side of figure 4.2 the mass radius relations of the examined EoSs are shown. We consider the EoSs discussed in chapter 3 with effective masses between $m^*/m = 0.55 - 0.75$ at zero temperature. On the right side, the $\Lambda_1 - \Lambda_2$ contains the credibility limits, depicted as a bold black dashed line for the 90% limit and a smaller dotted black line for the 50% limit. The x-axis is the tidal deformability value of the more massive star, the y-value the less massive one. Merger scenarios closer to the

origin are more compact than those far away. As we know, increased effective masses lead to more compact solutions, which in turn are more compatible with the GW170817 data. The cases $m^*/m = 0.55$ and $m^*/m = 0.60$ are competently outside the credibility limit, and the $m^*/m = 0.65$ case is only barely within the limit. Hornick et al. [Hornick et al., 2018] confirm this result.

This result strongly indicates, that stiff equations of state are disfavored. However, this finding goes contrary to the mass constraint, which disfavors soft equations of state. Only the cases $m^*/m = 0.65$ and $m^*/m = 0.70$ are compatible with both GW170818 and the newest mass constraint from J0952-0607 [Romani et al., 2022].

5. Hybrid Stars

In this chapter, we consider the possibility and implications of a phase transition from hadronic to quark matter occurring in neutron stars. As mentioned before, it is known that high density matter will at some point transition to a quark-gluon plasma. However, there is no certainty that the densities present in the center of a neutron star are sufficient to allow for such a transition. Furthermore, a phase transition might destabilize an otherwise stable neutron star, as was shown in some early works on the topic, for example by Seidov [Seidov, 1971] and Kämpfer [Kämpfer, 1981]. A stable neutron star with a phase transition between its hadronic crust and its quark matter core is referred to as a hybrid star [Ivanenko and Kurdgelaidze, 1965, Itoh, 1970, Alford et al., 2005, Coelho et al., 2010, Chen et al., 2011, Masuda et al., 2013, Yasutake et al., 2014, Zacchi et al., 2016], because its part quark star and part hadronic star, both of which are theorized to have "pure"-star versions. Purely hadronic stars have been discussed in the previous chapter and while pure quark stars will not be discussed in detail in this thesis it is worth pointing out some relevant works: [Ivanenko and Kurdgelaidze, 1965, Itoh, 1970, Bodmer, 1971, Haensel et al., 1986, Alcock et al., 1986, Fraga et al., 2002, Zacchi et al., 2015, Drago et al., 2016].

In section 5.1 we will discuss the model we use to describe the phase transition and the stability of the resulting hybrid stars. We will proceed to investigate possible indications for a phase transition provided by mass, radius and tidal deformability data in section 5.2 and search for those signatures using recent astrophysical observations in section 5.3. Finally, we will take some time to touch on possible production scenarios for hybrid stars as well as alternative explanations for potential data points in section 5.4.

5.1. Equations of State with a Phase Transition

There are many possibilities of including a phase transition in an equation of state that can vary based on the underlying assumptions, such as the presence of a mixed phase or the order of the phase transition. The most common types of construction are the Maxwell- and Gibbs-construction. A phase transition in thermodynamic equilibrium requires, that the pressure and the chemical potential at the point of transition are identical in both phases. For the Gibbs construction, one considers not only the baryon chemical potential, but the charge chemical potential as well. The conditions for a Gibbs construction between a quark phase (Q) and a hadronic phase (H) can be written as:

$$p^{(H)}(\mu_b^{(H)}, \mu_q^{(H)}) = p^{(Q)}(\mu_b^{(Q)}, \mu_q^{(Q)}); \quad \mu_b^{(H)} = \mu_b^{(H)}; \quad \mu_q^{(Q)} = \mu_q^{(Q)}\,. \tag{5.1}$$

Since global charge neutrality is imposed, the charge chemical potential for a specific baryon chemical potential is fixed. This means it is unlikely for the chemical potentials in the hadronic phase at the start of the transition to lead to charge neutrality in the quark phase as well. This problem is solved with a mixed phase, where the chemical potentials are adjusted along a pressure gradient Δp. Descriptively, this means there are "bubbles" of one phase present in the other, in such a way that global charge neutrality in maintained. Depending on the models used, this mixed phase can be over a large range of Δp or a small one. This is related to the surface tension σ, where greater surface tension leads to smaller Δp. At a critical value of σ, which is dependent on the model, Δp tends to 0 and the construction can be regarded as a Maxwell construction [Maslov et al., 2019], which is a simplified version of the Gibbs construction. Here only the pressure and the baryon chemical potential need to be considered, and no mixed phase is possible. The charge chemical potential jumps in this construction. The baryon density is not identical in both phases and neither is the energy density $\epsilon(p)$. Instead, $\epsilon(p)$ increases instantly at the point of transition for a value of $\Delta\epsilon$. Of course the concept of this jump in energy density is applicable to a Gibbs construction as well however due to the non-vanishing Δp is less strictly defined.
In the following we will use a Maxwell construction, thus assuming a strong first order phase transition with a strong surface tension present, since this heavily favors twin star configurations (see section 5.2), which we want to investigate.

5.1.1. Constant Speed of Sound Parameterization

In this work, we use a generic approach for the quark phase. It is based on earlier works by Zdunik et al. [Zdunik and Haensel, 2013] and Alford et al. [Alford et al., 2014] and offers a great amount of flexibility in fitting it to the hadronic EoS, while sacrificing some microscopic clarity by assuming a constant speed of sound. This ansatz can be expressed as a Maxwell construction and summarized as follows:

$$\epsilon(p) = \begin{cases} \epsilon_{hadronic}(p) & p < p_{trans} \\ \epsilon_{hadronic}(p_{trans}) + \Delta\epsilon + c_{QM}^{-2}(p - p_{trans}) & p > p_{trans} \end{cases}, \tag{5.2}$$

where a hadronic equation of state is used to describe the mantle of the star up to a transitional pressure of p_{trans}, at which point the EoS undergoes a discontinuity in the energy density ϵ of the value $\Delta\epsilon$. The following quark phase is described by assuming a constant sound speed c_{QM}, resulting in a linear function with a slope of c_{QM}^{-2}. This constant speed of sound approximation is a somewhat simplistic model, that could be replaced by a more sophisticated EoS. However, this method of describing the speed of sound as constant for quark matter is well established (see also [Zdunik et al., 2006, Agrawal, 2010, Bonanno and Sedrakian, 2012, Zdunik and Haensel, 2013]). The approach is justified by the nearly constant speed of sound predicted in two-flavor superconducting (2SC) and color flavor locked (CFL) superconducting quark matter predicted by NJL[1] type models as Zdunik and Haensel argue [Zdunik and Haensel, 2013]. Due to it being generic, it lends itself to investigate a broad variety of possibilities, allowing for an easy and still reliable fit to any hadronic EoS, where a more rigorous model might need more manual adjustments.

Of the three free parameters of equation (5.2) we only fix the speed of sound, the other parameters will be varied in the next (sub)sections. The value of c_{QM} for the majority of this work will be 1, which is the stiffest possible equation of state. We argue, that this choice allows us to find the greatest possible variety in solutions, despite the conformal limit being $c_{QM} = 1/3$. Later in this chapter, figure 5.4 illustrates this point. Here, the parameter space generating hybrid stars is shown. Using a constant speed of sound at the conformal limit reduces the size of the parameter space, but $c_{QM} = 1$ does not produce a type of mass-radius relation that is not present for the conformal limit as well. In figure 5.1 equation (5.2) is visualized with an equation of state from chapter 3 as

1 Nambu–Jona-Lasinio

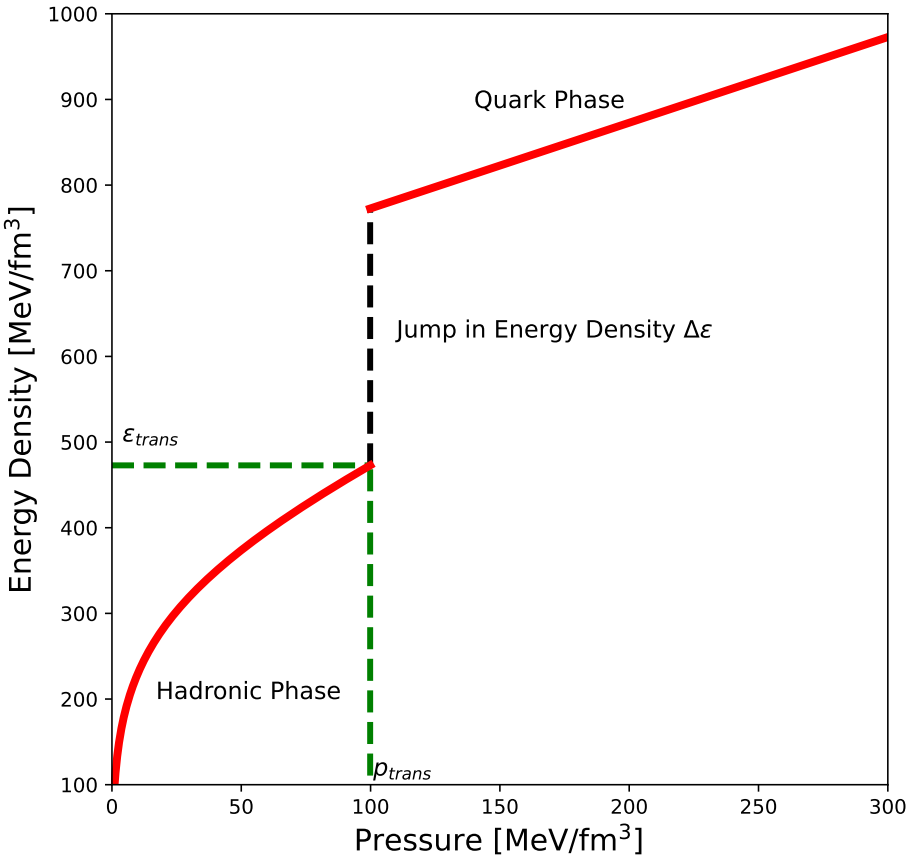

Figure 5.1.: The energy density and the pressure of an EoS with a first order phase transition, as in (5.2). The hadronic EoS has the effective mass $m^*/m = 0.65$ at saturation density. The parameters for the phase transition are $p_{trans} = 100\,\mathrm{MeV/fm^3}$ and $\Delta\epsilon = 300\,\mathrm{MeV/fm^3}$. After the phase transition, the matter is described as quark matter with a constant speed of sound of $c_{QM} = 1$.

the hadronic part, where the effective mass is $m^*/m = 0.65$. In this case the transition parameters have the values $p_{trans} = 100\,\mathrm{MeV/fm^3}$, $\Delta\epsilon = 300\,\mathrm{MeV/fm^3}$ and $c_{QM} = 1$. The jump in energy density is represented by the dashed black line, the remainder of $\epsilon(p)$ as a red line. The energy density in the hadronic phase at the point of transition is ϵ_{trans} and shown with a green dashed line, as is the transitional pressure p_{trans}, which is identical in both phases.

5.1.2. Stability Criterion for First Order Phase Transitions

It is not unreasonable to assume that the presence of a sharp first order phase transition to quark matter like described above might destabilize a neutron star. Thankfully, there is a criterion that considers this possibility, the so-called Seidov limit [Seidov, 1971], that was rediscovered by Kämpfer [Kämpfer, 1981]. It states that a value of $\Delta\epsilon$ will not destabilize a neutron star with a central pressure close to p_{trans}, if

$$\frac{\Delta\epsilon}{\epsilon_{trans}} \leq \frac{1}{2} + \frac{3}{2}\frac{p_{trans}}{\epsilon_{trans}} \tag{5.3}$$

holds true. We will briefly summarize how it is derived following [Schaffner-Bielich, 2020]. We start by contemplating a star with the central pressure $p_{central}$ just below the transitional pressure. Following the TOV equations (4.16) the gradient for the pressure can be stated as:

$$\frac{dp}{dr} = -\frac{p+\epsilon}{r(r-2m)}\left(m + 4\pi r^3 p\right) . \tag{5.4}$$

Since we are interested in the phase transition we consider the core of the star specifically, which means that we are operating at small radii allowing us to ignore Schwarzschild corrections and to approximate the energy density and pressure as constant, barring the phase transition of course. For a purely hadronic matter case, where we can use $p_{central} \simeq p_{trans}$ and $\epsilon = \epsilon_{trans}$, the mass of a small sphere at the star's center can be expressed as:

$$m_{HM} = \frac{4\pi}{3} r^3 \epsilon_{trans} . \tag{5.5}$$

This expression can be inserted into equation (5.4) giving us the pressure gradient just before a phase transition takes place:

$$\frac{dp_{HM}}{dr} = -\frac{p_{trans}+\epsilon_{trans}}{r^2}\left(\frac{4\pi}{3} r^3 \epsilon_{trans} + 4\pi r^3 p_{trans}\right) , \tag{5.6}$$

which can be integrated to find the pressure as a function of the radius r:

$$p_{HM}(r) = p_{trans} - \frac{2\pi}{3}\left(p_{trans}+\epsilon_{trans}\right)\left(p_{trans}+3\epsilon_{trans}\right) r^2 . \tag{5.7}$$

If we increase the pressure at the center of the star slightly by a small amount δ to $p_{central} = p_{trans} + \delta$ a quark matter sphere is created at the center of the star. With the way our equation of state is set up, this sphere should have a significantly different energy density with $\epsilon_{QM} = \epsilon_{trans} + \Delta\epsilon$, while the pressure changes only slightly. The mass of the quark matter sphere can be stated as:

$$m_{QM} = \frac{4\pi}{3} r_{QM}^3 \epsilon_{QM}\,, \tag{5.8}$$

with r_{QM} being the radius of the sphere. To describe the pressure gradient of the region, we again insert this mass into equation (5.4):

$$\frac{dp_{QM}}{dr} = -\frac{p_{trans} + \epsilon_{trans}}{r^2} \left(\frac{4\pi}{3} r^3 \epsilon_{QM} + 4\pi r^3 p_{trans} \right) . \tag{5.9}$$

Notice that p_{QM} does not refer to the pressure of the quark phase, but to the circumstance that a phase transition to quark matter is present in the considered star. Unlike for the pressure increase δ this means ϵ_{QM} only contributes through the mass term. For δ only the quark phase is relevant, which means we can write δ as:

$$\delta = -\frac{2\pi}{3} \left(p_{trans} + \epsilon_{QM} \right) \left(p_{trans} + 3\epsilon_{QM} \right) r_{QM}^2 \,. \tag{5.10}$$

Following Lighthill [Lighthill, 1950] who's Newtonian stability analysis Seidov [Seidov, 1971] extended we can identify the difference in the two pressure solutions as a perturbation function with an ansatz containing A and B as coefficients determined by the boundary conditions and neglecting higher orders. This means:

$$\Pi = p_{QM} - p_{HM} = A + \frac{B}{r} \,. \tag{5.11}$$

Considering the boundary condition for the radius of the quark core, with $p_{QM} = p_{trans}$ at the point of transition, we find:

$$\Pi(r_{QM}) = \frac{2\pi}{3} \left(p_{trans} + \epsilon_{trans} \right) \left(p_{trans} + 3\epsilon_{trans} \right) r_{QM}^2 \,. \tag{5.12}$$

The second boundary condition is given by the gradient:

$$\frac{d\Pi}{dr} = -\frac{B}{r_{QM}^2} = \frac{dp_{QM}}{dr} - \frac{dp_{HM}}{dr} = \frac{4\pi}{3} \left(p_{trans} + \epsilon_{trans} \right) \left(2p_{trans} + 3\epsilon_{trans} + 3\epsilon_{QM} \right) r_{QM}\,,$$

(5.13)

allowing us to find an expression for the coefficient A and relate it to δ:

$$A = \frac{(p_{trans} + \epsilon_{trans})\left(3p_{trans} + 3\epsilon_{trans} - 2\epsilon_{QM}\right)}{\left(3p_{trans} + \epsilon_{QM}\right)\left(p_{trans} + \epsilon_{QM}\right)}\delta\,. \tag{5.14}$$

Let us now consider the entire compact star. At large radii Π can be simplified to $\Pi = A$, as the term including B becomes small. This means p_{QM} and p_{HM} are identical, except for a shift $A(\delta)$ that is constant. The mass change of the compact star caused by changing the central pressure by δ can therefore be expressed as a relation of A and δ resulting in:

$$\frac{dM_{QM}}{dp_{central}} = \frac{(p_{trans} + \epsilon_{trans})\left(3p_{trans} + 3\epsilon_{trans} - 2\epsilon_{QM}\right)}{\left(3p_{trans} + \epsilon_{QM}\right)\left(p_{trans} + \epsilon_{QM}\right)} \times \frac{dM_{HM}}{dp_{central}}\,. \tag{5.15}$$

This expression will become negative if $3p_{trans} + 3\epsilon_{trans} - 2\epsilon_{QM} < 0$, which would denote the end of a stable sequence [Bardeen et al., 1966]. As we were interested in the greatest possible jump in energy density $\Delta\epsilon$ before the sequence becomes unstable, we rephrase the condition:

$$\frac{\epsilon_{QM}}{\epsilon_{trans}} = \frac{\epsilon_{trans} + \Delta\epsilon}{\epsilon_{trans}} \geq \frac{3}{2}\left(1 + \frac{p_{trans}}{\epsilon_{trans}}\right)\,, \tag{5.16}$$

which can easily be identified as the Seidov limit (5.3).

5.2. Signature of Hybrid Stars in Astrophysical Data

As established in the previous section, it is quite possible for a phase transition to occur in neutron stars without it destabilizing them. This raises the question, how this rapid change at the core would be detectable or rather, if a detection is possible at all. In this section, we will examine possible indicators for the presence of phase transition in neutron stars. The application of these indicators to astrophysical data can be found in the following section 5.3.

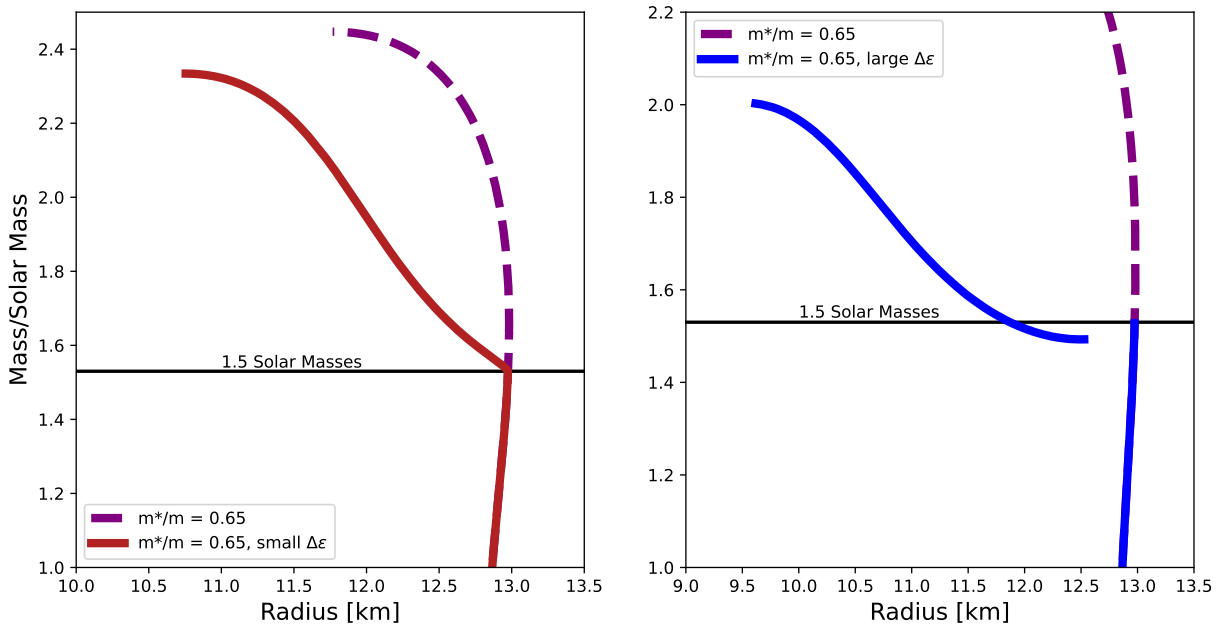

Figure 5.2.: Left is a mass radius relation for the $m^*/m = 0.65$ EoS with a phase transition and a small jump in energy density. The sequence remains stable and there are no twin stars present. If $\Delta\epsilon$ is increased, as is the case on the right, twin stars can be found, in this case for $1.5M_\odot$, which is the mass at the point of transition.

5.2.1. Mass Radius Effects

It is not far-fetched to assume that a sudden drastic change in the equation of state will be reflected in the mass radius relation, if the sequence does not become unstable. An example of that is shown in figure 5.2 on the left side. Here, a kink in the mass radius relation clearly indicates the point of transition at around $1.5M_\odot$. This EoS is compliant with the Seidov limit.

However, there is also a possibility not covered by the Seidov limit. A sequence of neutron stars could regain stability after it was destabilized by a small quark matter core close to the point of transition at even higher pressures. This scenario would manifest as a second branch in the mass radius relation, which is made up entirely of hybrid stars, whereas the first branch consists nearly completely of pure hadronic stars, as can be seen on the right side of figure 5.2. A particularity of this case is the presence of a mass gap between the last star of the hadronic branch and the minimum of the second branch, creating two stars with exactly the same mass, but different radii. This configuration is referred to as twin stars and could be a strong candidate for indicating the existence

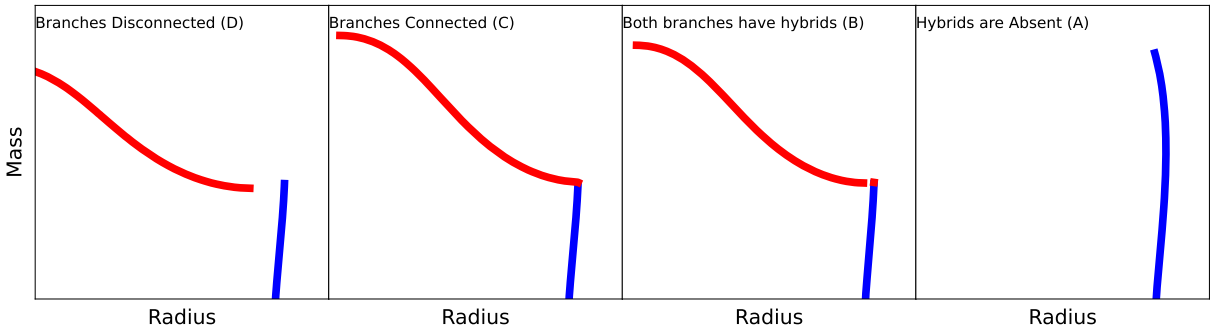

Figure 5.3.: Hadronic stars are shown in blue, hybrid stars are shown in red. Either a mass gap is present, as is the case for class "disconnected" (D) and "both" (B), or a phase transitions takes place without a mass gap and the branches are "connected" (C), meaning only a kink is present in the mass radius relation. Of course, it is also possible that no phase transition is present, as shown in the "absent" (A) case.

of a phase transition in neutron stars if observed [Kämpfer, 1981, Glendenning and Kettner, 2000, Schertler et al., 2000, Schaffner-Bielich et al., 2002, Zdunik and Haensel, 2013, Alford et al., 2015, Blaschke and Alvarez-Castillo, 2016, Zacchi et al., 2017, Alford and Sedrakian, 2017, Christian et al., 2018, Blaschke et al., 2020, Jakobus et al., 2021]. Due to their status as a separate branch from the hadronic branch, they are also referred to as the "third family" of compact stars, with the first "family" being white dwarfs and the second neutron stars. We will discuss whether or not the indicators for a phase transition provided by a mass radius relation with a kink or a mass gap are sufficient for confirmation of a transition using current astrophysical constraints in section 5.3.

Hybrid Star Classification by Alford et al.

Even a model as generic as the one presented in section 5.1.1 gives rise to a myriad of hybrid star scenarios. Because of this, it can be useful to categorize the different results. One of the first attempts to do so was presented by Alford et al. [Alford et al., 2013]. They used the Seidov limit to sort hybrid star solutions into the classes "absent" (A), "both" (B), "connected" (C) and "disconnected" (D). These titles refer to the presence (or absence in case of A) of hybrid stars in the two branches. In class A there are no hybrid stars, they are absent. In class B the first and second branch both contain hybrids. In case C, there is no second branch, because the two branches are connected. Hybrids

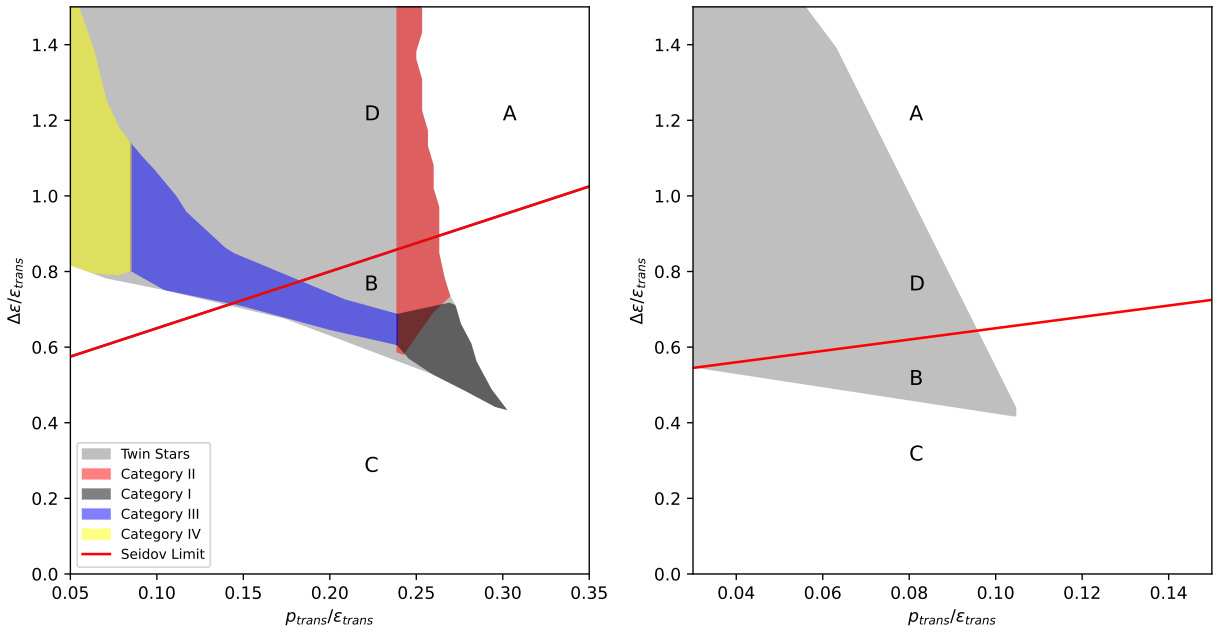

Figure 5.4.: On the left side the parameter space for $c_{QM} = 1$ is shown, on the right the parameter space for $c_{QM} = 1/3$ both sides use the RMF EoS with $m^*/m = 0.65$ as the hadronic crust. The parameter sets leading to twin stars (areas B and D following the Alford classification) are shaded gray. The colorful areas indicate the four categories defined in the following subsection 5.2.1. The parameter spaces leading to twin stars allowing for specific classes of hybrid stars is strongly dependent on the value of c_{QM}. Smaller values for the speed of sound decrease the parameter space significantly. However, none of the four classes of hybrid stars vanish, even for the greatly diminished parameter space of $c_{QM} = 1/3$.

can be found in the first branch. Finally, D covers the case that only the second branch contains hybrid stars (compare fig. 5.3). This places class A and D above the Seidov limit and class B and C below it, which can be seen in figure 5.4, where the Seidov criterion is marked with a red straight line. Note that only the case B and D can contain so-called twin stars, since a connected branch does not allow for two stars with the same mass but different radii. The area covered by classes B and D is shaded gray, with category I-IV (covered in the next subsection) overlaid. It is noticeable that for a more realistic speed of sound $c_{QM} = 1/3$ the parameter space decreases. However, all hybrid star scenarios are still present, which means that using a higher sound speed opens up a greater parameter space to explore without creating any type of solution unique to it. As stated earlier, we will be using a speed of sound $c_{QM} = 1$ for our calculations, strengthening any constraints that we find despite the increased parameter space.
Another important thing to note is that the $\Delta\epsilon/\epsilon_{trans}$ - $p_{trans}/\epsilon_{trans}$ parameter space seems to be nearly independent from the hadronic crust EoS, as Alford et al. find in a similar plot [Alford et al., 2013].

Twin Star Classification by Christian et al.

The categorization by Alford et al. is useful in discussing what types of hybrid stars exist. However, when considering constraints on the equation of state that describes those hybrid stars, it provides no intuitive additional insights. To get a better feeling for the connection between equation of state and the mass radius relation, it is useful to consider the influence of the transition parameters. As outlined in [Christian et al., 2018] the transitional pressure can reliably be correlated with the maximal mass of the purely hadronic stars, while the discontinuity in energy density has a significant influence on the position of the hybrid star maximum in the mass radius diagram.
In figure 5.5 the effects of varying the jump in energy density (left) and transitional pressure (right) are shown for the $m^*/m = 0.65$ equation of state as an example. On the right-hand side $\Delta\epsilon$ is increased from a value of $\Delta\epsilon = 200\text{MeV/fm}^3$ to $\Delta\epsilon = 400\text{MeV/fm}^3$ with $p_{trans} = 60\text{MeV/fm}^3$ being constant. Noticeably the shape of the hybrid star branch remains the same for all values of $\Delta\epsilon$, only its position changes, where high values of $\Delta\epsilon$ move it to more compact solutions and lower values of $\Delta\epsilon$ keep it closer to the hadronic branch. On the left-hand side of the figure, the transitional pressure is varied from $p_{trans} = 10\text{MeV/fm}^3$ to $p_{trans} = 140\text{MeV/fm}^3$ with a constant

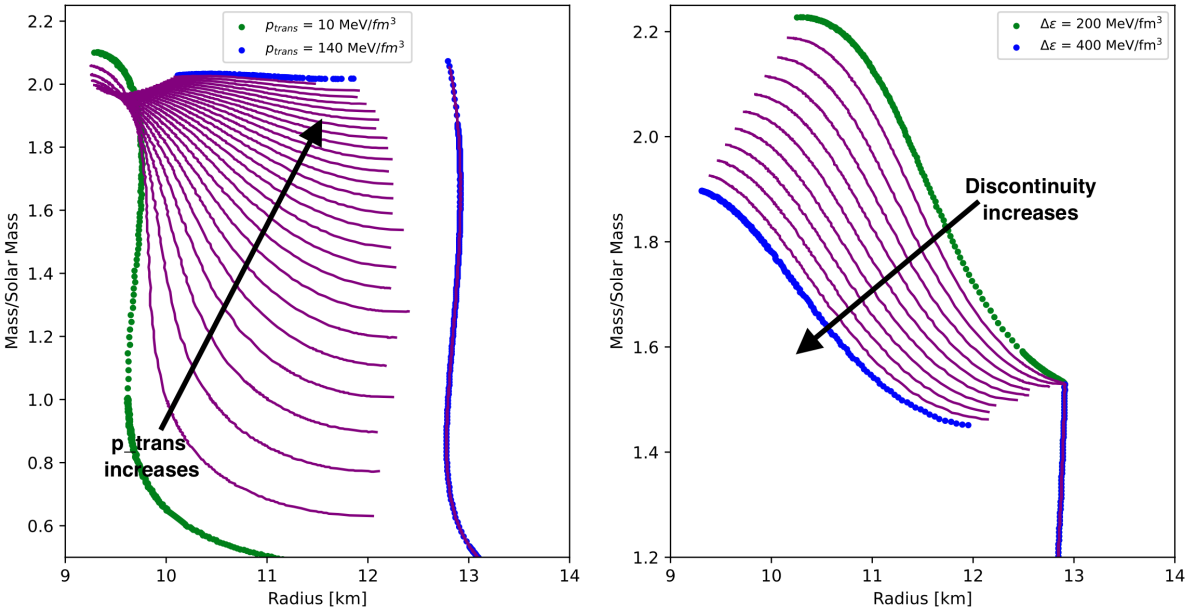

Figure 5.5.: Left: The jump in energy density is fixed to $\Delta\epsilon = 350\text{MeV/fm}^3$ and p_{trans} is increased from $p_{trans} = 10\text{MeV/fm}^3$ (green) to $p_{trans} = 140\text{MeV/fm}^3$ (blue). The second branch becomes steeper with increasing transitional pressure. Right: The transitional pressure is fixed to $p_{trans} = 60\text{MeV/fm}^3$ and the value of $\Delta\epsilon$ increases from $\Delta\epsilon = 200\text{MeV/fm}^3 - \Delta\epsilon = 400\text{MeV/fm}^3$. The shape of the second branch remains similar, but its position changes to more compact solutions for increased $\Delta\epsilon$.

jump in energy density of $\Delta\epsilon = 350\text{MeV/fm}^3$. This is obvious for parameter sets above the Seidov limit, where the hadronic branch loses stability with the addition of quark matter. However, this is also the case for twin star configurations below the Seidov limit (class B following Alford et al.). In these cases, there are usually only a few hybrid stars in the first branch before the sequence becomes unstable. The value of p_{trans} also determines the shape of the hybrid star branch. Low values of transitional pressure will lead to a steep hybrid star branch and high values generate a flat second branch. Surprisingly, the mass value of the hybrid star maximum seems to be determined mostly by the value of $\Delta\epsilon$, with only a small connection to the transitional pressure.
Using this correlation between p_{trans} and the hadronic maximum, as well as $\Delta\epsilon$ and the hybrid star maximum, we can categorize the types of phase transition by their relation to the most massive neutron star, currently known. In the following we will refer to its mass value as $\mathbf{M_{data}}$, which is currently known to be about $2M_\odot$ [Demorest et al., 2010, Antoniadis et al., 2013, Cromartie et al., 2019, Nieder et al., 2020]. Only twin star solutions (i.e. class B and D following Alford et al. [Alford et al., 2013]) will be part of this categorization, as they are the most interesting cases for constraining the EoS. However, the outlined trends are similar for connected branches C.

Category I is defined by both branches having masses higher than M_{data}. This condition can only be satisfied with a high value of p_{trans}, as the first maximum will be too low otherwise. This will necessarily lead to a flat hybrid star branch, generating a characteristic mass radius relation as shown in figure 5.6. If the second maximum has values above M_{data} as well, the energy density discontinuity has to feature relatively small values. Otherwise, the second branch would dip below the set limit. This is in contrast to category II. The maximal masses of the hadronic and hybrid star branch are usually very close to each other in category I, due to the second branch's flatness.

Category II is defined by only the hadronic maximal mass reaching M_{data}. Again, this necessitates high values of p_{trans}, but uniquely allows the values of $\Delta\epsilon$ to become nearly arbitrarily large. A characteristic category II mass radius relation will look similar to category I, with the first branch being indifferentiable and the second branch being as flat as category I, but located at lower masses (see figure 5.6). This feature means, that category II can contain twin stars with the greatest possible radius differences

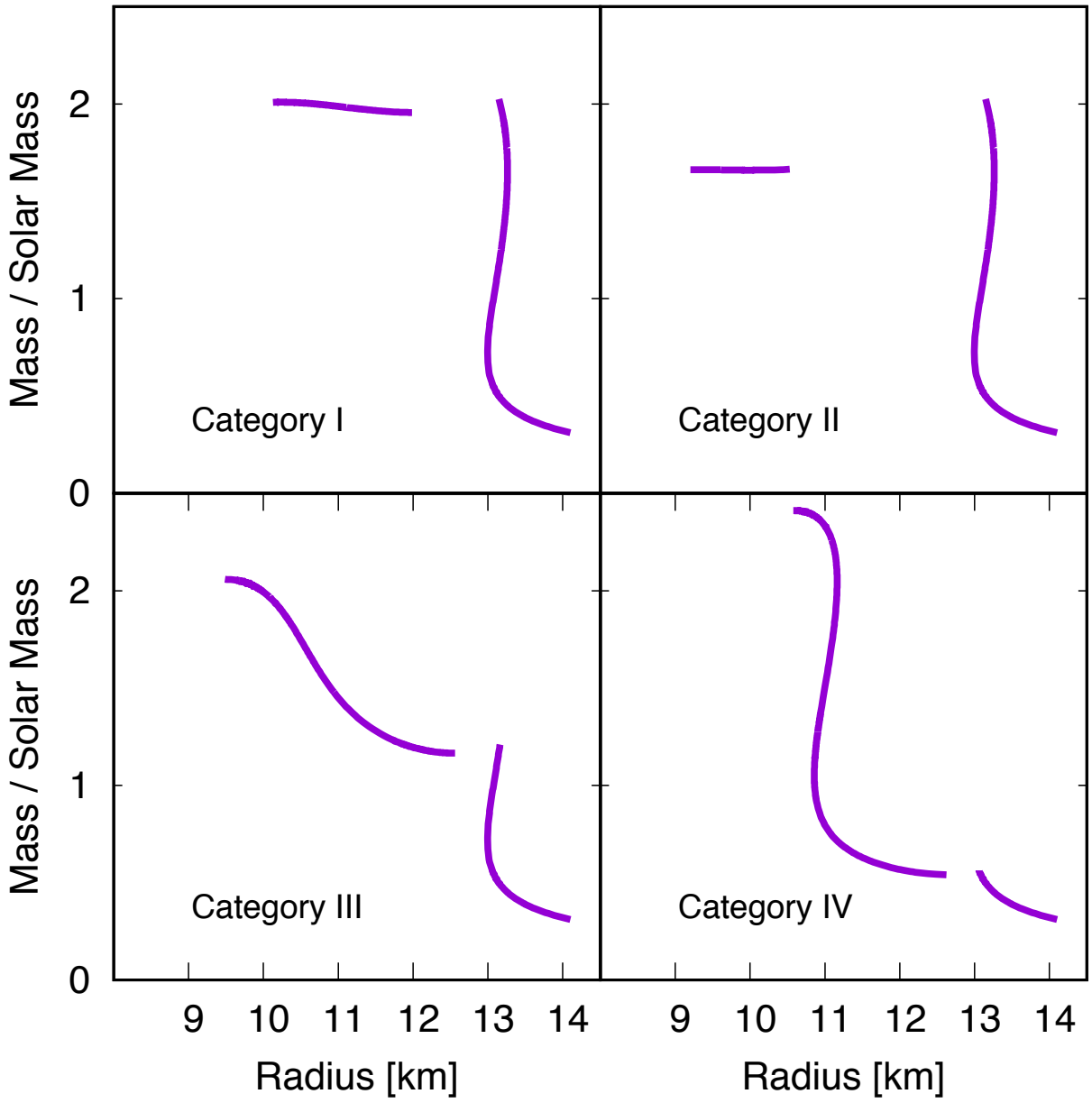

Figure 5.6.: Representative examples for category I-IV with the DD2 equation of state as the hadronic part and a constant speed of sound ($c_{QM} = 1$) in the quark phase. The current value of M_{data} is $2M_{\odot}$.

when compared to all other categories. However, as we will see in section 5.3, it also requires a hadronic EoS that fulfills all current astrophysical constraints without a phase transition.

Category III is defined by the hybrid star maximum meeting or exceeding M_{data}, while the hadronic mass maximum is within the range of known neutron star masses, i.e. not below the mass of about $1.1 M_\odot$ from the J0453+1559 companion [Martinez et al., 2015], but also not above M_{data}. This makes category III the most diverse category, as the second branch can be very steep for early transitions and very flat at high transitional pressures. The transition from category III to category I at high transition pressures is fluid, as well as the transition to category IV at lower p_{trans}. Like category I the values of $\Delta\epsilon$ have to be chosen in a way that does not move the second branch to values below M_{data}. An example with some distance to both adjacent categories is provided in figure 5.6. The mass radius relation on the right side of figure 5.2 is a category III phase transition as well, demonstrating the similar behavior of a twin star solution and a connected branch with similar parameters depicted on the left side of that figure.

Category IV is defined by the hybrid star maximum exceeding M_{data} and the transition taking place before the lowest currently known neutron star mass (currently [Martinez et al., 2015]) is reached, which can only be achieved with a phase transition at remarkably low values. This would mean, that if this category describes nature accurately, all known neutron stars are in fact hybrid stars. Category IV contains the steepest second branch of all categories. Like for category III cases with low transitional pressures, the hybrid star branch runs approximately parallel to the x-axis near the point of transition, but then rises at a nearly constant radius. This behavior is so pronounced that the second branch of a category IV phase transition can be orthogonal to a category I or II second branch. The quark matter equation of state is dominant in this category, due to the early transition. This means that the mass radius relation contains the highest mass values of all categories for a steep quark matter parameterization like ours.

The usefulness of this categorization should become apparent when one considers that the detection of a single pair of twin stars could heavily constrain the conditions of the

Features	Category I	Category II	Category III	Category IV
p_{trans}	high	high	medium	low
$\Delta\epsilon$	medium	high	medium	medium-low
Hadronic maximum	> M_{data}	> M_{data}	< M_{data}	< M_{data}
Hybrid maximum	> M_{data}	< M_{data}	> M_{data}	> M_{data}
Second branch shape	flat	flat	variable	steep

Table 5.1.: These are the features that distinguish category I-IV.

phase transition, as well as provide evidence for the transition itself. This is highlighted in table 5.1, where the features of each category are listed. For example, finding a star with a radius significantly smaller than the radius of M_{data} at lower masses would point strongly towards a category II phase transition, which would constrain the transition parameters to large values of p_{trans} and $\Delta\epsilon$. We refrain from stating concrete values in table 5.1, as the parameters p_{trans} and $\Delta\epsilon$ are depended on the base hadronic EoS and the value of M_{data} is likely to change at some point in the future.

The different categories for the $c_{QM} = 1$ case are shaded over the $\Delta\epsilon/\epsilon_{trans}$ - $p_{trans}/\epsilon_{trans}$ parameter space in figure 5.4. Since the transitional pressure very accurately determines the mass at the first maximum, clear borders on the x-axis are present between the categories. The jump in energy density is not as clearly correlated with the second maximum, leading to some slight overlap in the categories I and II.

5.2.2. Tidal Deformability Effects

The tidal deformability of a neutron star is mostly determined by its equation of state. It is entirely possible that two stars with identical mass and radius, but a different composition might behave differently under the influence of tidal forces. As such, it is not surprising, that the presence of a phase transition would alter the tidal deformability of a neutron star significantly. With the previous subsection in mind, we can already predict how a phase transition could effect the tidal deformability. In subsection 4.3.2 we saw that tidal deformability Λ is proportional to C^{-5}, where $C = M/R$ is the compactness (compare equation (4.44)). Increasing the compactness therefore decreases the deformability significantly. As a result, hybrid stars, which are more compact than regular stars, should be harder to deform.

This prediction is correct, as can be seen in figure 5.7, where some representative

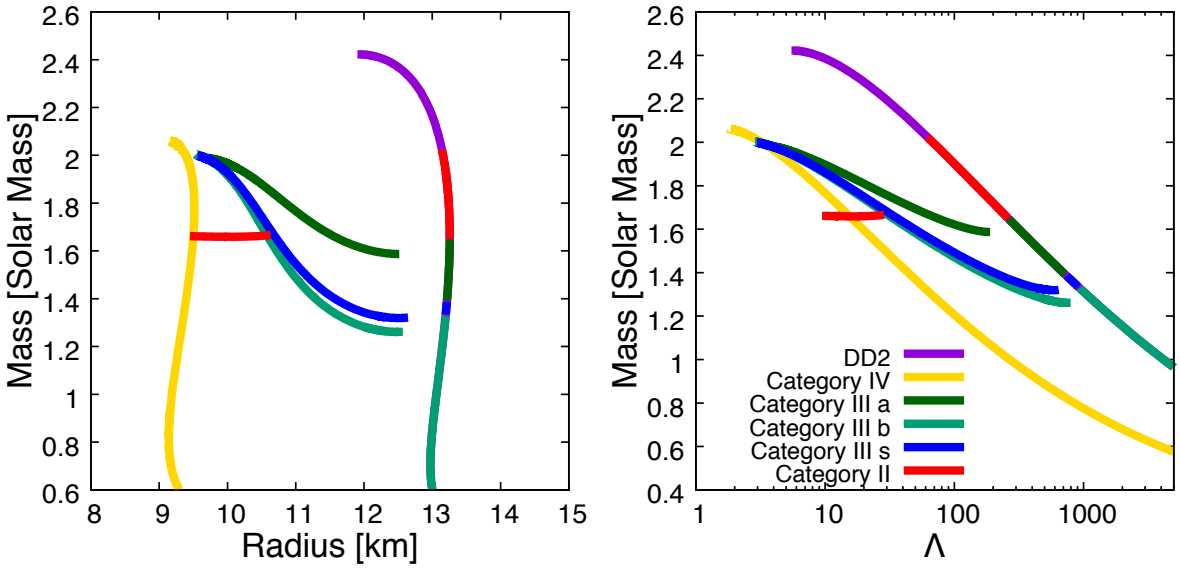

Figure 5.7.: Left: Mass radius relations for category II, III and IV phase transitions with a DD2 hadronic base EoS. Right: The corresponding tidal deformabilities.

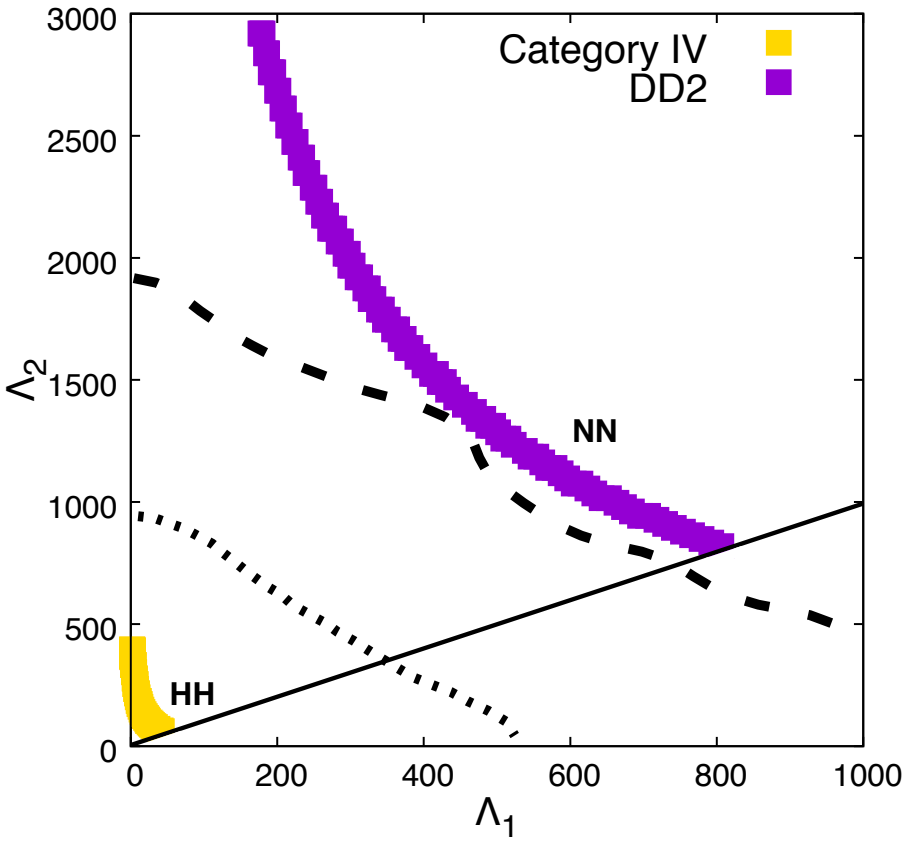

Figure 5.8.: The purple neutron-neutron (NN) line is generated by the DD2 equation of state. The golden hybrid-hybrid (HH) line is category IV. The black dashed line is the 90% credibility limit determined by LIGO and the dotted black line the 50% limit. This figure was published in [Christian et al., 2019].

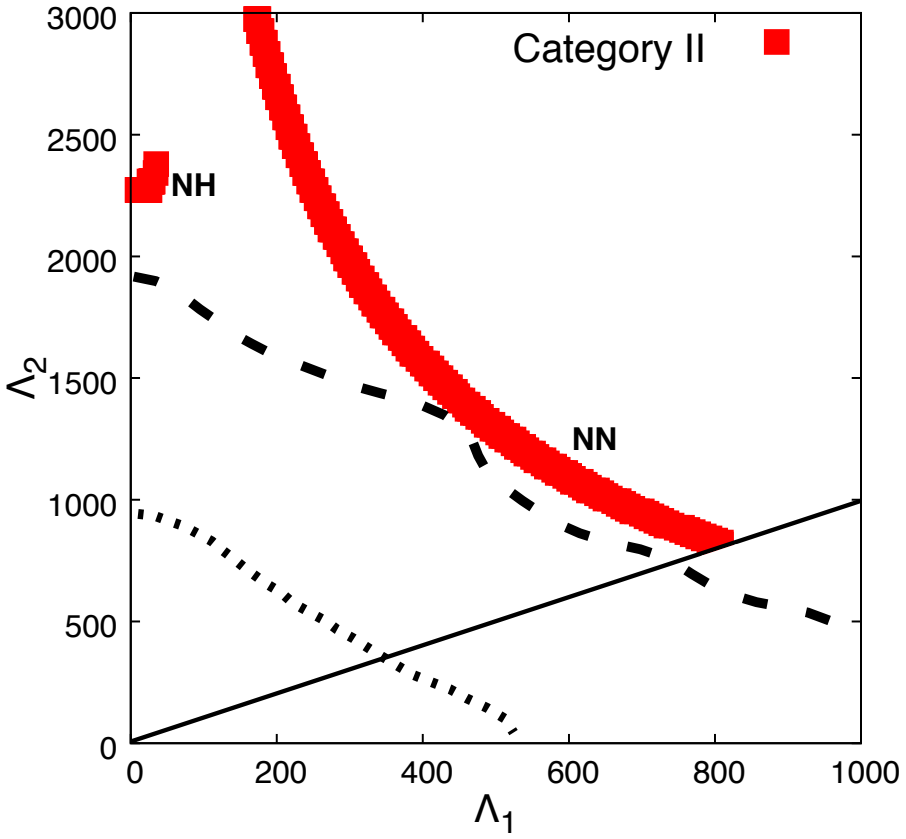

Figure 5.9.: Category II EoSs can generate two separate lines, since neutron-neutron (NN) and neutron-hybrid (NH) combinations can be found that add up to M_{total}. The NN line is at the same location as the DD2 line in figure 5.8. The NH line is located close to the axis, because it can only be generated by combinations of low mass hadronic stars, with high values of Λ and massive hybrid stars, with small values of Λ. This figure was published in [Christian et al., 2019].

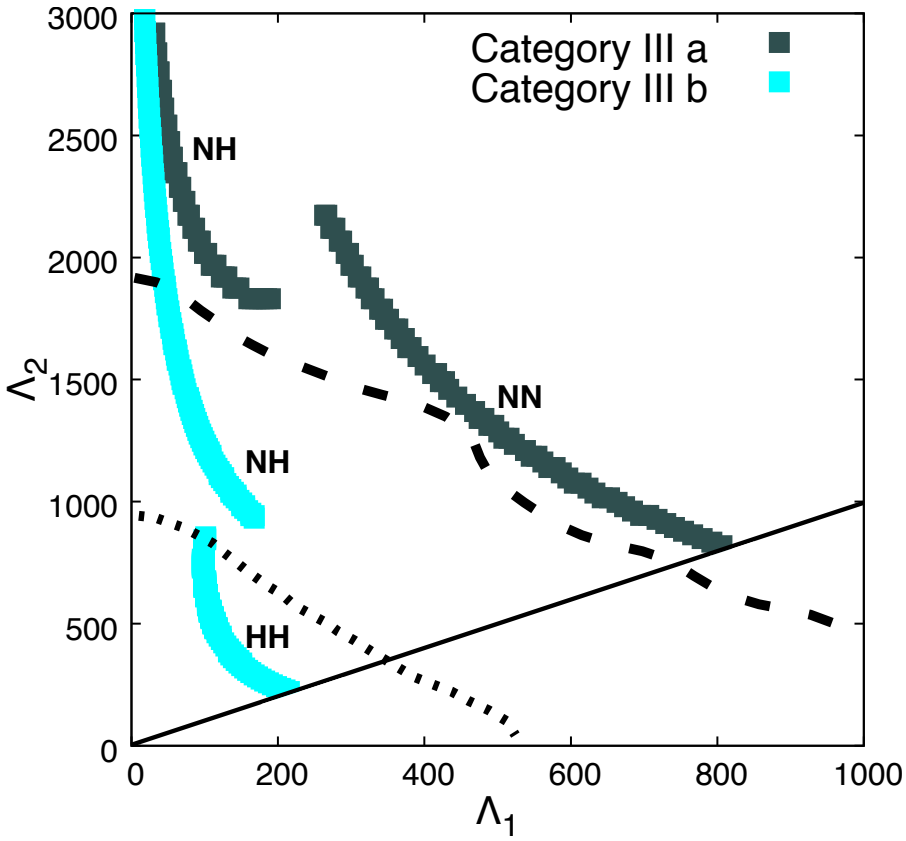

Figure 5.10.: Category III EoSs usually generate two lines. Depending on the transition parameters, these lines are either neutron-neutron and neutron-hybrid star lines (dark green) here denoted by category III a or neutron-hybrid and hybrid-hybrid star lines (turquoise) here called category III b. This figure was published in [Christian et al., 2019].

examples of the four categories are compiled. The DD2 equation of state [Typel et al., 2010] is used for the hadronic mantle, and the speed of sound in the quark phase is $c_{QM} = 1$. Early phase transition solutions like the category IV case (gold) contain the most compact hybrid stars with the lowest values of Λ, while the pure DD2 case (purple) has the highest values of Λ.

As outlined in section 4.4 the tidal deformability of compact stars cannot be measured directly. Instead, a combined value of both participants $\tilde{\Lambda}$ is calculated (see equation (4.45)) and compared to the available areas of likelihood from a merger event, for example in a $\Lambda_1 - \Lambda_2$ plot. Such a $\Lambda_1 - \Lambda_2$ plot contains a single line for a purely hadronic EoS (see figure 4.2). This is because, for a purely hadronic EoS, each mass has only one possible radius. However, if a transition takes place it becomes possible that the stars participating in the merger are either both from the hadronic branch (NN), both from the hybrid star branch (HH) or one from each branch (NH). Due to the vastly different values of tidal deformability between the branches, these possibilities places the results in distinctly different areas in a $\Lambda_1 - \Lambda_2$ plot. This means, if there are twin stars present, more than one line can be generated, where their placement strongly depends on the transition parameters and the total mass M_{total} of the merger event. For example, a category III phase transition featuring a small transitional pressure would only be able to provide a hybrid-hybrid (HH) explanation for a merger event with a high total mass, since the total mass is not achievable with the combination of a hadronic and a hybrid star. However, if the merger event involves a small total mass and the maximal mass of the hadronic branch can be added to a more massive hybrid star this small total mass can be reached and a neutron-hybrid merger (NH) is possible. In this hypothetical, both HH and NH combination would be possible. If the total mass of the merger event is even smaller, a neutron-neutron star merger (NN) could also reach the M_{total}. However, if this is the case it is likely also the case that even the least massive hybrid stars could not be combined to a total mass below M_{total}, therefor only NN and NH mergers could be provided as an explanation for the merger by this EoS. There is one case in which all three possible cases can be provided by the same EoS. This scenario can only be realized if half the total mass is within the range of twin star masses. We provided a formula to predict which kind of merger participants are allowed by a

certain total mass in [Christian et al., 2019], which reads:

$$M_{total} \begin{cases} < 2M_{twin} \Rightarrow NH, NN \\ = 2M_{twin} \Rightarrow HH, NH, NN \\ > 2M_{twin} \Rightarrow HH, NH \end{cases} , \tag{5.17}$$

where M_{twin} is the range of twin star masses. In reality, it is much more useful to consider the chirp mass $\mathcal{M}$ instead of the total mass, as it is much better constrained, though the two quantities are qualitatively nearly interchangeable and M_{total} is less abstract. We will now check the predictions from equation (5.17) for our categories using the data from GW170817 and the same EoSs shown in figure 5.7. GW170817 has a total mass of about $2.7\,M_\odot$. We start with category I and IV, as these are the limiting cases. The hybrid star branch in a category I phase transition has values close to $M_{data} = 2\,M_\odot$. This means a total mass of $2.7\,M_\odot$ cannot be obtained with the combination of a hybrid star and a neutron star[2]. Therefore, the category I line in a $\Lambda_1 - \Lambda_2$ plot based on GW170817 is indistinguishable from the pure case. The NN line from the DD2 equation of state is plotted in figure 5.8 in purple. Contrary to the category I case, a category IV EoS like the gold line of figure 5.7 will necessarily contain only hybrid stars, because the transition takes place at masses that should not be realizable in nature by definition. It will therefore also generate a single line and not multiple ones. Category I and IV can be used as the limiting cases, because all other categories will involve more compact participants than category I and less compact participants than category IV. Note that a category I phase transition could generate a second line for $M_{total} \geq 3\,M_\odot$ in the $\Lambda_1 - \Lambda_2$. However, the NH line would be placed at very high values of Λ_2 and low values of Λ_1 as it would require a hadronic star with astonishingly small mass to participate in the merger. A similar situation arises for the category II case, where the twin star masses are still large (about $1.6\,M_\odot$ in this example) in a range where it's possible to find a hybrid star and a neutron star that can be combined to M_{total}. Nevertheless, these massive hybrid stars can only be combined with very light neutron stars increasing the discrepancy between Λ_1 and Λ_2 and placing the NH line close to the y-axis. This is shown in figure 5.9. In the case of GW170817, the category II neutron-hybrid star line is outside the credibility limit.

2 Remember that the minimal mass of neutron stars that can be generated by supernovae is about $1.0\,M_\odot$

If the transition takes place at lower transitional pressures we move into category III, for which examples are given in figures 5.10 and 5.11. In figure 5.10 two category III case are shown. One with $M_{twin} > 0.5M_{total}$ is plotted in dark green and denoted case (a), and one in turquoise denoted case (b). The letters (a) and (b) refer to the location of the phase transition, where in case (a) the transition takes place "above" the $M_{twin} < 0.5M_{total}$ limit and case (b) "below" it. As predicted by relation (5.17) the category III a case has a neutron-hybrid star line and a neutron-neutron star line, while the category III b case features a neutron-hybrid and a hybrid-hybrid line. Notice, that the neutron-neutron star line of the category III a case is still congruent with the pure DD2 line.
If the transitional pressure used for category III a is decreased further we find a solution where $0.5M_{total}$ is in the range of M_{twin}, which means we should be able to find a neutron-neutron, neutron-hybrid and hybrid-hybrid line generated by a single EoS. This is shown in figure 5.11, where four lines can be found in the $\Lambda_1 - \Lambda_2$ plot. We expected to find only three lines, but the additional fourth line can be interpreted as an expansion of the neutron-hybrid line, here denoted as NH(II). It is generated by the merger of stars, where the more massive star also has a higher tidal deformability. This behavior is found in so-called "rising twins" [Schertler et al., 2000], where a hadronic star is more massive and has a higher radius than its hybrid counterpart. Given the strong correlation of compactness and tidal deformability (equation (4.44)) it is apparent, that rising twins would have a noticeable impact on the $\Lambda_1 - \Lambda_2$ plot. To illustrate this point, we consider figure 5.12, where the mass radius relation of the category III case from figure 5.11 is shown. The upper and lower bounds of M_{twin} are marked in green, the range of stars that can generate a neutron-neutron line is shown by a dashed black line. To indicate, that the compactness of hybrid stars is greater than that of the hadronic stars a red line with the compactness of the hadronic maximum as its slope is drawn. It is evident, that all hybrid stars are above that line and have therefore greater compactness and lower tidal deformability. Furthermore, two stars that would generate a point on the NH(II) line in figure 5.11 are marked, where the more massive one is the maximal mass of the hadronic branch Max_1 with $\Lambda = 739$ and the less massive is a star with mass M_2 and $\Lambda = 387$.
A curious side note is that the compactness of the hadronic maximum seems to be greater or equal to the compactness of the least massive hybrid star for all cases we checked. If this is a coincidence or somehow more explicitly linked to the transition could be explored at some other time.

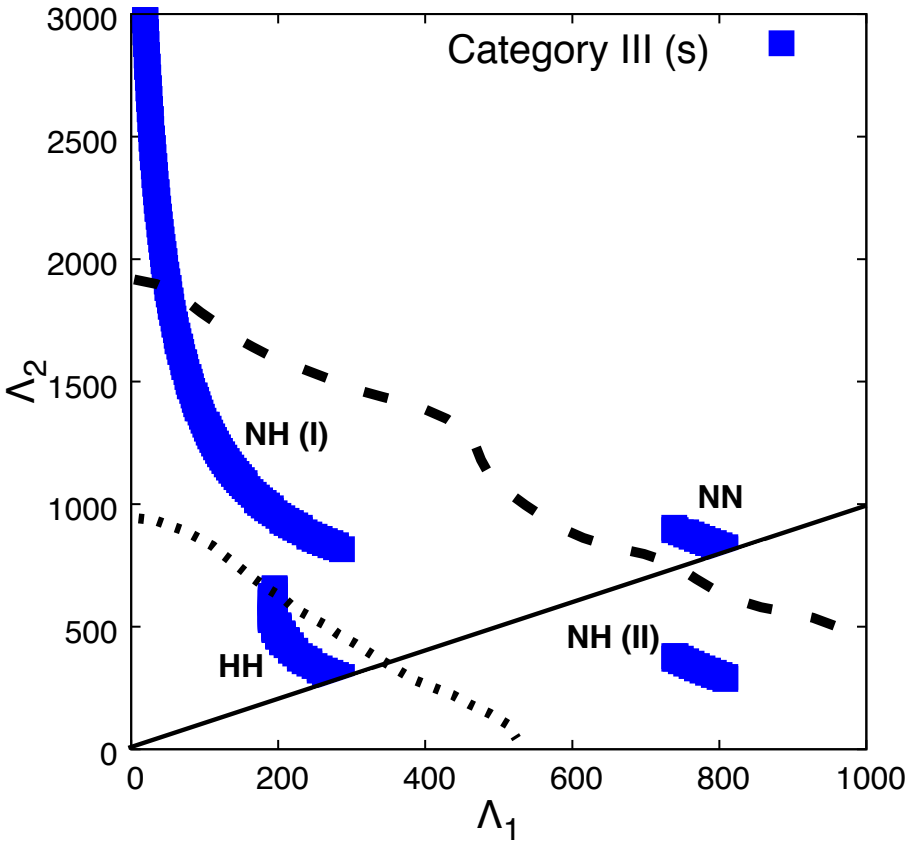

Figure 5.11.: Category III with transition parameters such that 0.5 M_{total} is within M_{twin} will generate a neutron-neutron, neutron-hybrid and hybrid-hybrid line from a single EoS. This figure was published in [Christian et al., 2019].

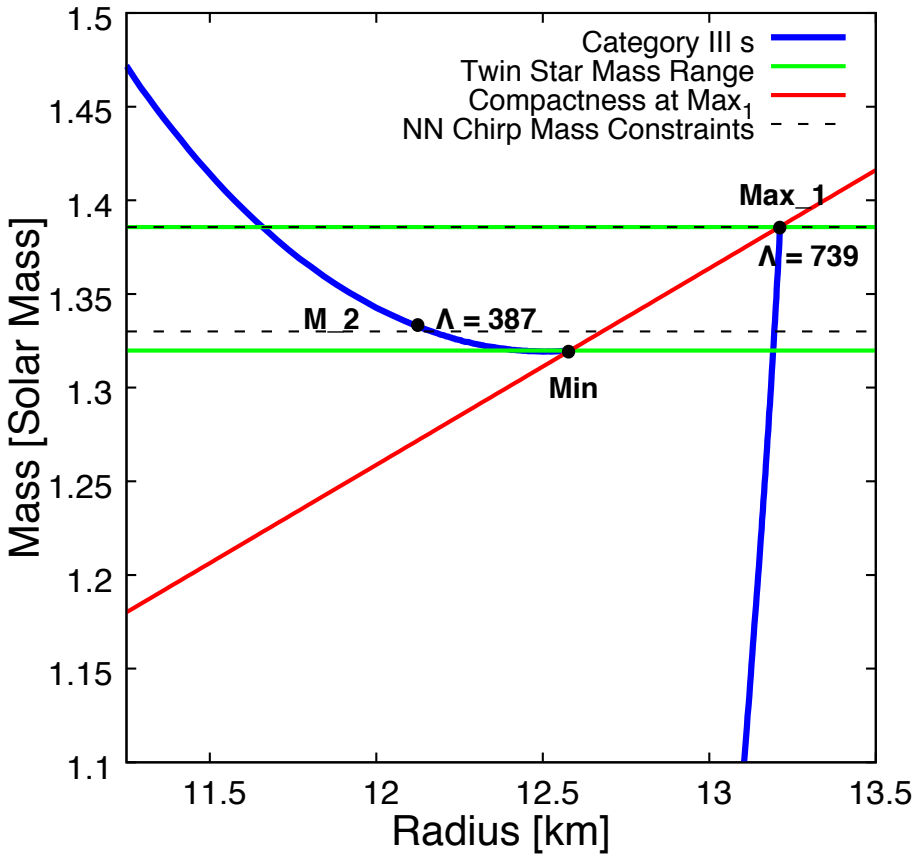

Figure 5.12.: Mass radius relation from figure 5.11 with M_{twin} in green, the area generating the NN line as dashed black lines and the compactness of the hadronic maximum Max_1 in red. Notice that hybrids are always more compact than hadronic stars and feature therefore smaller Λ. This figure was published in [Christian et al., 2019].

5.3. Constraints on the Hybrid Star Equation of State

In the previous section, we elaborated the different possible signatures a phase transition might generate in astrophysical data. In this section, we take the constraints already discussed in section 4.4 and compare them to our predicted signatures for the equation of state discussed in chapter 3. We find, that phase transitions can improve the comparability of an EoS with some measurements, while being challenging to bring into agreement with others.

5.3.1. Mass Constraints on Hybrid Stars

As we have seen previously in subsection 5.2.1 the jump in energy density governs the position of the second branch, where small $\Delta\epsilon$ decrease the distance between the hadronic maximum and the hybrid minimum. Particularly small values of $\Delta\epsilon$ might not even lead to a mass gap, but a connected case. For category III and IV this means, that the maximal mass overall will be determined by the jump in energy density. While the mass constraint for category I and II can be applied in a straight forward way, because it has to be located in the first branch, the maximal mass of category III and IV phase transitions necessarily increases significantly after the phase transition. In [Christian and Schaffner-Bielich, 2021] we investigated the mass limit of category III and IV phase transitions, the results can be seen in figures 5.13-5.17. Here the maximal mass of the second maximum M_2 is plotted as a function of the jump in energy density for EoSs with effective masses from $m^*/m = 0.55$ to $m^*/m = 0.75$ and a suitable collection of transitional pressures. We will use four examples for each effective mass with p_{trans} values that represent the earliest possible transition[3] (purple), the first category III transition (green), the highest p_{trans} of category III (orange) and a transitional pressure between those two (blue). An alternative way of viewing the different transitional pressures would be by mass, i.e. the green line corresponds to about $1M_\odot$, the blue line to $1.5M_\odot$ and the orange line to $2M_\odot$ at the hadronic maximum.
Crucially the figures contain the masses of pulsar J0740+6620 [Cromartie et al., 2019] shaded in red and the less massive companion of the GW190814 merger [Abbott et al., 2020] shaded in blue allowing us to easily compare if the condition set by observation is

3 Earliest p_{trans} compatible with the NICER data from [Raaijmakers et al., 2019] according to [Christian and Schaffner-Bielich, 2020], which is an estimate.

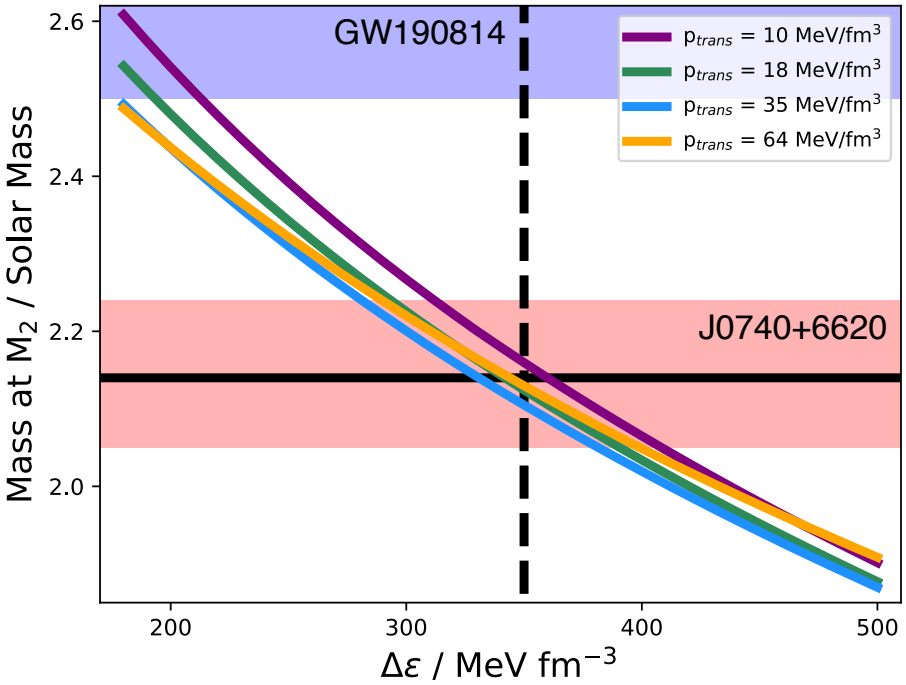

Figure 5.13.: The maximal hybrid mass as a function of $\Delta\epsilon$ with a $m^*/m = 0.55$ hadronic phase is shown. Different transitional pressures are depicted in purple (earliest transition), green (early category III transition), blue (phase transition at about $1.4M_\odot$) and orange (last possible category III phase transition). Note that the orange case is incompatible with the LIGO measurement of GW170817 [Abbott et al., 2019, Christian and Schaffner-Bielich, 2020]. The dashed line indicates $\Delta\epsilon = 350\,\mathrm{MeV/fm^3}$. This jump in energy density always generates a significant mass gap in the mass radius relation, if stability is regained at all. The shaded areas are constraints from GW190814 [Abbott et al., 2020] and J0740+6620 [Cromartie et al., 2019]. The black continuous line is placed at the estimated value of J0740+6620. This figure was published in [Christian and Schaffner-Bielich, 2021].

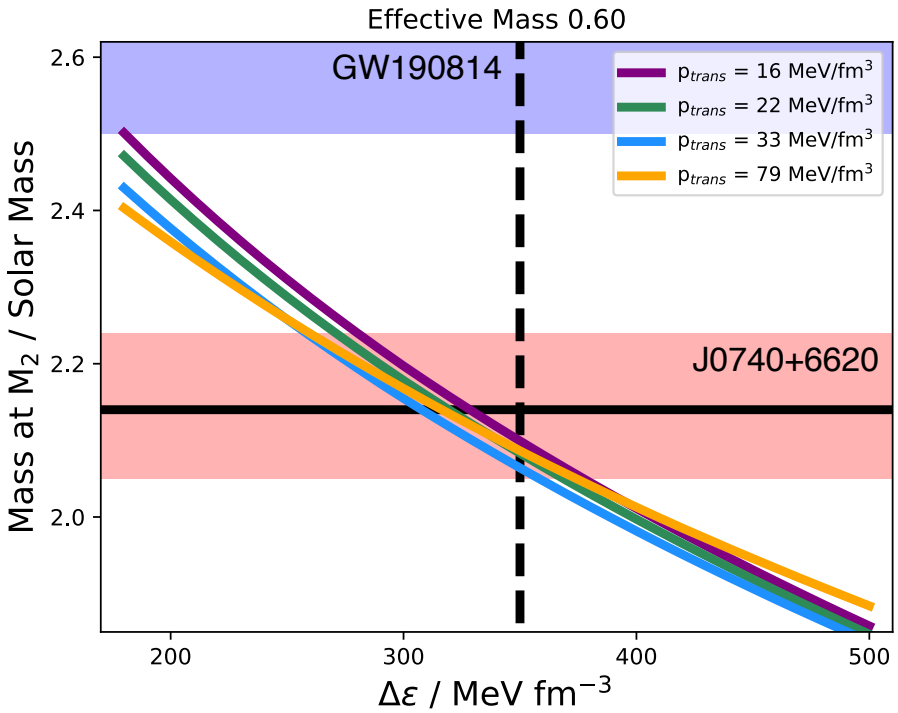

Figure 5.14.: Maximal hybrid star masses generated by different transitional pressures from category III and IV phase transitions of the $m^*/m = 0.60$ case. The $m^*/m = 0.60$ case contains lower values of M_2 when compared to the $m^*/m = 0.55$ case. However, it is still possible to reach the lower limit of the error bar (shaded red) with all category III phase transitions at energy density discontinuities larger than $\Delta\epsilon \geq 350\,\mathrm{MeV/fm^3}$ (dashed line). No combination reaches a mass of $2.14 M_\odot$ (black vertical line) at $\Delta\epsilon \geq 350\,\mathrm{MeV/fm^3}$.

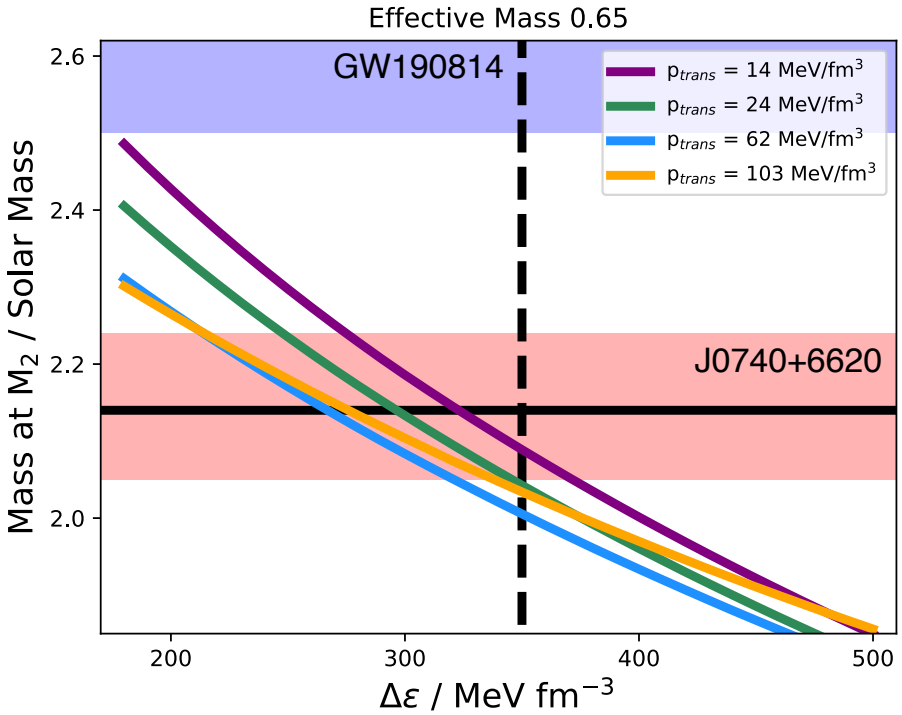

Figure 5.15.: Only the lowest possible transitional pressure meets the mass constraint from J0740+6620 at $\Delta\epsilon \geq 350\,\mathrm{MeV/fm^3}$, which guarantees a sizable mass gap. This figure was published in [Christian and Schaffner-Bielich, 2021].

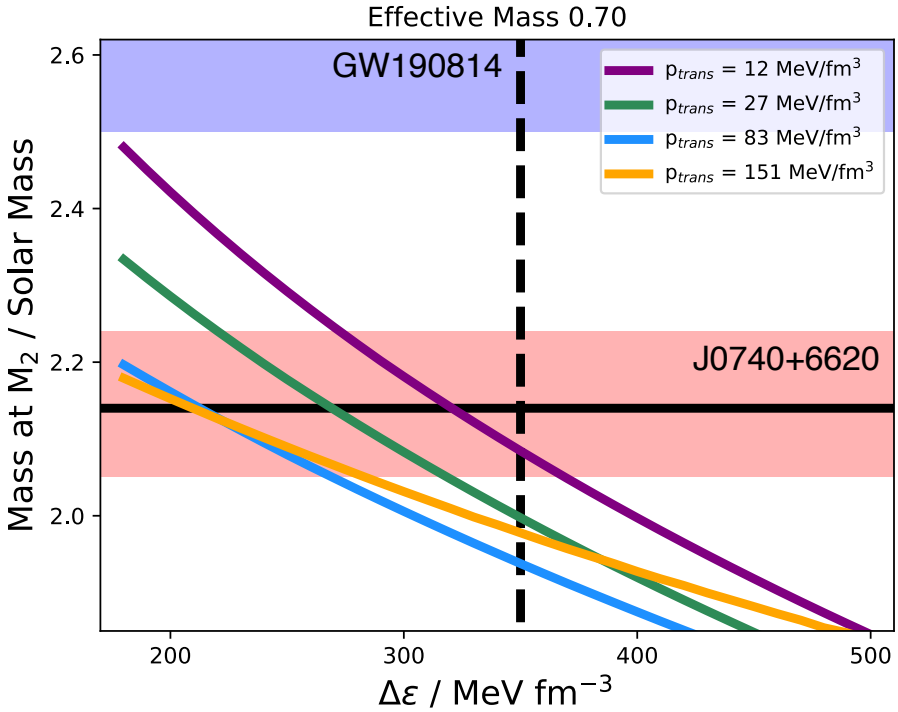

Figure 5.16.: For $m^*/m = 0.70$ only the category IV case $p_{trans} = 12\,\mathrm{MeV/fm^3}$ allows for a configuration with $\Delta\epsilon \geq 350\,\mathrm{MeV/fm^3}$ and a maximal hybrid star mass $M_2 \geq 2.05 M_\odot$. All other cases would not produce visible twin stars and the required hybrid star mass.

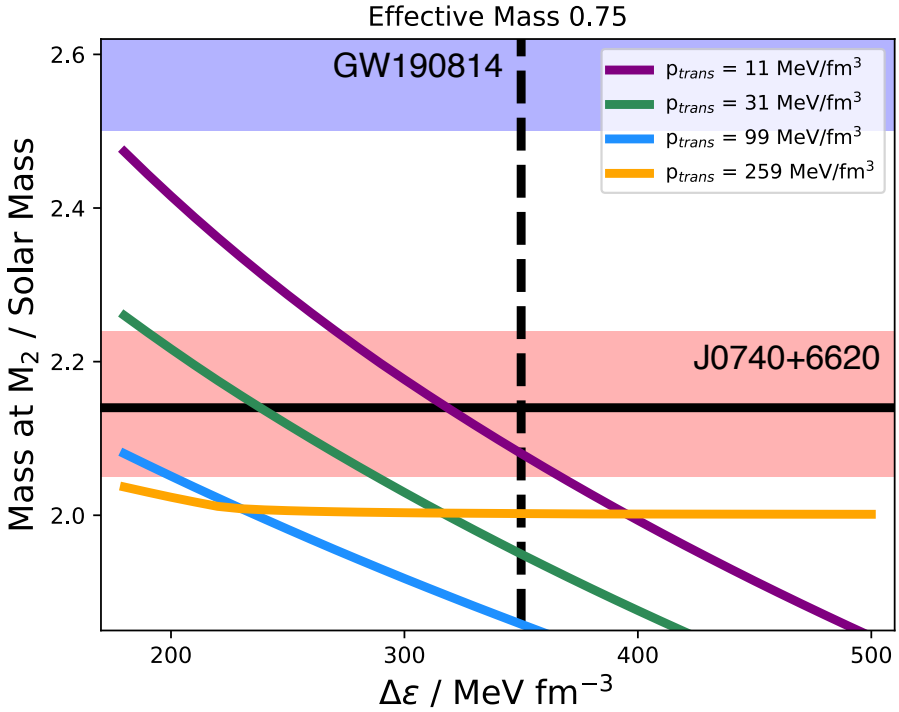

Figure 5.17.: The effective mass $m^*/m = 0.75$ behaves similar to $m^*/m = 0.70$ in that only the category IV case would produce visible twin stars and sufficient hybrid star masses. However, it is the only case in which the upper limit of category III (orange line) fails to reach the lower estimate of J0740+6620, even for small jumps of $\Delta\epsilon$.

met. It should be noted that it is not certain if the companion of the GW190814 merger is the most massive neutron star ever observed or a surprisingly small black hole [Tsokaros et al., 2020, Most et al., 2020, Godzieba et al., 2021, Fattoyev et al., 2020, Dexheimer et al., 2021, Lim et al., 2021, Tews et al., 2021, Tan et al., 2020, Zhang and Li, 2020, Nunes et al., 2020, Blaschke and Cierniak, 2021, Nathanail et al., 2021]. Like in section 4.4 we will touch upon its implications if it were to be considered a neutron star.
Finally there is a dashed vertical line present in figures 5.13-5.17, it is drawn at $\Delta\epsilon = 350\text{MeV/fm}^3$, which is a jump in energy density large enough to guarantee a noticeable mass gap of about $0.1M_\odot$ in the mass radius relation. There are certainly smaller $\Delta\epsilon$ that still generate a mass gap; however, for this discontinuity we can assume with confidence that the effect on the mass radius relation would be detectable independent from the other parameters and the EoS. This means concretely that all EoSs in figures 5.13-5.17 generating lines inside the red box indicating the mass of J0740+6620 **and** to the right of the dashed black line at $\Delta\epsilon = 350\text{MeV/fm}^3$ have masses compatible with J0740+6620 and a significant mass gap, i.e. feature twin stars.
Figure 5.13 depicts the stiffest hadronic EoS with $m^*/m = 0.55$. Since the stiffest EoS will generate the most massive stars all constraints derived for this EoS will also be true for the rest. First, one notices, that an early phase transition, in this case $p_{trans} = 10\text{MeV/fm}^3$, leads to higher masses overall, which is caused by the greater impact of the maximally stiff quark matter EoS. One also finds, that the lines generated by different transitional pressures are not parallel. This is particularly obvious for the orange case closest to category I. For small jumps in energy density, this case has the lowest maximal masses, as one would expect due to the flat second branch associated with such a phase transition. However, for high values of $\Delta\epsilon$ it has higher maximal masses than other phase transitions. This behavior can likely be explained when one considers the corresponding mass radius relation. Since the phase transition occurs at high masses the minimum of the hybrid star branch will also be located at high masses, but the mass will not rise significantly along the second branch. The mass constraints for phase transitions in EoSs with a $m^*/m = 0.55$ can be read directly from figure 5.13. The hypothetical neutron star that might have been a part of the merger GW190814 is reachable, which means if it where to be considered a neutron star it would not rule out the presence of phase transitions. However, the required transitional parameters would not create a significant mass gap, meaning a phase transition would be difficult to differentiate from a purely hadronic EoS, as we will see in the next subsection. We can conclude that all EoSs in our model with higher effective masses will not be able to

generate twin stars for such high mass either.
For a more conventional mass constraint, i.e. J0740+6620, all transitional pressures allow twin star solutions, as the dashed line indicating $\Delta\epsilon = 350\text{MeV}/\text{fm}^3$ is crossed after the lower limit of the red shaded area is reached. Furthermore, we can determine, that the highest possible mass in the second branch that allows for twin stars with sizable mass gaps to be generated with absolute certainty is about $2.2M_\odot$, the point where the purple line meets the dashed line. Note that twin stars at higher masses might be possible, since mass gaps do not require a $\Delta\epsilon = 350\text{MeV}/\text{fm}^3$ discontinuity, but are ensured by it. During this work a neutron star with a mass of $2.35 \pm 0.17\, M_\odot$ [Romani et al., 2022] was reported. This would point towards smaller $\Delta\epsilon$, which are easily compatible with such a massive star but phase transitions would be harder to detect using mass and radius measurements. It should also be noted that there are some uncertainties in this reported mass value, as it belongs to a black widow pulsar, which are notoriously hard to accurately determine due to their accretion.
For figure 5.14, which shows the $m^*/m = 0.60$ case, only the earliest transition (purple) reaches the hypothetical maximal neutron star mass provided by GW190814 in the shown parameter space. It might be possible to reach the required masses if even smaller jumps in energy density are considered (see for example figure 5.21 in the following section), but since there is no consensus in the identity of the GW190814 companion and because such small jumps would not lead to easily detectable particularities in the mass radius relation that point towards a phase transition we will not consider this constraint further.
With the increase of effective mass compared to the $m^*/m = 0.55$ case the maximal masses of the second branch decrease for this EoS. As a result no set of transition parameters with $\Delta\epsilon < 350\text{MeV}/\text{fm}^3$ reaches masses above the stated mass of J0740+6620, which is $2.14\, M_\odot$ [Cromartie et al., 2019]. However, the lower limit is still achievable with $\Delta\epsilon < 350\,\text{MeV}/\text{fm}^3$ for all transitional pressures, which implies, that twin stars are possible for this EoS.
As can be seen in figure 5.15 the $m^*/m = 0.65$ case requires small transitional pressures to ensure twin star solutions under the J0740+6620 constraint. The smallest value of p_{trans} supporting the minimal mass of J0740+6620 for higher jumps in energy density then $\Delta\epsilon = 350\,\text{MeV}/\text{fm}^3$ corresponds to the lower boundary of category III. However, it is important to note, that the line generated by the upper transitional pressure of category III (orange) is closer to the constraint from Cromartie et al [Cromartie et al., 2019] than the line generated by a medium transitional pressure. This is due to the

dynamic already discussed for figure 5.13, where the transition at high masses in the first branch also implies high masses for the minimum of the second branch. Taking into account, that our choice of $\Delta\epsilon = 350\,\mathrm{MeV/fm^3}$ as boundary for twin stars is just a rough approximation we can conclude, that the $m^*/m = 0.65$ case could feature high transitional pressures leading to noticeable twin star solutions in addition to twin star solutions from low p_{trans}. Medium values are unlikely to lead to twin stars for this case. The previously mentioned DD2 equation of state has a very similar mass-radius relation to this case and would follow similar constraints.
The $m^*/m = 0.70$ case heightens the problem of the previous case to the point, where only the purple line of figure 5.16 meets the Cromartie et al. [Cromartie et al., 2019] data point at $\Delta\epsilon > 350\mathrm{MeV/fm^3}$, with no other transitional pressure being close. This means no category III transition featuring twin stars with a significant mass gap and in compliance with this constraint can be generated. Only a category IV solution with a dominant quark phase would meet this constraint. If we increase the effective mass to the highest value we consider this statement remains true, as is shown in figure 5.17. In this latter case we can see that the late category III transition will not generate a second branch for $\Delta\epsilon < 200\,\mathrm{MeV/fm^3}$ at all, which is why we find a horizontal orange line at about two solar masses, where the transition takes place.
We can summarize these findings in table 5.2, as was done in [Christian and Schaffner-Bielich, 2022], where the table as well as figures 5.13 and 5.15 were published. To increase the tables readability the effective masses are listed as "a", "b", "c", "d" and "e" in ascending order. Brackets indicate that a constraint is only met for some parameter set in the respective section. Note that the connected branch in table 5.2 refers only to parameter sets with $\Delta\epsilon > 180\,\mathrm{MeV/fm^3}$. Smaller jumps in energy density will increase the maximal mass enough to satisfy the GW190814 constraint. However, such small jumps would lead to a hybrid star section in the mass radius relation that not only connects to the hadronic branch, but does so without creating a noticeable difference in radius between stars with similar masses. Therefore, it would be nearly impossible to detect them. The NICER constraint will be discussed in the next subsection 5.3.2 and the GW170817 constraint in the subsection 5.3.3 following that. They are already listed, due to them being present in [Christian and Schaffner-Bielich, 2022].

	CI	CII	CIII	CIV	Connected
NICER	abcd	abcd	abcd	(abcde)	abcde
GW170817	cd	cd	(a)bcd	abcde	abcde
2.05 $M_\odot$	abcd	abc	abc	abcde	abcde
2.50 $M_\odot$	/	/	/	/	abcde

Table 5.2.: Effective masses 0.55, 0.60, 0.65, 0.70 and 0.75 correspond to the letters a,b,c,d and e. Instead of the estimated mean value stated by Cromartie et al. [Cromartie et al., 2019] the 1σ lower limit is used ($2.05\,M_\odot$). Likewise, the lower estimate of the GW190814 companion is used ($2.5\,M_\odot$) [Abbott et al., 2020]. A connected branch with a sufficiently small jump in energy density can fulfill all constraints.

5.3.2. Radius Constraints on Hybrid Stars

In this subsection we will investigate the constraints put on equations of state with phase transitions by the NICER radius constraints for the pulsars J0030+0451 [Miller et al., 2019, Riley et al., 2019, Raaijmakers et al., 2019] and J0740+6620 [Miller et al., 2021, Riley et al., 2021, Raaijmakers et al., 2021]. Shortly after the first NICER measurement [Miller et al., 2019, Riley et al., 2019, Raaijmakers et al., 2019] we published an article in which we discussed the possibility to constrain the onset of a phase transition in neutron stars using their radius constraint [Christian and Schaffner-Bielich, 2020]. Under the assumption that a phase transition leading to a $\Delta M = 0.1 M_\odot$ is present we found that the phase transition cannot take place before a central density of $1.4 n_0$ is reached. The argument for this statement stems from the behavior of the second branch under increased jumps in energy density discussed extensively in the previous subsections. High values of $\Delta\epsilon$ move the second branch to lower masses and radii, which are not compatible with the NICER data. To demonstrate this a selection of mass radius relations for a $m^*/m = 0.65$ EoS is plotted in figure 5.18. The transition parameters are stated in units of MeV/fm^3 in brackets following the scheme ($p_{trans}/\Delta\epsilon$). The coloring of the NICER ellipses and mass constraints is identical to the colors chosen in subsection 4.4.2.

Of particular interest is the category IV transition in yellow, which features a transition at central densities slightly larger than $1.4 n_0$. As claimed in [Christian and Schaffner-Bielich, 2020] it is just barely inside the first NICER 2σ error ellipse from Riley et al. [Riley et al., 2019]. Its connected counterpart is shown as the dashed blue line and, due to the decreases discontinuity in energy density, easily inside the ellipse. It is clear,

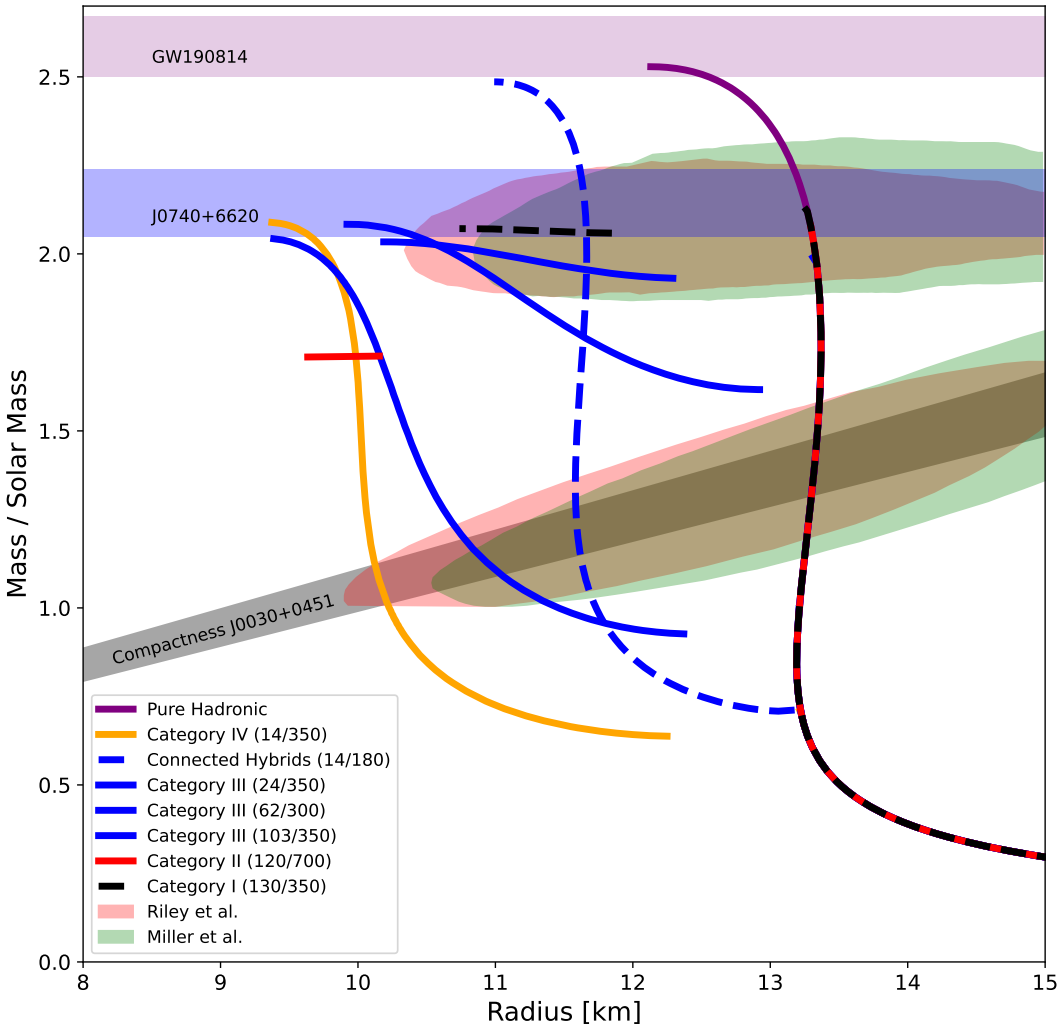

Figure 5.18.: Examples of category I-IV are shown, as well as a connected branch (dashed blue line). Notice that all values of $\Delta\epsilon > 350\text{MeV}/\text{fm}^3$ lead to mass gaps larger than $0.1M_\odot$. The category III example in the middle has a jump in energy density of $300\text{MeV}/\text{fm}^3$, which in this case does not generate a mass gap of $0.1M_\odot$. The constraints from NICER are shaded red (Riley et al. [Riley et al., 2019, Riley et al., 2021]) and green (Miller et a. [Miller et al., 2019, Miller et al., 2021]), and the mass constraints are shaded blue [Cromartie et al., 2019] and purple [Abbott et al., 2020].

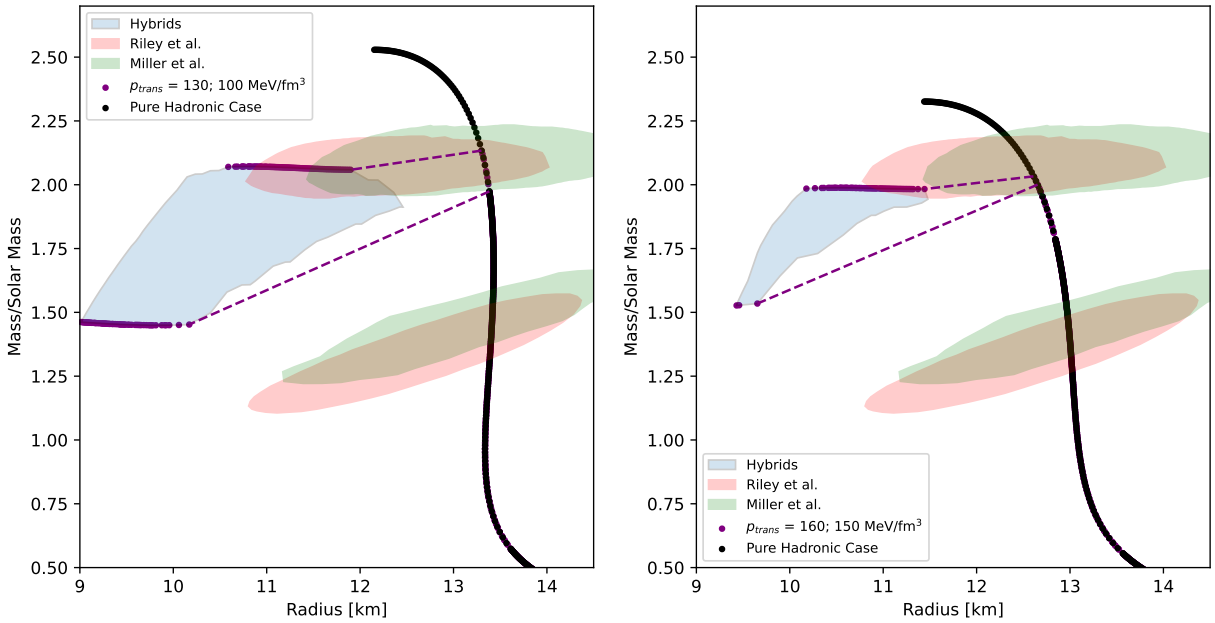

Figure 5.19.: The black continuous line is the pure hadronic case, which satisfies the NICER constraints. If the phase transition takes place after the constraint is met, the mass radius relations will resemble category I and II solutions. On the left side the hadronic equation of state has an effective mass of $m^*/m = 0.65$ and on the right side $m^*/m = 0.70$. These are the only two effective masses, that meet the GW170817 constraint without a phase transition, but still allow for one. At low radii category II solutions populate an area in the mass radius diagram that is inaccessible by pure hadronic EoSs, which is ($R < R_{NICER}$ and $M < 2M_\odot$). This figure was published in [Christian and Schaffner-Bielich, 2022].

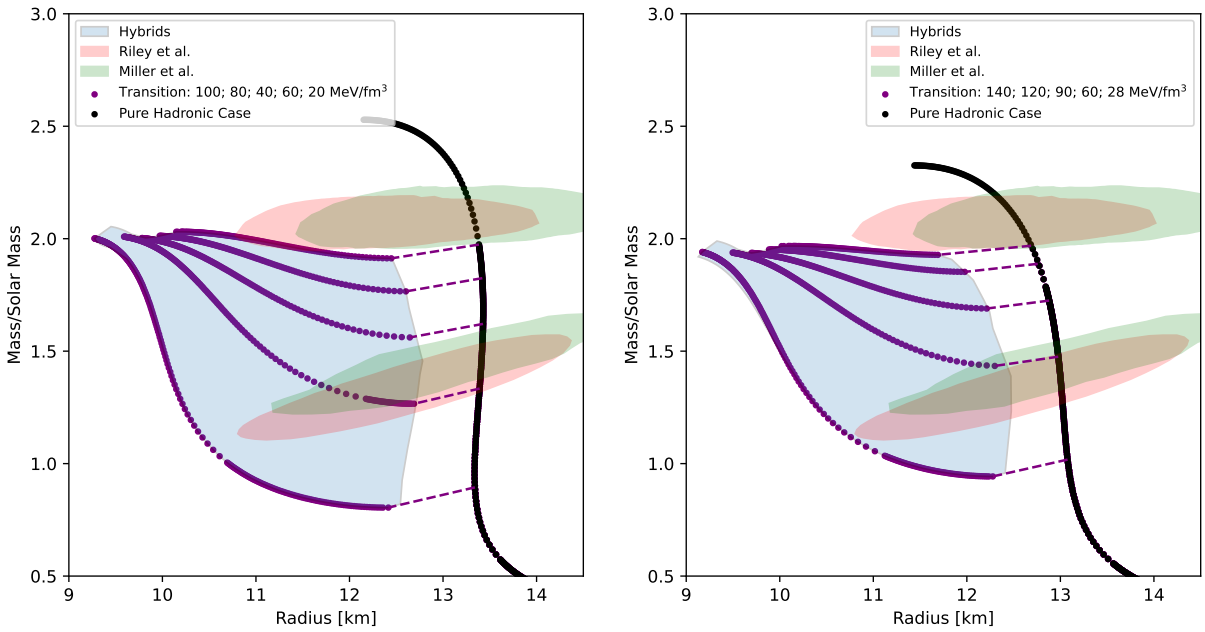

Figure 5.20.: Category III transitions are not compatible with the NICER data of J0740+6620 (upper ellipsis), if a sizable mass gap is demanded, even if the $2M_\odot$ constraint and the GW170817 constraint are met. This figure was published in: [Christian and Schaffner-Bielich, 2022].

that the sensitivity of NICER would not be high enough to differentiate between two similarly massive stars in this case. Category III cases, as shown in blue have a higher transitional pressure and are therefore compatible with the first NICER measurement as well.

The assumption that high transitional pressures are favored is reinforced by the second NICER measurement, which is not only located at higher masses, but larger radii as well [Miller et al., 2021, Riley et al., 2021, Raaijmakers et al., 2021]. Even the category III cases that are compatible with this new measurement have their transition close to $2M_\odot$ (upper blue continuous line) or feature only a small $\Delta\epsilon$ leading to a small mass gap (middle blue continuous line). Only the category I and II cases (black and red) satisfy both constraints no matter the parameter set. This latter point is highlighted in figure 5.19. In this figure, all mass radius relations resulting from parameter sets belonging to category I and II are shown with the hadronic base EoSs $m^*/m = 0.65$ (left) and $m^*/m = 0.70$ (right). Note that the jump in energy density is also limited to $1000\text{MeV/fm}^3 > \Delta\epsilon > 350\text{MeV/fm}^3$. It is clear that all category I and II parameter sets (shaded blue) are within the 1σ NICER constraints[4] .This is because the pure hadronic

4 Here only the 1σ constraint is shown, but this would obviously extend to 2σ confidence as well.

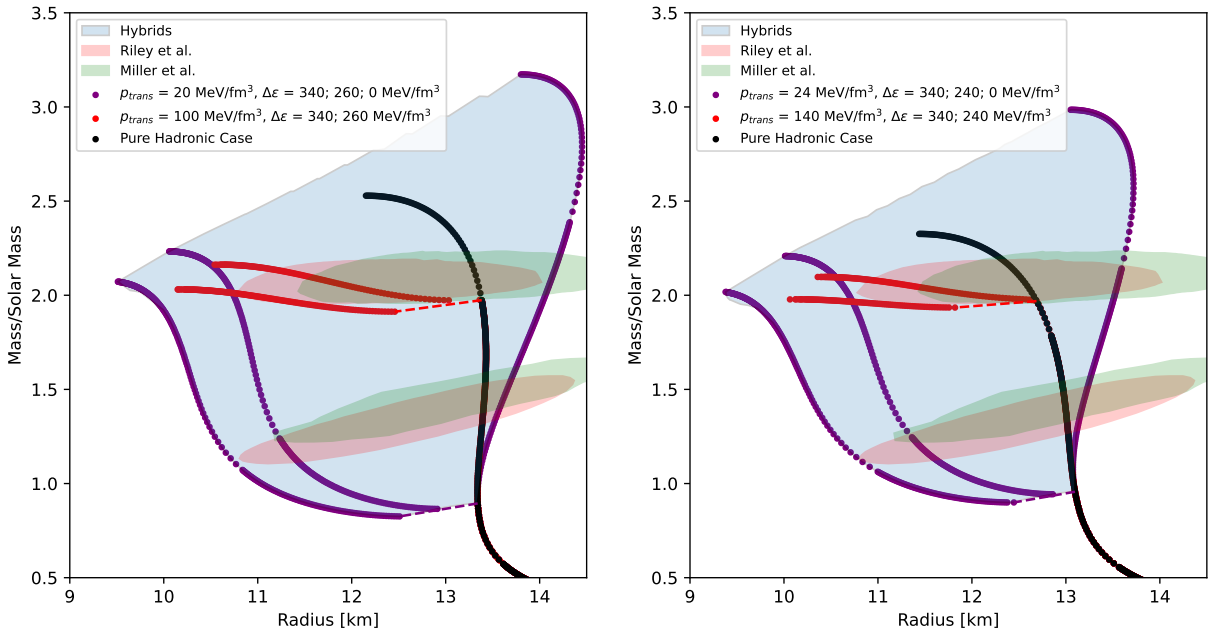

Figure 5.21.: For small jumps in energy density all constraints can be met. However, this will mean that no significant mass gap is present. The boundaries of the mass radius space populated by hybrid stars is formed by a parameter set with a transition at $1M_\odot$, i.e. the lower limit of category III, and a jump in energy density of $340\text{MeV}/\text{fm}^3$ as the lower bound and $0\text{MeV}/\text{fm}^3$ as the upper bound, they are marked by purple lines. An additional purple line in the middle shows the largest value of $\Delta\epsilon$ that is required to grant compliance with the NICER data. For this value, the mass gap is small. The red lines indicate a transition at $2M_\odot$ with a jump in energy density of $340\text{MeV}/\text{fm}^3$ and a jump equal to the one present in the middle purple line. This figure was published in: [Christian and Schaffner-Bielich, 2022].

case (black) already satisfies the constraints. As a result the hybrid star branch can be located at very small radii, which demonstrates that contrary to what is claimed about models without a transition [Pang et al., 2021, Annala et al., 2022, Huth et al., 2022], the radii of hybrid stars cannot be constrained to radii larger than 11km. If a star with a radius smaller than 11km were to be found, it would point towards a phase transition. The area left of the NICER constraints can only be populated by an EoS compatible with the NICER data if a phase transition occurs or other exotic matter is present.
Category III phase transitions do not have a hadronic branch that complies to the mass constraint. They need to achieve it in the hybrid star branch. As can be seen in figure 5.20 this makes them incompatible with the newest NICER constraint, as long as the parameter space for the jump in energy density is limited to $1000\text{MeV/fm}^3 > \Delta\epsilon > 350\text{MeV/fm}^3$. Even higher values of p_{trans} result in second branches that reach the mass constraint at radii that are outside the NICER constraints. If we keep the values of transitional pressure from category III and exchange the limitations on $\Delta\epsilon$ to $350\text{MeV/fm}^3 > \Delta\epsilon \geq 0\text{MeV/fm}^3$ we find figure 5.21. Some limiting cases are highlighted in red and purple. The purple lines show phase transitions with the lowest transitional pressure of category III combined with the highest $\Delta\epsilon$, the last value of $\Delta\epsilon$ that places the mass radius relation outside the NICER constraint and the smallest possible value of $\Delta\epsilon$.
It is abundantly clear, that neither the radius measurement of J0030+0451 [Miller et al., 2019, Riley et al., 2019, Raaijmakers et al., 2019] nor J0740+6620 [Miller et al., 2021, Riley et al., 2021, Raaijmakers et al., 2021] can be used to invalidate the possibility of phase transitions inside neutron stars. However, as demonstrated by the purple line barely reaching the NICER ellipse in 5.21, the jump in energy density is constrained to low values. Despite the purple line representing the largest $\Delta\epsilon$ that is allowed by this transitional pressure the parameter set only results in a radius difference of about 0.5 km between its hadronic maximum and hybrid star minimum. If the transition were to take place at higher values a significant difference in radius might be observable, even if no mass gap is present. This is shown with the red lines in figure 5.21. The discontinuities in energy density correspond to the highest value considered here and the value of the purple line in the middle. Due to the high transitional pressures we find a very flat hybrid star section in the mass radius relation. This leads to a significant amount of stars with similar masses and different radii, despite the small value of $\Delta\epsilon$. This is even true if the branches are connected. An example for this is shown on the right side of figure 5.21, where the point of transition and the maximum of the mass radius relation

are only apart by about $\Delta M = 0.2 M_\odot$ but nearly $\Delta R = 3\,\mathrm{km}$. The underlying EoSs of such cases would be indistinguishable from category I or II phase transitions, but have the potential to be observed.

Before we move on to the constraints on hybrid star EoSs from tidal deformability one might question, why we only considered the cases $m^*/m = 0.65$ and $m^*/m = 0.70$ in the examination of the radius constraints in this subsection. This is because, as we will see, a category I or II phase transition compatible with GW170817 requires that $m^*/m \geq 0.65$ holds true [Christian et al., 2019]. Furthermore, effective masses $m^*/m > 0.70$ cannot generate a second branch outside of category IV [Christian and Schaffner-Bielich, 2021]. We demonstrated in figure 5.21 that phase transitions at such low transition thresholds generate a second branch at radii too small to comply with the J0740+6620 NICER measurement [Miller et al., 2021, Riley et al., 2021, Raaijmakers et al., 2021] unless the jump in energy density is reduced to such a small value, that the branches nearly connect. A parameter set with small p_{trans} and small $\Delta\epsilon$ implies a stiff hybrid branch and thus only small differences in radii between stars of similar mass. Current technology would not be able to detect those differences, therefore it cannot be used to determine if a phase transition is present in neutron stars and we will not include a detailed discussion in this work.

5.3.3. Tidal Deformability Constraints on Hybrid Stars

In this subsection, we will apply the constraints from gravitational wave data to our hybrid star models. This is currently limited to the GW170817 event [Abbott et al., 2018, Abbott et al., 2019]. However, in the near future, tidal deformability might prove to be the most important observable when it comes to confirming or falsifying the existence of twin stars. Landry and Chakravarti [Landry and Chakravarti, 2022] predict that within a week of observation using next generation gravitational wave detectors [Maggiore et al., 2020, Evans et al., 2021] the mass range at which twins occur can be determined within a few percent. Even if no twin stars are found, this would put a strong bound on the upper limit of tidal deformability difference between two stars with nearly identical mass. This could therefore be used to constrain the parameter space of hybrid star equations of state that are not twin stars.

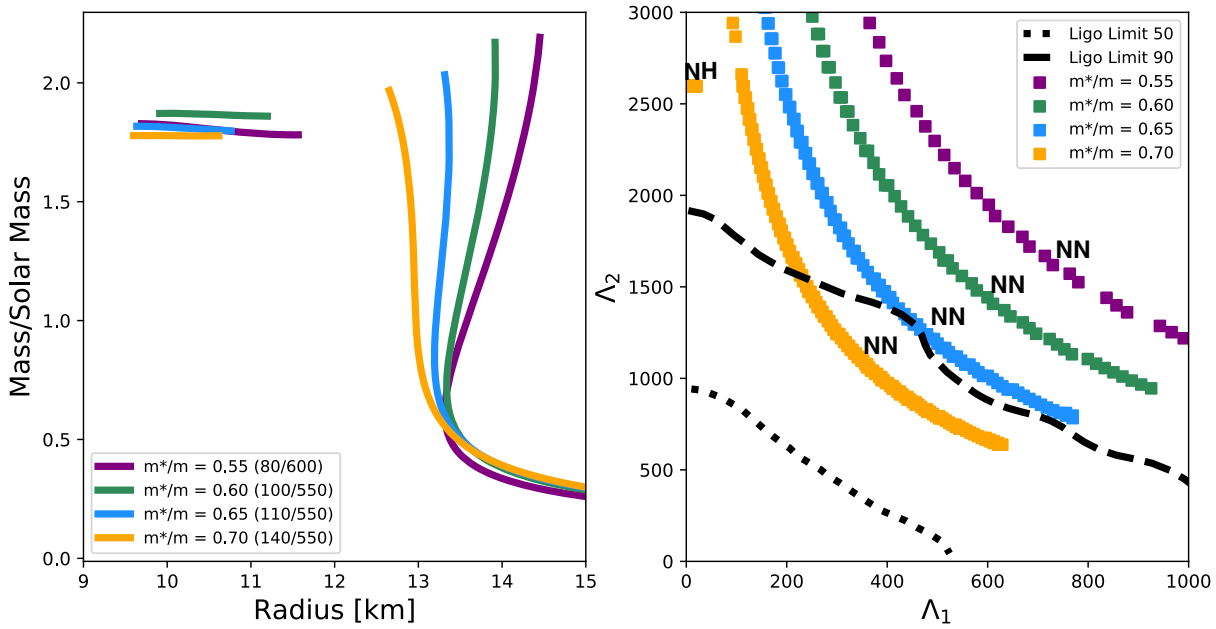

Figure 5.22.: Left: Mass radius relations for category II with varied effective masses. Right: $\Lambda_1 - \Lambda_2$ plot for the category II cases. The compatibility of an EoS with GW170817 is not improved with a category II phase transition. This figure was published in [Christian and Schaffner-Bielich, 2020].

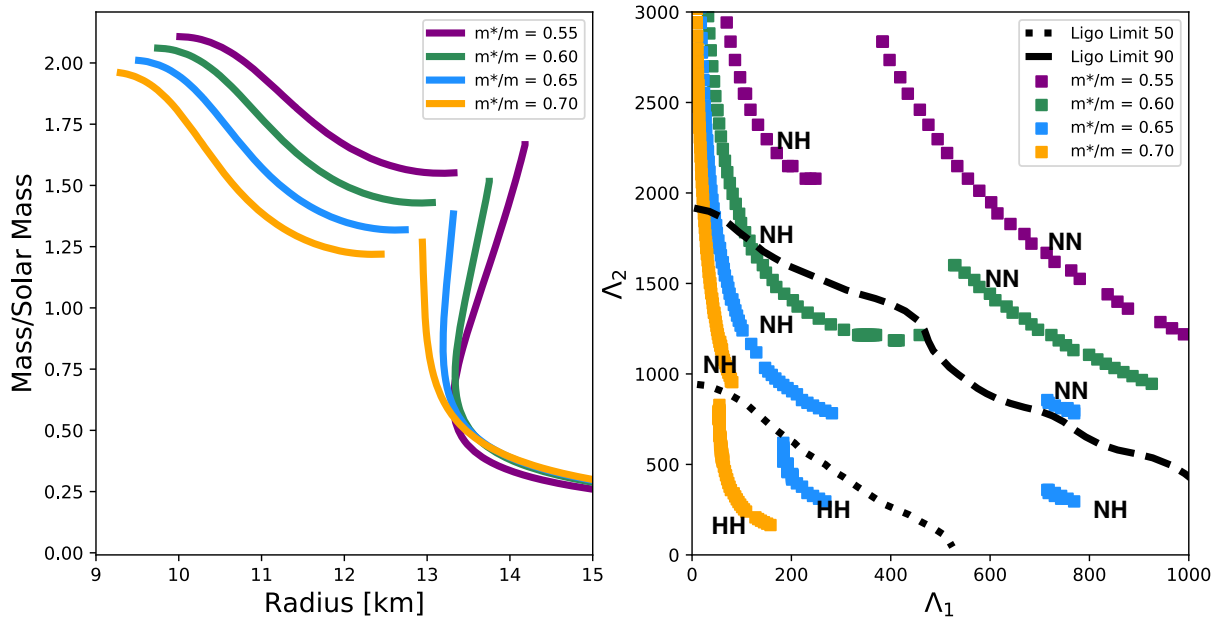

Figure 5.23.: Category III phase transition can generate more compact solutions, which can be seen on the left. This leads to better compatibility with the LIGO data (right). This figure was published in [Christian and Schaffner-Bielich, 2020].

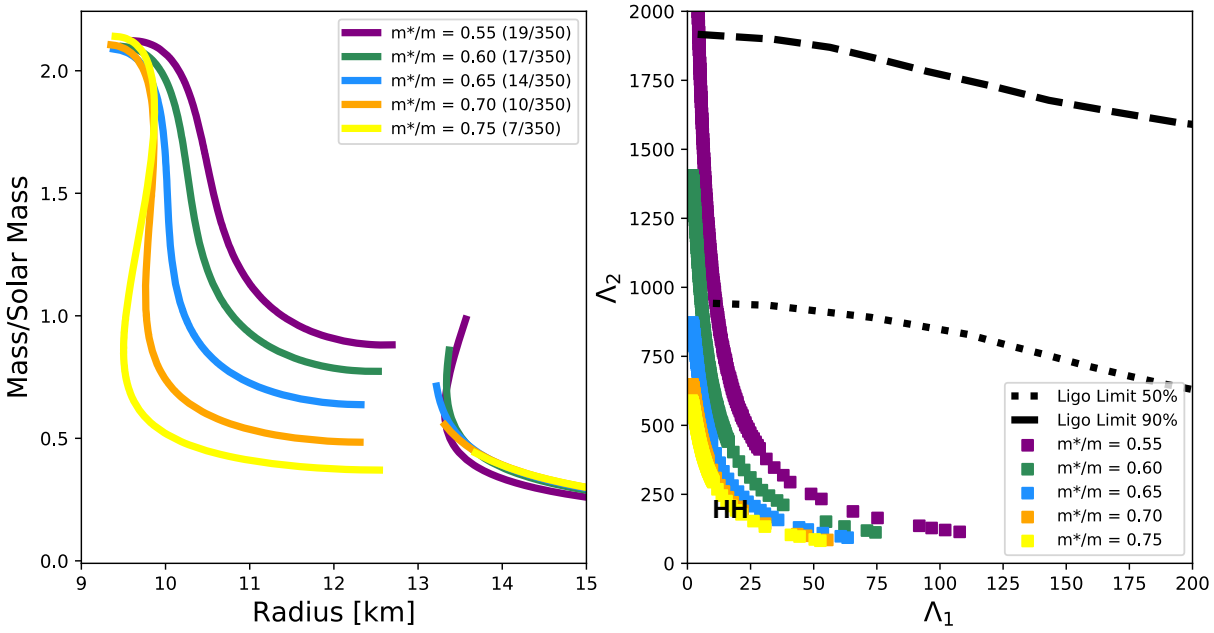

Figure 5.24.: All category IV phase transitions are inside the LIGO credibility limit. This is because the EoS is dominated by the quark phase. This figure was published in [Christian and Schaffner-Bielich, 2020].

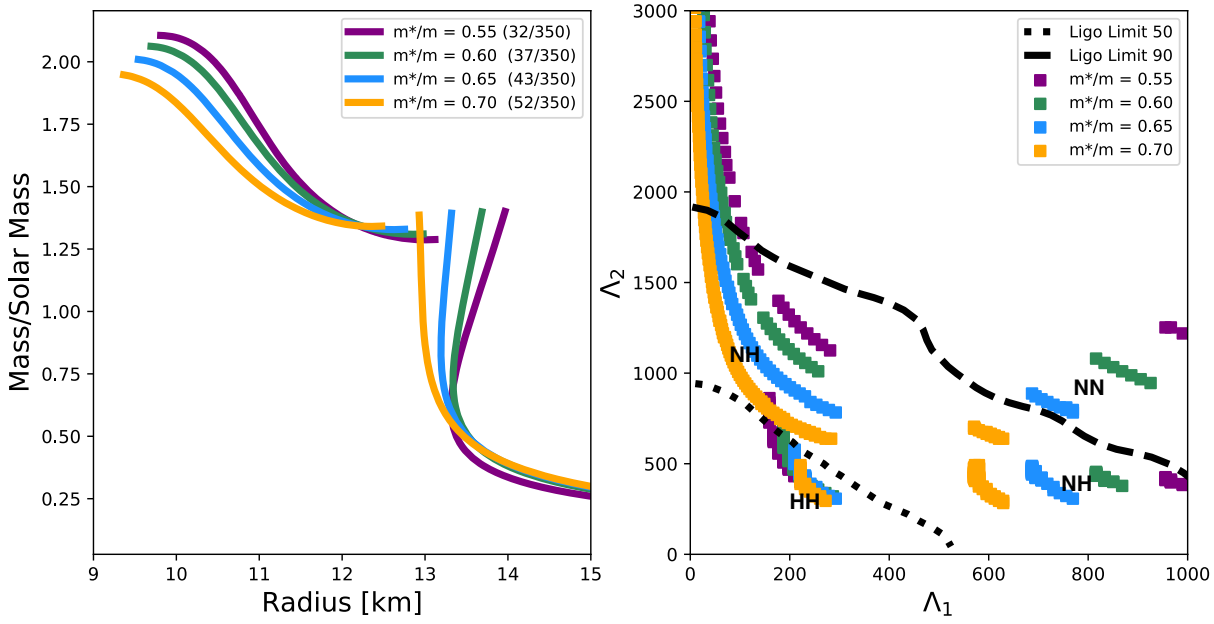

Figure 5.25.: If the parameters of the phase transition are chosen in such a way that twin stars can add up to the total mass all combinations of merger, i.e. hybrid-hybrid, neutron-hybrid and neutron-neutron star mergers, are possible with a single EoS. This figure was published in [Christian and Schaffner-Bielich, 2020].

As discussed in subsection 4.4.3 the GW170817 LIGO/Virgo measurement [Abbott et al., 2018, Abbott et al., 2019] favors compact stars. Usually one has to rely on softer EoSs to find more compact stars, which creates conflict with the mass constraints, since it favors stiff equations of state, which generate higher masses and radii. It has been found, that hybrid stars fit the GW170817 event particularly well [Paschalidis et al., 2018, Alvarez-Castillo et al., 2019, Christian et al., 2019, Montana et al., 2019, Sieniawska et al., 2019], due to the possibility of using two EoSs in one. We established in section 5.2 that in a $\Lambda_1 - \Lambda_2$ plot with the GW170817 credibility limits, multiple lines can appear for hybrid star equations of state. The lines containing hybrid stars contain more compact stars and are therefore more compatible with the gravitational wave data. In the following, we will analyze the category II-IV cases for the effective masses $m^*/m = 0.55 - 0.70$ in detail. We leave out the category I case, as it is identical to the purely hadronic case outlined in subsection 4.4.3, due to category I hybrids being too massive to fit the data. The parameter sets for the transition will be chosen to be as close together as possible. This way, we can be sure that the stiffness of the hadronic EoS will be the determining factor in the differences between the results. If the parameter set is not exactly identical for all cases, the values will be stated in brackets following the scheme $(p_{trans}/\Delta\epsilon)$.
Figures 5.22-5.25 follow the same structure as 4.2 by showing the mass radius relation on the left side and the corresponding $\Lambda_1 - \Lambda_2$ plot on the right side. The EoSs of figure 5.22 feature a reasonably high jump in energy density, placing them unmistakably in category II. As we have discussed in section 5.2 this kind of phase transition generates a neutron-hybrid line close to the y-axis. However, the neutron stars that form this line are not compact enough to meet the constraints. This means, that category II phase transitions are only compatible with the GW170817 data point if their base hadronic EoS already is, like is the case for $m^*/m \geq 0.65$. If we were to increase the value of $\Delta\epsilon$ the hybrid star masses would decrease, allowing us to pair them with more compact neutron stars. It might be possible for the stiffer EoSs to meet the LIGO/Virgo constraint under such conditions, but the values of $\Delta\epsilon$ would have to be enormous and the resulting signature in the tidal deformability would not be observable.
Figure 5.23 is more interesting, because for this case the $m^*/m = 0.60$ EoS becomes viable. The parameter set for it generates a twin star mass of about $1.5\,M_\odot$ for the $m^*/m = 0.60$ case, which makes it possible to form a neutron-hybrid line inside the credibility limit. The transitional pressure could be increased to find more massive twin stars that are still compatible with GW170817 for this case. However, this would only work for category III phase transitions up to a hadronic maximal mass of about $1.8 M_\odot$.

The cases $m^*/m = 0.65$ and $m^*/m = 0.70$ have not only a neutron-hybrid line inside of the credibility limit, but a hybrid-hybrid line as well, reaching even the 50% limit instead and not only the 90% limit. The $m^*/m = 0.55$ EoS is still too stiff to satisfy the constraint. However, if we decrease p_{trans} further we move into category IV solutions shown in figure 5.24.
These equations of state generate only hybrid-hybrid solutions, since category IV is defined by the fact, that only hybrid stars can be observed. The resulting lines in the $\Lambda_1 - \Lambda_2$ plot are clearly inside the LIGO/Virgo constraint and nearly congruent for all hadronic EoSs. This is because the equation of state is dominated by the quark phase, due to the early transition. It is even possible to find a suitable phase transition for the $m^*/m = 0.75$ case (yellow), which usually cannot feature twin stars, due to its softness. To demonstrate this point, the $m^*/m = 0.75$ case has a significant higher transitional pressure than the other EoSs and still is clearly inside the credibility limit. It is somewhat surprising that the hybrid-hybrid line of the $m^*/m = 0.75$ case is still nearly congruent with the remaining EoS, even though the corresponding mass radius relation is vastly different. This might be because the tidal deformability is strongly influenced by the crust equation of state, which is identical for all cases, while the rest of the EoS is dominated by the quark phase, which, again, is identical with $c_{QM} = 1$. Note that it is possible to make any hadronic EoS fit the LIGO/Virgo data of GW170817, if a phase transition is included and placed suitably early. This is of course not a very helpful finding for particularly early phase transitions, where it becomes a statement about the suitability of the quark matter EoS instead of the hadronic one.
The compatibility of the EoSs and categories with GW170817 is summarized in table 5.3, where y indicated, that a case is compatible, o indicates that a case is partially compatible and x indicates, that it is not compatible. Figure 5.25 serves as a demonstration, that it is always possible to generate four lines in the $\Lambda_1 - \Lambda_2$ plot, if the twin star masses contain $0.5M_{total}$, as stated by equation (5.17). The total mass of GW170817 is about $2.7M_\odot$, therefore the maximal hadronic star in figure 5.25 was chosen to be $1.35M_\odot$. This of course means, that all EoSs shown there are compatible with GW170817, as all hybrid-hybrid lines are.

What makes this analysis particularly interesting is its interplay with the NICER findings and mass constraints discussed in the previous subsections (see also table 5.2), because the results point in different directions. In order to make EoSs that struggle to satisfy the NICER and mass constraints viable, we usually need to increase the

Category	0.55	0.60	0.65	0.70	0.75
I	x	x	o	y	n.a.
II	x	x	o	y	n.a.
III	y	y	y	y	n.a.
IV	y	y	y	y	y

Table 5.3.: This table shows which categories of twin stars are compatible with the gravitational wave event GW170817 based on the effective masses m^*/m of their hadronic EoS. We consider the 90% credibility limit, where y indicates that the category matches the constraint, x indicates that it does not and o is used when the EoS generates a line directly at the credibility limit.

transitional pressure and reduce the jump in energy density. EoSs that are outside the GW170817 credibility limit require the opposite treatment. New data points from both sources might shift this dynamic in the near future.

5.4. Additional Considerations

In this section we will discuss a few topics related to hybrid and twin stars that did not fit within the other sections, such as production scenarios 5.4.1, the recent HESS J1731-347 [Doroshenko et al., 2022] measurement and alternative explanations for potential data points 5.4.2.

5.4.1. Production Scenarios of Hybrid Stars

This work is focused on determining what observables can be reliably used to determine if a phase transition is present in neutron stars, and how the parameter space of such a phase transition could be constrained from simple astrophysical data points. For this purpose, the way in which hybrid stars themselves are produced is secondary. Nevertheless, if it were to be demonstrated that hybrid stars have no way to be produced in the first place, the search for observables marking their existence would be pointless. For this reason we take some time to discuss some possible production scenarios in this subsection.
Since the phase transition happens at a critical pressure p_{trans}, the easiest way to explain

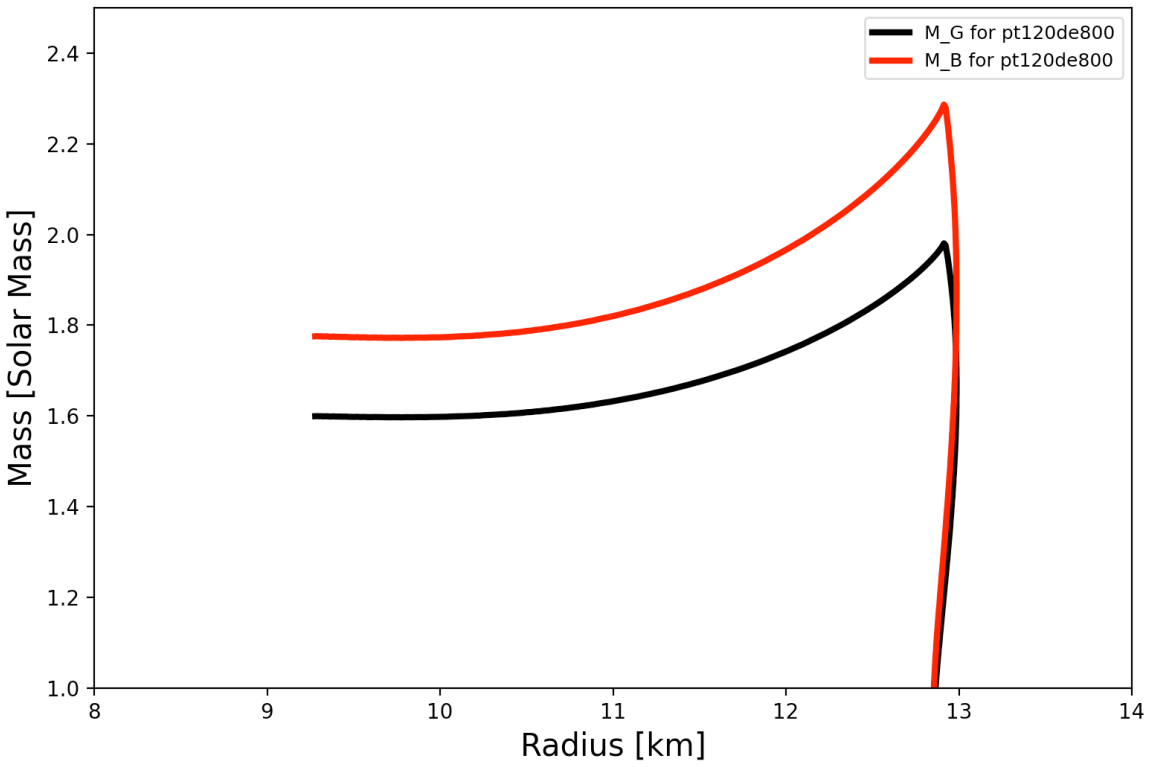

Figure 5.26.: Baryonic mass in red, gravitational mass in black of a category II phase transition.

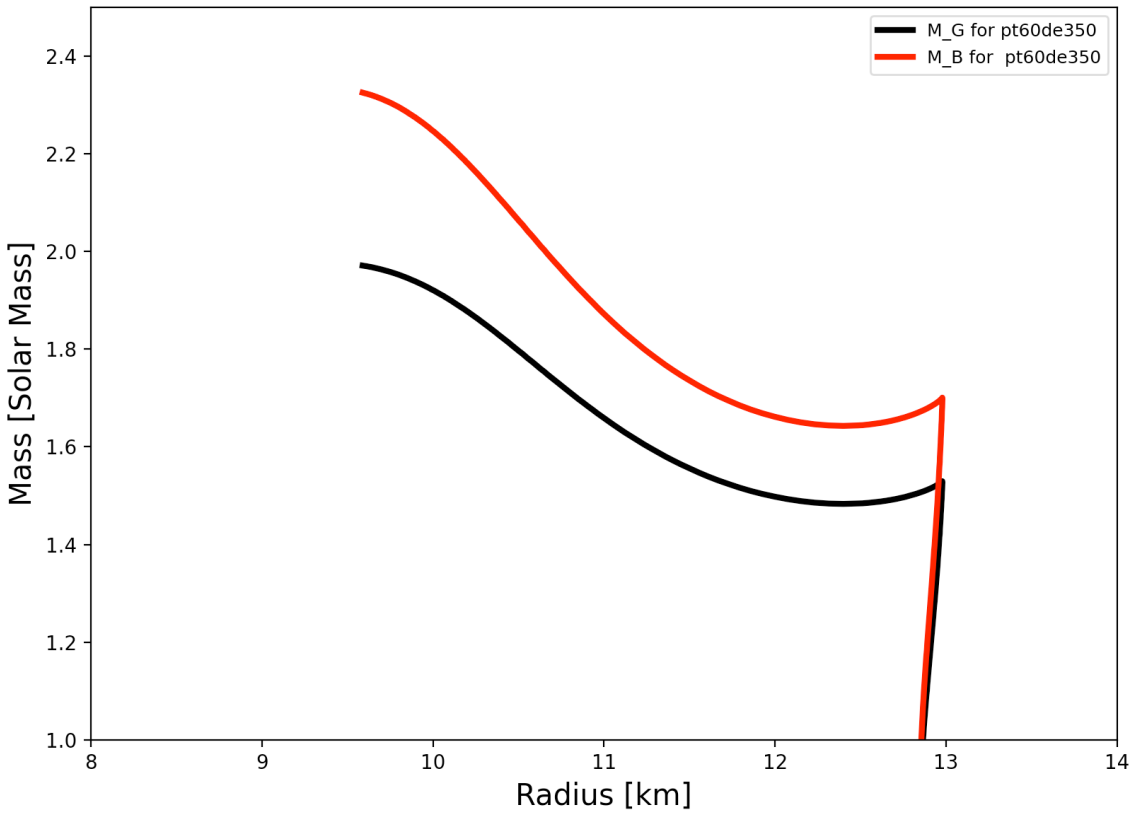

Figure 5.27.: Baryonic mass in red, gravitational mass in black. This typical category III case suggests that the baryon mass in the hybrid star branch can be significantly bigger than in the hadronic branch. However, category III phase transitions with sizable mass gaps are not compatible with NICER data.

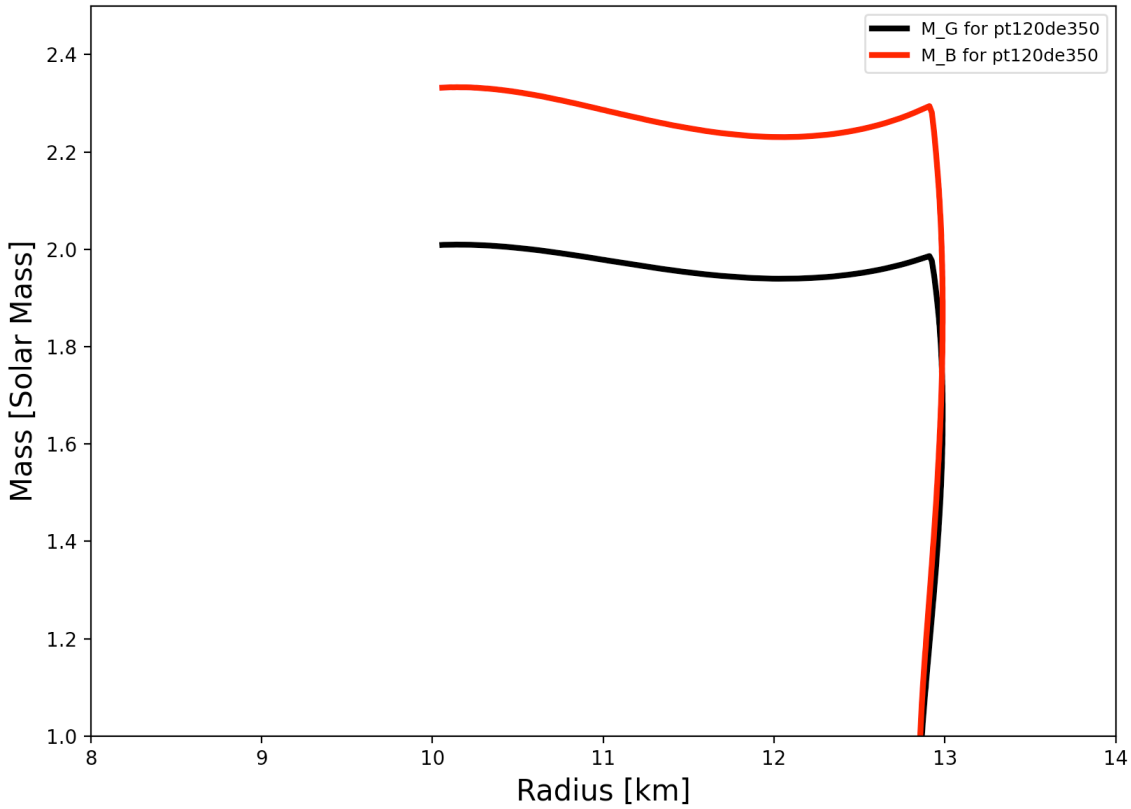

Figure 5.28.: Category I phase transition, which are allowed by NICER data, have larger baryonic masses in their hybrid star branch than the maximum of the hadronic branch. This implies a bigger baryon number and thus that the hybrid star could be generated by accretion.

the creation of a hybrid star would be to find a scenario in which the central pressure of a star is increased to a critical pressure. This could be done by the accretion of mass from a companion star onto the neutron star. However, in this process the baryon number of the star would increase, which in turn means that a star in the hybrid branch would need a larger baryonic mass than a star in the hadronic branch. In order to check if this is the case, let us take a look at how to approximate the baryon density in the quark phase of our model[5]:

$$n_B = n_{trans}^{QM} \sqrt{\frac{\epsilon + p}{\epsilon_{trans} + p_{trans}}}, \tag{5.18}$$

where n_{trans}^{QM} is the baryon density at the point of transition in the quark phase [Drischler et al., 2021]. Note that unlike the baryon number n_B the baryon chemical potential μ_B has the same value in the hadronic and the quark phase at the point of transition, due to the nature of the Maxwell construction. With this information, we can determine the value of n_{trans}^{QM}. We use:

$$\mu_{trans} = \frac{p_{trans} + \epsilon_{trans}}{n_{trans}^{HM}} = \frac{p_{trans} + (\epsilon_{trans} + \Delta\epsilon)}{n_{trans}^{QM}}, \tag{5.19}$$

which leads us to:

$$n_{trans}^{QM} = \frac{p_{trans} + (\epsilon_{trans} + \Delta\epsilon)}{\mu_{trans}}. \tag{5.20}$$

This allows us to find the baryonic mass of hybrid stars. In figures 5.26 - 5.28 the baryonic mass M_B (red) is compared to the gravitational mass M_G (black) for three different equations of state. A trend for all three figures is that M_B and M_G are nearly perfectly parallel, with the exception of particularly high central pressure stars. This means that accretion is only a suitable production scenario for hybrid stars that are more massive than their hadronic counterparts. In figure 5.26 a category II phase transition is shown. Definitionally, category II phase transition feature smaller masses in the hybrid branch than at the hadronic maximum. It is particularly disappointing that this category cannot be produced by accretion, since we noted in subsection 5.3.2 that this category populates an area in the mass radius diagram that can only be achieved

5 A special thanks goes to Giuseppe Pagliara and Alessandro Drago who pointed out the necessity of this consideration and helped with some caveats.

with a phase transition. However, category II is the only category where the hadronic maximum is always more massive than the hybrid branches maximum. In a category III phase transition, for example, accretion would be a plausible production scenario, as is showcased in figure 5.27. Here the baryonic mass clearly is much larger in the hybrid branch than in the hadronic branch. However, in order to be compatible with NICER data, a category III phase transition requires very small values of $\Delta\epsilon$, which might fall shy of generating a sizable mass or radius gap making them much harder to detect and thus less interesting for our particular purposes. Finally, figure 5.28 shows an example of a category I phase transition. The hybrid branch has similar masses to the hadronic branch, with just enough increase in mass to allow accretion as a possible creation process. This is interesting because, like category II, an unique area in the mass radius diagram can be populated by category I phase transitions. In particular, radius values smaller than the smallest possible radius for a 2 $M_\odot$ star with a continuous mass radius relation [Pang et al., 2021, Annala et al., 2022, Huth et al., 2022] predicted to be about 11 km, as noted in section 5.3.2.

This makes it clear that apart from category II phase transitions, accretion cannot be ruled out as a production scenario for hybrid stars. Regardless, there are other possible, less intuitive production scenarios that might apply to category II cases as well. It is beyond the scope of this work to go into greater detail about these production scenarios. The underlying idea behind most scenarios is the existence of a barrier that depending on initial conditions separates neutron and hybrid stars. The main causes proposed for such a barrier are:

- A barrier in the thermal evolution directly after the core collapse supernova [Sagert et al., 2009, Fischer et al., 2011, Hempel et al., 2016, Fischer et al., 2018]. This barrier could be overcome through the process of bubble nucleation [Berezhiani et al., 2003, Bombaci et al., 2004, Bombaci et al., 2007, Bombaci et al., 2008, Bombaci et al., 2009, Mintz et al., 2010, Bombaci et al., 2016, Bhattacharyya et al., 2017].
- The rotation of the protoneutron star could determine if it becomes hadronic or a hybrid star. Fast rotating stars would not allow for hybrid stars [Bhattacharyya et al., 2005, Pili et al., 2016, Bejger et al., 2017], whereas slower rotating stars might.
- The strength of the magnetic field [Gomes et al., 2019] could influence whether or not a protoneutron star becomes a hybrid or hadronic star.

- Hybrid stars might be produced in neutron star mergers [Most et al., 2019, Bauswein et al., 2019, Weih et al., 2020].

5.4.2. Alternative Explanations for Potential Data

In this subsection, we will shortly highlight an alternative to hybrid stars. We noted earlier that there is some area in the mass radius diagram that can only be populated by hybrid stars, if all other astrophysical constraints are to be satisfied. This is, however, not entirely correct. An extremely soft hadronic equation of state could satisfy the GW170817 constraints, as well as populate the area described as "unique" to our category II cases. However, to do so it would need to be so soft that it could not satisfy the 2 $M_\odot$ constraint. The constraints posed by a stiff equation of state would have to be fulfilled by a second equation of state that coexists to the soft hadronic one. This equation of state could of course not be hadronic itself. Instead, it would be a quark matter equation of state that describes pure quark stars. Since the GW170817 constraint is fulfilled by the hadronic EoS, the quark matter EoS is less constricted by the usually high values of Λ found for quark stars. These two families of compact stars would dissolve the tension between the astrophysical constraints demanding a soft EoS and those pointing towards a stiff EoS. This is a short summary of the model that is referred to as the "two family" scenario introduced by Drago et al. [Drago et al., 2016, Drago and Pagliara, 2016, Drago and Pagliara, 2018]. The indicators for this two family scenario are very similar to the twin star configurations explored in this work, especially for category II phase transitions. In fact, if one were to only consider twin star mass radius relations with a sizable mass gap, implying only category I and II fit the data (compare subsection 5.3.2), there would only be a clear difference between the two scenarios at about 2 $M_\odot$, where category I reaches small radii at high masses that cannot be reached by a hadronic EoS. Another important note is that the two family scenario can be achieved through accretion and neutron star mergers, where a hadronic star would be conversed to a quark star.

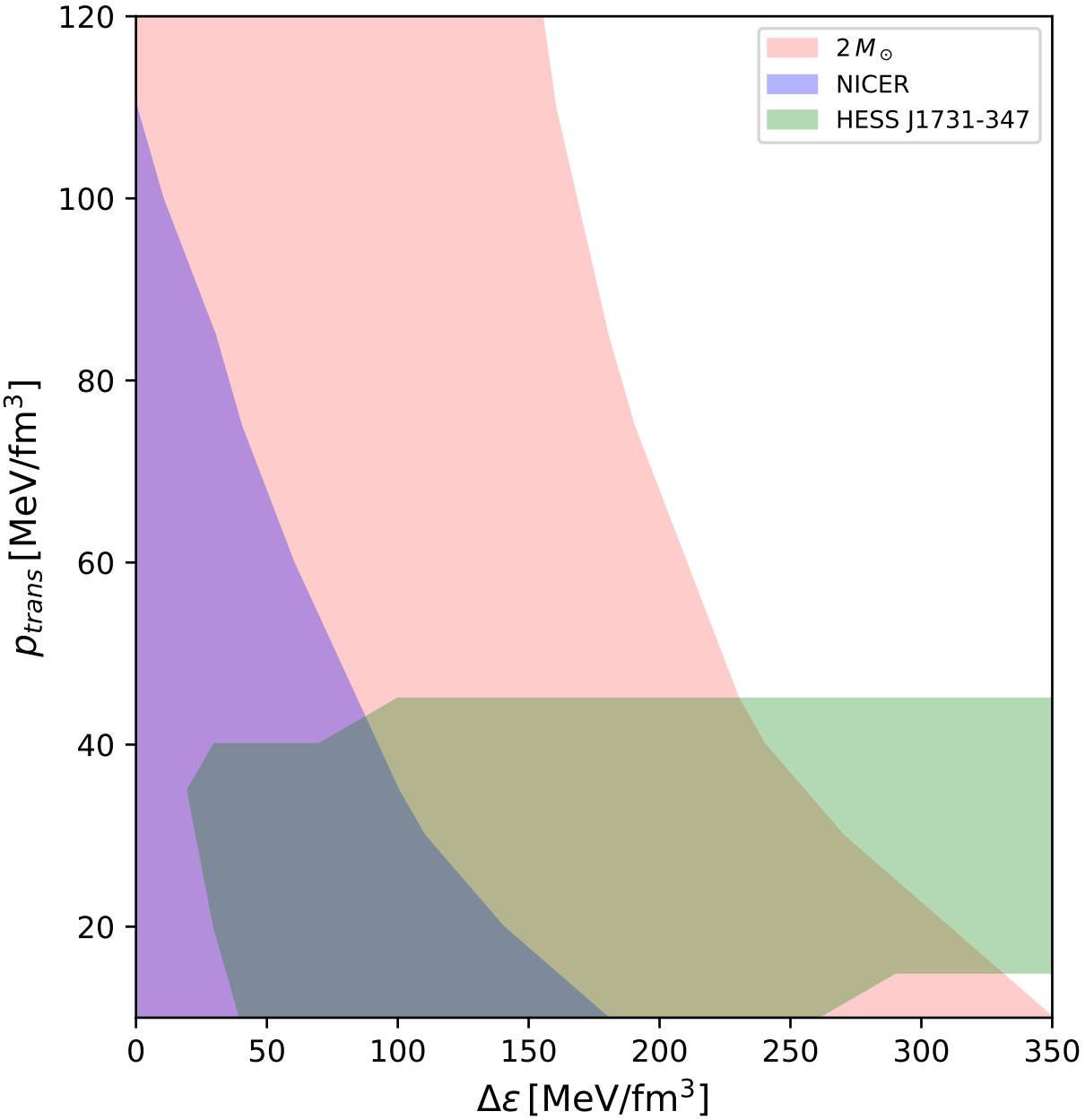

Figure 5.29.: Here the areas in the parameter space are shown that satisfy the $2\,M_\odot$ constraint (red), the new HESS constraint (green) and the previously discussed NICER constraint (blue) respectively. There is a small overlapping section starting at about $\Delta\epsilon \simeq 30\,\mathrm{MeV/fm^3}$, extending to about $\Delta\epsilon \simeq 180\,\mathrm{MeV/fm^3}$ at very small transitional pressures. This implies only category IV type hybrid stars are possible with these constraints.

5.4.3. Influence of HESS J1731-347 on Hybrid stars

During the writing of this work a surprisingly light neutron star mass was reported, HESS J1731-347 [Doroshenko et al., 2022]. Its mass was reported to be $M = 0.77^{+0.20}_{-0.17}\,M_\odot$, which is significantly below estimates from core collapse supernovae simulation [Ozel et al., 2012, Ozel and Freire, 2016, Müller et al., 2019, Suwa et al., 2018], making a discovery of significant interest. However, since the minimal mass of neutron stars has no significant influence on the behavior of hybrid or twin stars, it is not a high priority in this work. In addition to the mass, a radius of $10.4^{+0.86}_{-0.78}$ km estimate was reported. This would be of much more consequence regarding our considerations, as such a small radius would put significant constraints on the hadronic equation of state. However, this estimate is highly optimistic and a more realistic estimate given by Doroshenko et al. [Doroshenko et al., 2022] is noticeably less restrictive with an uncertainty of more than 4 km in the 2σ interval. If different atmosphere models are used, the radius changes significantly as well.
Nevertheless, the surprisingly light star that cannot be generated by conventional means is intriguing and despite the report being very recent some works have been produced to investigate its implications [Tsaloukidis et al., 2022, Di Clemente et al., 2022, Jiang et al., 2022]. Notably, the involvement of exotic matter has been suggested as the cause for this strange behavior, either in the form of quark stars [Di Clemente et al., 2022] or hybrid stars [Tsaloukidis et al., 2022]. However, both cases are made utilizing the surprisingly small radius as well as the small mass.
If one were to apply the stated radius constraint of $10.4^{+0.86}_{-0.78}$ km not even the softest hadronic equation of state still reaching $2\,M_\odot$, which was constructed by Kurkela et al. [Kurkela et al., 2014] would reach radii low enough in the required mass range. This EoS1 reaches radii of about 11.4 km in the mass range of HESS J1731-347 and is therefore off by about 200 m. If we now employ this softest possible hadronic equation of state and include a phase transition, we can move the mass radius relation containing hybrids to smaller radii and therefore meet the radius constraint. However, this requires an early phase transition limiting us to category IV scenarios as well as small values in $\Delta\epsilon$, because if the jump in energy density becomes too large the NICER constraint will not be met. In figure 5.29 the parameter space is plotted and the areas complying with the NICER (blue) [Raaijmakers et al., 2021, Miller et al., 2021, Riley et al., 2021], HESS (green) [Doroshenko et al., 2022] and the $2\,M_\odot$ (red) constraint are shaded. While the HESS constraint can be met by any phase transition with a transitional pressure

that generates a hadronic maximum below the mass of HESS J1731-347 and a jump of $\Delta\epsilon \gtrsim 30\,\mathrm{MeV/fm^3}$, the NICER criterion is much more restrictive. It sets an upper limit of about $\Delta\epsilon \simeq 180\,\mathrm{MeV/fm^3}$, where the maximal transition pressure a $\Delta\epsilon$ can be combined with, decreases with an increase in the discontinuity. On one hand this HESS data would imply that a phase transition is necessary to achieve the mass radius constraint, on the other hand it would make the appearance of twin stars impossible, relegating the possibility of finding a mass radius indicator for a phase transition to cases like itself, where measurements deviate from the expectation.
If one were to ignore the radius constraint from HESS J1731-347 and only apply the mass constraint, the equation of state could not be improved upon using the methods discussed in this work.
Another interpretation of the HESS data point could be dark matter. We will discuss this possibility in an upcoming work with Nibras Suleman, Sarah L. Pitz, Laura Tolos and Jürgen Schaffner-Bielich as well as touch upon it in a collaboration with the group of Laura Sagunski.

5.4.4. Parameter Space for Increased Slope Parameter L

Previously we constrained the slope parameter L to values of about $L = 40 - 60\,\mathrm{MeV}$. This ensured compatibility with χ_{EFT} results and is in line with multiple experiments, most recently the CREX neutron skin experiments for ^{48}Ca [Adhikari et al., 2022, Zhang and Chen, 2022, Lattimer, 2023] from Jefferson Lab. However, the PREX collaboration, which investigated ^{208}Pb estimates much larger values of $L = 121 \pm 47\,\mathrm{MeV}$ [Adhikari et al., 2021, Zhang and Chen, 2022, Lattimer, 2023]. This is disfavored by astrophysical constraints, as we discussed in section 4.4, mostly because increased values of L move the mass radius relation to larger radii causing the EoS to be incompatible with the tidal deformability constraint from GW170817 [Abbott et al., 2019]. Even if the relativistic mean field equation of state undergoes a softening at moderate densities by including a non-zero ζ term, a value of $L = 90\,\mathrm{MeV}$ cannot generate stars with the required compactness, as can be seen on the right side of figure 4.1. However, as discussed in chapter 5, a phase transition could create a hybrid star branch that is located at significantly lower radii than the hadronic branch, making the EoS compatible with GW170817 (see subsection 5.3.3 in particular). Using the equations of state featuring $L = 90\,\mathrm{MeV}$ provided by Farruhk Fattoyev [Fattoyev, 2022], which are fitted to finite nuclei, we can

calculate all possible phase transitions and apply the astrophysical constraints discussed before. The phase transition is applied like in chapter 5. The results are summarized as figures 5.30 - 5.33, where only m^*/m and ζ are varied. On the left side of these figures, the absolute values of p_{trans} and $\Delta\epsilon$ are displayed and the areas in which a constraint is met is shaded accordingly. On the right side, the relative values are shown, where p_{trans} and $\Delta\epsilon$ are divided by ϵ_{trans}. Due to the location of the purely hadronic mass radius relation at large radii, the strongest constraint on the equation of state by far is the tidal deformability. It is indicated by a dark green shade in figures 5.30 - 5.33. In contrast, the NICER constraint [Miller et al., 2021, Riley et al., 2021, Raaijmakers et al., 2021] and the $2\,M_\odot$ constraint [Demorest et al., 2010, Antoniadis et al., 2013, Fonseca et al., 2016, Cromartie et al., 2019, Romani et al., 2022, Doroshenko et al., 2022] are fulfilled easily and barely constrain the EoS. The areas corresponding to these constraints are shaded red and light green, resulting in a brown color where they coincide, which is nearly everywhere.
The stiffest EoS is the one in figure 5.30, consequentially it has the smallest parameter space compatible with GW170817 but reaches $2\,M_\odot$ the easiest. The parameters for this EoS are $m^*/m = 0.55$ and $\zeta = 0.00$. If we increase ζ to $\zeta = 0.02$ (figure 5.31) the parameter space compatible with GW170817 increases, but fewer combinations of p_{trans} and $\Delta\epsilon$ reach $2\,M_\odot$. The same behavior can be seen for the $m^*/m = 0.60$ cases in figures 5.32 and 5.33. However, since the equation of state becomes slightly softer with the increase of the effective mass, the differences are even more pronounced.
All figures also include a small blue shaded area that represents the HESS constraint discussed in the previous subsection. It is possible to match the HESS data in all cases, but the corresponding parameter space is exceedingly small. Finally, the area that generates twin stars is shaded black. Like Alford et al. [Alford et al., 2013] we find this twin star area is very similar for every hadronic EoS. Note that the appearance of twin stars is not a constraint on the equation of state itself, but can be used as an indicator for the presence of a phase transition using mass and radius observation.

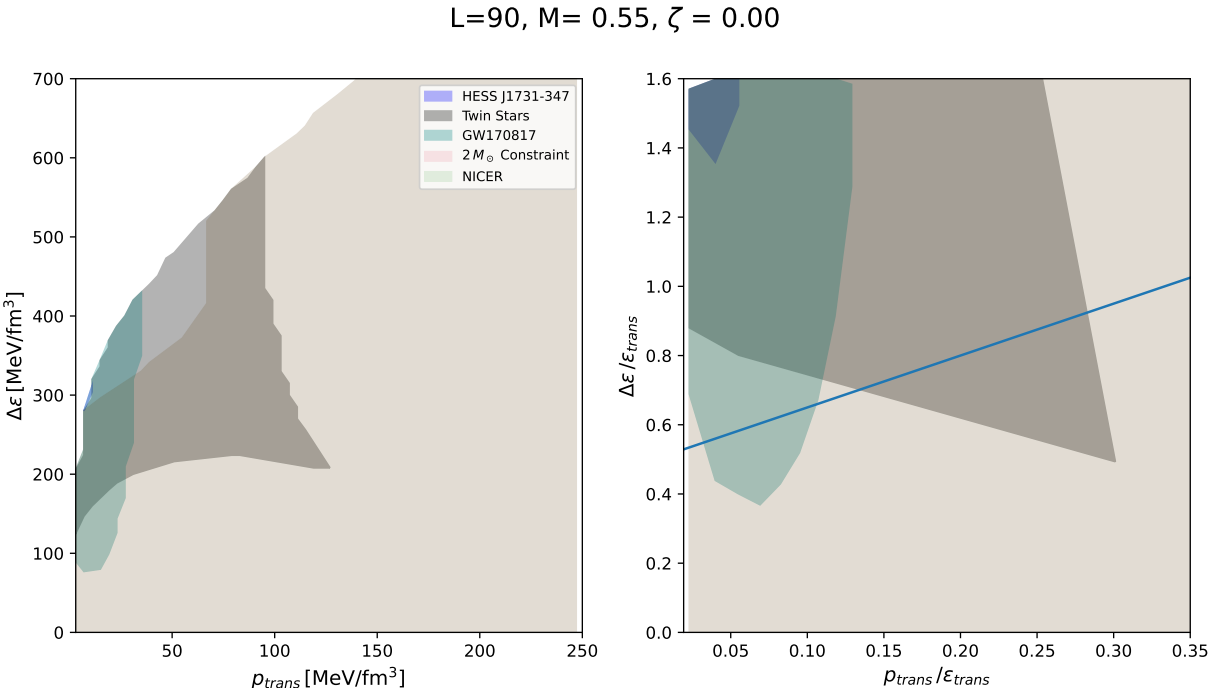

Figure 5.30.: Parameter space for an RMF EoS with $L = 90\,\mathrm{MeV}$, $m^*/m = 0.55$ and $\zeta = 0.00$ provided by Farruhk Fattoyev [Fattoyev, 2022].

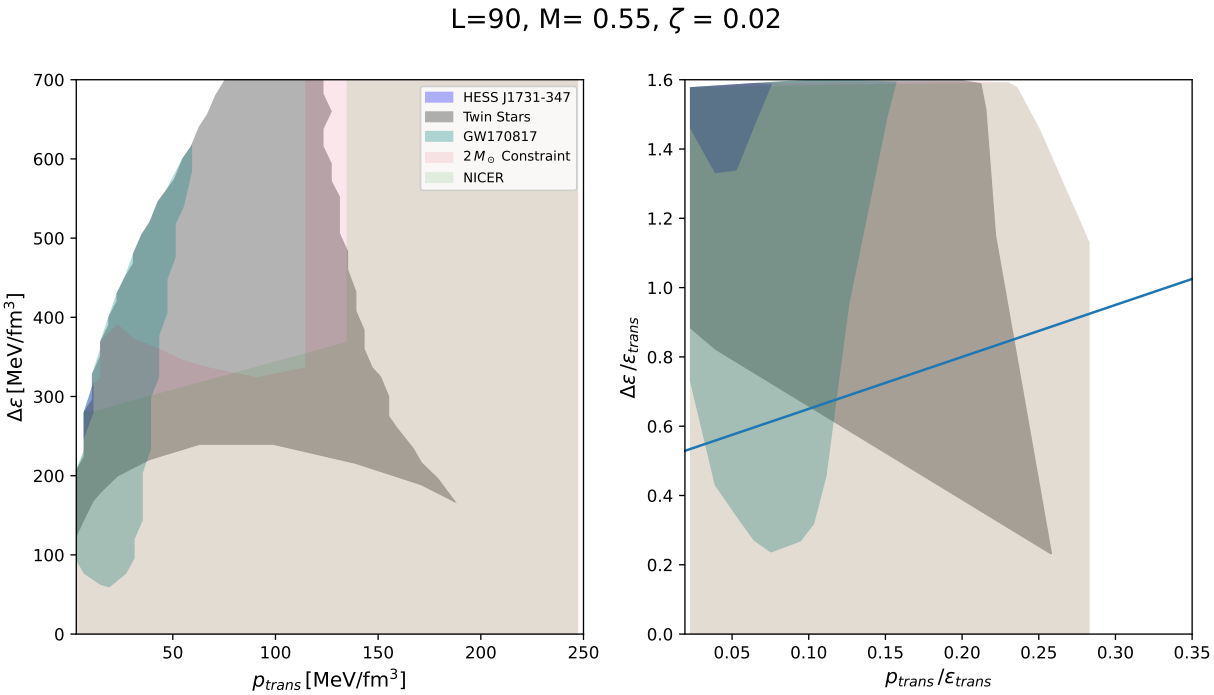

Figure 5.31.: Parameter space for an RMF EoS with $L = 90\,\mathrm{MeV}$, $m^*/m = 0.55$ and $\zeta = 0.02$ provided by Farruhk Fattoyev [Fattoyev, 2022].

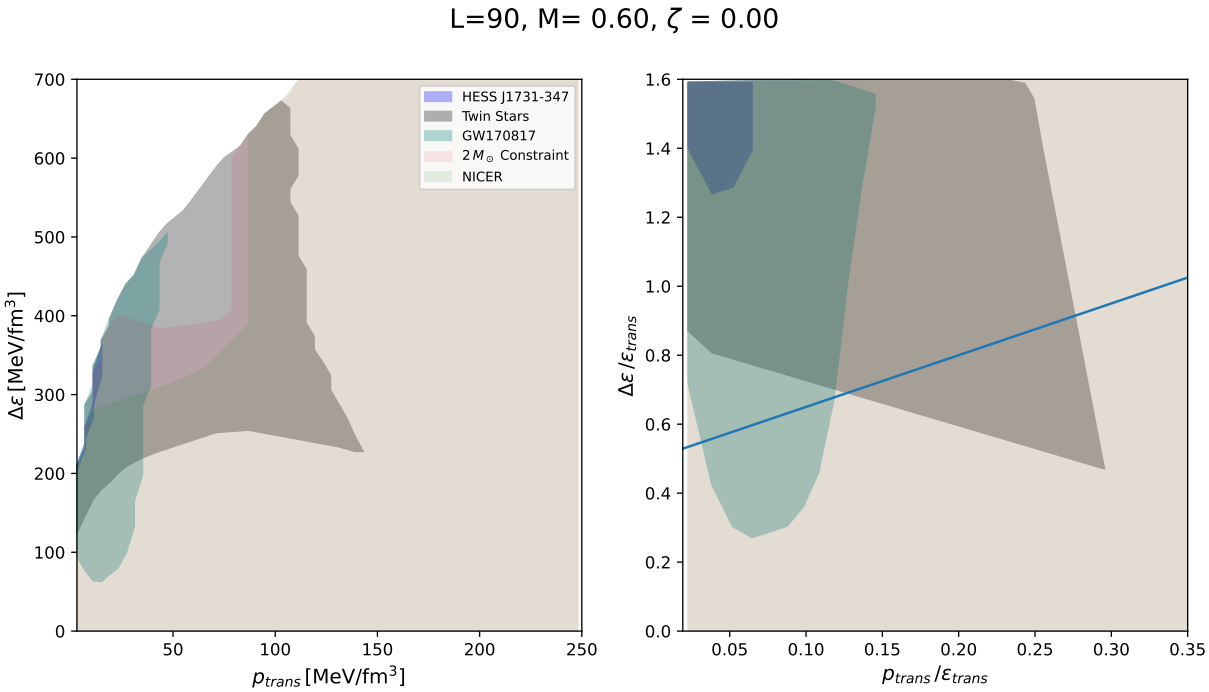

Figure 5.32.: Parameter space for an RMF EoS with $L = 90\,\mathrm{MeV}$, $m^*/m = 0.60$ and $\zeta = 0.00$ provided by Farruhk Fattoyev [Fattoyev, 2022].

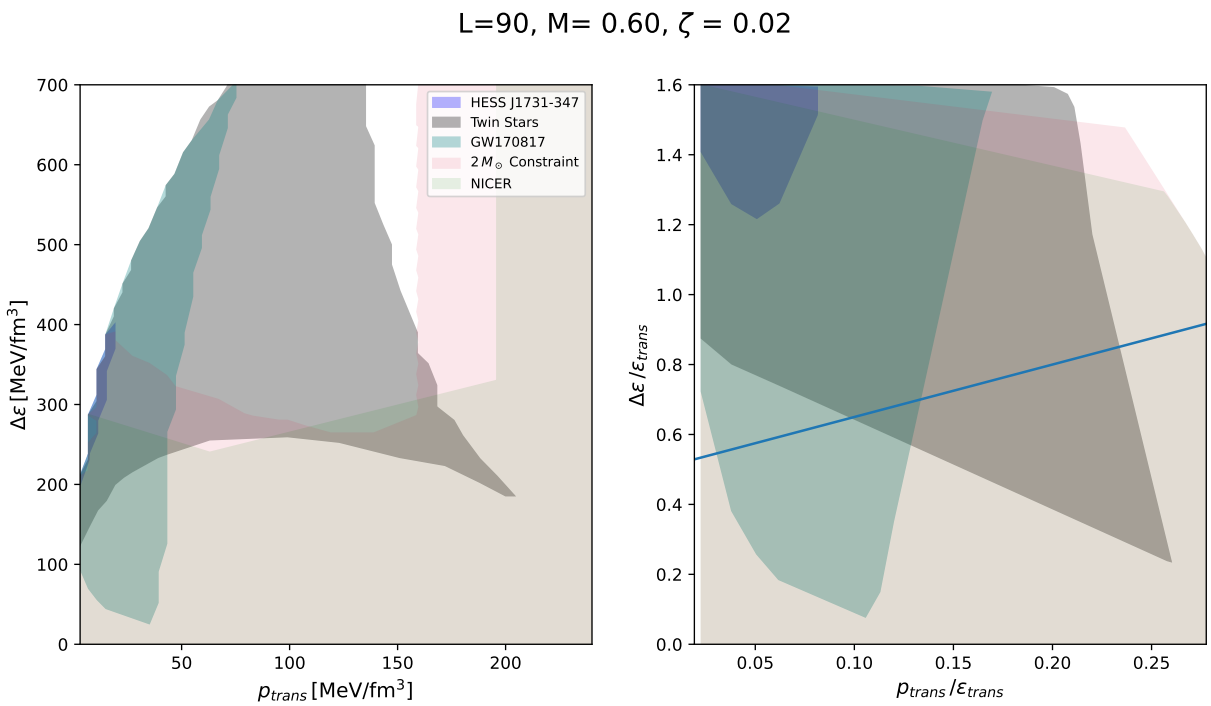

Figure 5.33.: Parameter space for an RMF EoS with $L = 90\,\mathrm{MeV}$, $m^*/m = 0.60$ and $\zeta = 0.02$ provided by Farruhk Fattoyev [Fattoyev, 2022].

6. Conclusion

In this work, we examined the influence of a first order phase transition on the observable properties of neutron stars. This is done with a setup that allows as much flexibility as possible, within a physically motivated framework. As a result, we can make generalized statements about phase transition in neutron stars with some level of independence from the specific model. We started by introducing a relativistic mean field approach that we use to describe the hadronic part of the neutron stars. The purpose of using this particular equation of state is to allow for a large amount of variability. We assume that the matter in a neutron star is only composed of neutrons, protons, electron and muons. The equation of state is constructed in a way where the coupling parameters are fitted to bulk matter properties, leaving some parameters to be freely chosen within certain constraints. Most notably these parameters are the symmetry energy at saturation density $J = 30 - 32\,\mathrm{MeV}$, its slope $L = 40 - 60\,\mathrm{MeV}$ and the effective mass at saturation density $m^*/m = 0.55 - 0.75$ [Li and Han, 2013, Lattimer and Lim, 2013, Roca-Maza et al., 2015, Hagen et al., 2015, Oertel et al., 2017, Birkhan et al., 2017]. We varied these three parameters and found that only some parameter sets are compatible with chiral effective field theory predictions for nuclear matter [Drischler et al., 2016, Hornick et al., 2018]. We noted that small effective masses and small values of L are particularly difficult to combine. Of the three varied parameters, the effective mass has the largest influence on the high density behavior of the equation of state, where it governs the stiffness of the EoS. Here, small effective masses lead to stiffer equations of state [Boguta and Stöcker, 1983]. The other two parameters were therefore fixed in a way that allows the greatest variation of m^*/m still compatible with χ_{EFT}. This means setting $J = 32\,\mathrm{MeV}$ and $L = 60\,\mathrm{MeV}$. We then expanded the equation of state to finite temperatures for future use. The thermal index was shown to be related to the effective mass, where high values of m^*/m leads to high values in the thermal index at intermediate densities. As one would expect, the high density behavior tends to $4/3$. After we established the equation of state, we used it to calculate the mass, radius and

tidal deformability of neutron stars that would be described by it. These quantities are known for some neutron stars, allowing us to constrain our equation of state at high densities. The mass constraint of about 2 $M_\odot$ [Demorest et al., 2010, Antoniadis et al., 2013, Fonseca et al., 2016, Cromartie et al., 2019, Romani et al., 2022, Doroshenko et al., 2022] slightly favors stiff equations of state, which puts pressure on the highest effective mass equation of state under investigation. Contrary to this, the gravitational wave event GW170817 provides a tidal deformability estimate that favors soft equations of state excluding effective masses of $m^*/m < 0.65$. The radius cannot be used to solve this tension, as it is not known to a degree sufficient enough to exclude any of the effective masses. We therefore constrained effective masses for pure neutron stars in our model to $m^*/m = 0.65 - 0.70$.

This constraint was somewhat weakened by the introduction of a first order phase transition to deconfined quark matter [Christian and Schaffner-Bielich, 2020]. We constructed this phase transition as a jump in the energy density $\Delta\epsilon$ at a critical pressure p_{trans} and employed a constant speed of sound approach to describe the quark phase. Again, this gives us three parameters to consider, the discontinuity $\Delta\epsilon$, the transitional pressure p_{trans} and the speed of sound c_{QM}. We set the speed of sound to $c_{QM} = 1$ giving us the stiffest possible case and thus the greatest possible parameter space for the other two parameters. With this construction, mass, radius and tidal deformability can be calculated for hybrid stars, which are stars composed partially from quark and hadronic matter. Some indicators for the presence of a phase transition in neutron stars were outlined, including so-called twin stars, where two stars with the same mass, but different radii are observed. We went on to define four distinct categories of twin stars, as was done in [Christian et al., 2018], which makes it far easier to discuss this topic. A particular advantage of this categorization is its applicability to any twin star configuration, not only our model. It is reasonable to assume that stars with the same mass, but different radii would also lead to two stars with the same mass but different tidal deformabilities. We find that hybrid stars are much more compact than purely hadronic stars. Applying the same astrophysical constraints as we did for neutron stars this became particularly important, as the stiff equations of state ruled out by GW170817 gained access to much more compact hybrid stars, making them compatible with the tidal deformability constraint. However, this requires that the phase transition takes place at small central densities [Christian and Schaffner-Bielich, 2020]. Unlike for the purely hadronic stars, the radius constraints from NICER effect the parameter space noticeably. We found that the NICER constraints require small jumps in energy density

if the phase transition takes place at small central densities. This is because $\Delta\epsilon$ effects the position of the hybrid stars in the mass radius diagram, where small $\Delta\epsilon$ lead to larger radii. Small jumps in energy density imply that the mass and radius differences between hadronic and hybrid stars are small, making them hard to detect and unsuitable as possible indicators for a phase transition. The mass constraint points towards small values of $\Delta\epsilon$ as well, if the phase transition happens early. This is because small $\Delta\epsilon$ increase the mass of the hybrid star maximum, which for early phase transitions is always more massive than the hadronic maximum.
However, the NICER constraints do not rule out larger $\Delta\epsilon$ entirely, but restrict them to high values of p_{trans}, where the constraints can be met by the hadronic mantle. In such a case, all hybrid stars would have a similar mass determined by $\Delta\epsilon$.

To summarize: Using a versatile equation of state, we conducted a parameter study on hybrid stars using most current astrophysical constraints. We find that phase transitions in neutron stars are not required to fit the data but are not excluded either. The parameter space that allows for hybrid stars seems to be pushed to its edges, where some measurements like NICER [Miller et al., 2019, Riley et al., 2019, Raaijmakers et al., 2019, Miller et al., 2021, Riley et al., 2021, Raaijmakers et al., 2021] favor high transitional pressures [Christian et al., 2019, Christian and Schaffner-Bielich, 2022] and others like GW170817 [Abbott et al., 2017, Abbott et al., 2019] and the new HESS J1731-347 [Doroshenko et al., 2022] measurement point towards extremely small values of p_{trans} [Christian and Schaffner-Bielich, 2020, Christian and Schaffner-Bielich, 2021]. We provide an overview over some methods with which the existence of a phase transition could be verified in the near future. Due to the generalized approach taken, these results should hold for different models as well.

7. Outlook

Finally, we take a moment to look into the future. Our equation of state is matched to describe high density matter constraints, while still providing a large amount of parameterizability, making it well suited to investigate extremely soft and extremely stiff cases in a consistent framework. Within this framework, we can already complete multiple new projects. Like mentioned in subsection 5.4.3 a closer look at the HESS J1731-347 [Doroshenko et al., 2022] data point and is in order, as it is nearly impossible to reconcile with a purely hadronic equation of state. The possible influences of quark matter on the compatibility with HESS will be compared to possible influences from dark matter with the framework presented here as a basis for the quark matter description in an upcoming work. The hadronic equation of state described here will be used to research the interplay between a hadronic equation of state and dark matter in an upcoming project. This will be done in collaboration with the group of Laura Sagunski under the B09 project of the CRC TR 211, which would eventually open up the possibility to use the resulting matter description for merger simulations. Mass, radius and tidal deformability provide the best determined constraints on the equation of state. However, another helpful observable might be the luminosity of neutron stars. Starting from their previous work, we collaborate with Melissa Mendes et al. [Mendes et al., 2022] to investigate the effect a quark core would have on the cooling behavior of a hybrid star. It might, for example, be possible to determine the presence of a phase transition by comparing two stars with similar masses that show different cooling behavior.

While determining the existence of a phase transition took precedence in this work, the specificities of the phase transition itself will require more work in the future. There is a multitude of more sophisticated quark matter descriptions that could be implemented into the framework presented here, if the presence of a phase transition in neutron stars is more certain. Even our very simplistic model offers more potential for investigation. One could for example assume that the energy density at the point

of transition drops, instead of jumping up and investigate the thermal consistency of such a construction along with the mass radius implications. With the expansion of the EoS to finite temperatures and the possibility to set a specific proton fraction, it is easy to adjust the equation of state to be used for various purposes, such as core collapse supernova simulations as well as binary neutron star mergers and protoneutron stars. The greatest challenge in making the EoS used here suitable for such purposes would be the crust equation of state, that cannot be used at non-zero temperatures. However, there are already solutions for similar equations of state that could be used if a more involved approach is too time sensitive. A more in depth investigation of the thermal behavior of the hadronic EoS described here is the logical next step. This could include determining if the behavior of Γ_{th} in β equilibrium being smaller than for fixed Y_p EoSs is universal or not. Once this step is taken and the aforementioned simulations become achievable the possibility opens up to investigate production scenarios for hybrid stars in much greater detail, as was alluded to in subsection 5.4.1, where a barrier in the thermal evolution that separates hybrid and non-hybrid stars was suggested.
Possible further steps could be the inclusion of more exotic particles in addition to the neutrons, protons, electrons and muons, like for example hyperons. Another interesting avenue might be the inclusion of the ω mesons quadratic self coupling ζ in order to compare the possible methods of controlling the EoSs stiffness more thoroughly.
Apart from the projects described above, there are great strides expected in the field of gravitational wave observations. Later this year, LIGO/Virgo will start its fourth observational run [LIGO Collaboration, 2023], with much increased sensitivity, which should enable the detection of more neutron star mergers similar to the highly influential GW170817 event. The future of constraining the (hybrid star) equation of state is in gravitational wave data. Not only is it likely that the sizable differences in tidal deformabilities between hybrids and non hybrids are detectable [Landry and Chakravarti, 2022] in gravitational wave events, there might even be some signals for a phase transition in the post merger frequency [Most et al., 2019, Bauswein et al., 2019, Tootle et al., 2022] itself that can be detected with next generation observatories [Maggiore et al., 2020, Evans et al., 2021].

8. Zusammenfassung

In dieser Arbeit wurde der Einfluss eines Phasenübergangs erster Ordnung auf die beobachtbaren Eigenschaften von Neutronensternen untersucht. Weiterhin wurde die verwendete Zustandsgleichung auf endliche Temperaturen erweitert. Hierbei lag ein besonderer Fokus darauf, unsere Ergebnisse so universell anwendbar wie möglich zu halten, was wir mit einem generischen Ansatz gewährleisten. In Kapitel 3 begannen wir mit der Einführung eines relativistischen Mean Feld (RMF) Ansatzes, den wir zur Beschreibung des hadronischen Teils der Neutronensterne verwenden. Hierbei handelt es sich um eine effektive Zustandsgleichung, bei der die Interaktion der Nukleonen durch Mesonen modelliert wird. Ihr Name kommt daher, dass bei hoher Baryonendichte die Mittelwerte der entsprechenden Felder im Lagrangian verwendet werden können, was die Rechnung erheblich vereinfacht. Weiterhin ist der RMF Ansatz stark parametrisierbar, wodurch eine große Variabilität gewährleistet werden kann und dennoch ein physikalisch motiviertes Modell verwendet wird. Wir nehmen an, dass die Materie in einem Neutronenstern nur aus Neutronen, Protonen, Elektronen und Myonen besteht. Die Zustandsgleichung ist so konstruiert, dass die Kopplungskonstanten durch Kernmaterieeigenschaften vorgegeben werden können, indem einige Parameter innerhalb bestimmter Grenzen gewählt werden. Für unsere Zwecke sind die wichtigsten dieser Parameter die Symmetrieenergie $J = 30 - 32\,\mathrm{MeV}$, ihre Steigung $L = 40 - 60\,\mathrm{MeV}$ und die effektive Masse $m^*/m = 0.55 - 0.75$ bei Sättigungsdichte n_0 [Li and Han, 2013, Lattimer and Lim, 2013, Roca-Maza et al., 2015, Hagen et al., 2015, Oertel et al., 2017, Birkhan et al., 2017]. Beim Variieren dieser drei Parameter stellten wir fest, dass nur einige Parametersätze mit den Vorhersagen der chiralen effektiven Feldtheorie (χ_{EFT}) [Drischler et al., 2016, Hornick et al., 2018] kompatibel sind. Diese Theorie stellt einen ab initio Ansatz zur Beschreibung von Neutronenmaterie bei geringen Energien basierend auf dem Brechen der chiralen Symmetrie von Up- und Down-Quarks im QCD Lagrangian zur Verfügung. Wir stellten fest, dass kleine effektive Massen und kleine Werte von L besonders schwierig zu kombinieren sind. Das

liegt daran, dass geringe effektive Massen für eine steilere Zustandsgleichung sorgen, während kleinere L zu einer weicheren Zustandsgleichung führen. Die Konkurrenz dieser Effekte führt zu unphysikalischen Lösungen. Bei hohen Dichten hat die effektive Masse den größten Einfluss auf das Verhalten der Zustandsgleichung unter den drei variierten Parametern. Sie bestimmt, wie schnell der Druck mit der Energiedichte steigt, also die sogenannte Steilheit der Zustandsgleichung. Kleine effektive Massen führen zu steileren Zustandsgleichungen [Boguta and Stöcker, 1983]. Da diese Arbeit sich vor allem mit astrophysikalischen Einschränkungen beschäftigt, die bei hohen Dichten auftreten, wählten wir die beiden anderen Parameter so, dass die größte Variation von m^*/m gegeben ist, die noch mit χ_{EFT} vereinbar ist. Auf dieser Überlegung basierend wählten wir $J = 32\,\mathrm{MeV}$ und $L = 60\,\mathrm{MeV}$. Auf diese Weise konnten wir sowohl sehr weiche als auch sehr steile Zustandsgleichungen mit einem konsistenten Ansatz untersuchen. Anschließend wurde die Zustandsgleichung für zukünftige Verwendungen auf endliche Temperaturen erweitert. Hierbei wurde gezeigt, dass der thermische Index Γ_{th}, der im Fall des idealen Gases mit dem adiabatischen Index identifiziert werden kann, mit der effektiven Masse zusammenhängt, wobei hohe Werte von m^*/m zu hohen Werten des thermischen Indexes bei mittleren Dichten führen. Wie zu erwarten, nähert sich Γ_{th} bei hoher Dichte an den ultra-relativistischen Fall des adiabatischen Indexes, $4/3$, an. Weiterhin stellten wir fest, dass der thermische Index im β Gleichgewicht geringere Werte aufweist als für festgelegte Protonenanteile. Obwohl geringere festgelegte Protonenanteile zu höheren Werten des thermischen Index führen, ist dies trotzdem der Fall, wenn der Protonenanteil im β Gleichgewicht deutlich unter den festgelegten Werten liegt.

Nachdem wir uns mit der Zustandsgleichung intensiv beschäftigt haben und Werte für Symmetrieenergie und Steigungsparameter gewählt haben, konnten wir in Kapitel 4 die Zustandsgleichung verwenden, um die Masse, den Radius und die gezeitliche Verformbarkeit von Neutronensternen damit zu berechnen. Diese Größen sind durch aktuelle Messinstrumente ermittelbar und für einige Neutronensterne bekannt, was wir nutzen können, um unsere Zustandsgleichung bei hohen Dichten einzuschränken. Die maximale Neutronensternmasse von etwa $2\,M_\odot$ [Demorest et al., 2010, Antoniadis et al., 2013, Fonseca et al., 2016, Cromartie et al., 2019, Romani et al., 2022, Doroshenko et al., 2022] muss durch eine Zustandsgleichung reproduzierbar sein. Dadurch sind steilere Zustandsgleichungen leicht begünstigt, die zu massereicheren, aber auch weniger kompakten Neutronensternen führen. Dieser Umstand bringt die Zustandsgleichung mit den größten effektiven Massen in Bedrängnis. Im Gegensatz dazu liefert das Gravita-

tionswellenereignis GW170817 [Abbott et al., 2017] eine Abschätzung der gezeitlichen Verformbarkeit, die weiche Zustandsgleichungen begünstigt, die kompaktere Sterne generieren. Dadurch konnten effektive Massen von $m^*/m < 0,65$ ausgeschlossen werden. Bedauerlicherweise kann der Radius nicht verwendet werden, um diese Spannung zu lösen, da es bisher nicht möglich ist ihn ausreichend genau zu bestimmen. Mit der Einschränkung durch die Masse und die gezeitliche Verformbarkeit konnten wir die effektiven Massen für reine Neutronensterne in unserem Modell auf $m^*/m = 0,65 - 0,70$ beschränken.
Allerdings ist es möglich diese Einschränkung durch die Einführung eines Phasenübergangs erster Ordnung zu einem Quark-Gluon Plasma etwas abzuschwächen, wie in Kapitel 5 gezeigt wird. Dieser Phasenübergang wurde durch eine Maxwell Konstruktion in unser Modell eingefügt, wobei bei einem kritischen Druck von p_{trans} die Energiedichte eine Diskontinuität $\Delta\epsilon$ erfährt. Alle höheren Drücke wurden dann durch eine Quarkphase mit konstanter Schallgeschwindigkeit beschrieben. Das bedeutet es sind drei Parameter zu berücksichtigen: die Unstetigkeit $\Delta\epsilon$, der Übergangsdruck p_{trans} und die Schallgeschwindigkeit c_{QM}. Wir setzten die Schallgeschwindigkeit auf $c_{QM} = 1$, was den steilst möglichen Fall darstellt und damit den größtmöglichen Parameterraum für die beiden anderen Parameter bietet. Mit dieser Konstruktion konnten Masse, Radius und gezeitliche Verformbarkeit für Hybridsterne berechnet werden, die im Kern aus Quarkmaterie und im Mantel aus hadronischer Materie bestehen. Diese Rechnungen ermöglichen es, einige Indikatoren für die Präsenz eines Phasenübergangs zu ermitteln, darunter sogenannte Zwillingssterne, bei denen zwei Sterne mit genau gleicher Masse unterschiedliche Radien aufweisen. Diese Konfiguration ist dann zu finden, wenn die Masse-Radius Beziehung unterbrochen wird und erst nach einer Unstetigkeit in der Masse wieder fortgesetzt wird. Dieses Phänomen tritt auf, da ein kleiner Quarkkern den Neutronenstern destabilisiert, doch bei hohen Zentraldichten und größeren Kernen besteht die Möglichkeit erneut Stabilität zu erlangen. Es ist allerdings darauf hinzuweisen, dass eine große Differenz zwischen diesen Radien bestehen muss, wenn man hofft diesen Indikator mit aktuellen Messmethoden zu verwenden, was nicht immer der Fall ist. Wir haben gezeigt, dass solche Unterschiede in den Radien grundsätzlich möglich sind, aber nur in einem deutlich kleinerem Parameterraum. Diese Zwillingssternkonfiguration würde offensichtlich auch zu zwei Sternen mit gleicher Masse, aber unterschiedlicher gezeitliche Verformbarkeit führen, wobei Hybridsterne viel kompakter sind als rein hadronische Sterne. Als wir die gleichen astrophysikalischen Einschränkungen anwendet haben wie zuvor bei den reinen Neu-

tronensternen, wurde dies besonders wichtig, da die steileren Zustandsgleichungen, die durch GW170817 auszuschließen sind, zu viel kompakteren Hybridsternen führen als ihre puren Neutronensterngegenstücke. Diese kompakteren Sterne können mit GW170817 kompatibel sein. Das setzt jedoch voraus, dass der Phasenübergang bei kleinen zentralen Dichten stattfindet [Christian and Schaffner-Bielich, 2020]. Anders als bei den rein hadronischen Sternen wirkten sich die Radiusbeschränkungen durch NICER [Miller et al., 2019, Riley et al., 2019, Miller et al., 2021, Riley et al., 2021] deutlich auf den Parameterraum aus. So erfordern die NICER-Beschränkungen kleine Sprünge in der Energiedichte, wenn der Phasenübergang bei kleinen zentralen Dichten stattfindet. Das liegt daran, dass $\Delta\epsilon$ die Position der Hybridsterne im Massenradiusdiagramm beeinflusst, wo kleine $\Delta\epsilon$ zu größeren Radien führen. Kleine Sprünge in der Energiedichte bedeuten, dass die Massen- und Radiusunterschiede zwischen hadronischen und hybriden Sternen klein sind, was sie schwer nachweisbar und als mögliche Indikatoren für einen Phasenübergang ungeeignet macht. Das Massenkriterium deutet ebenfalls auf kleine Werte von $\Delta\epsilon$ hin, wenn der Phasenübergang früh stattfindet. Das liegt daran, dass kleine $\Delta\epsilon$ die Masse des Hybridstern-Maximums erhöhen und dieses ist bei frühen Phasenübergängen immer massereicher ist als das hadronische Maximum. Dennoch stellten wir fest, dass die NICER-Einschränkungen große $\Delta\epsilon$ nicht völlig ausschließen, sondern sie lediglich auf hohe Werte von p_{trans} beschränken, bei denen die Einschränkungen bereits durch den hadronischen Mantel erfüllt werden können. In einem solchen Fall haben alle Hybridsterne eine ähnliche Masse, die durch $\Delta\epsilon$ bestimmt wird. Das liegt daran, dass hohe kritische Drücke einen sehr flachen Hybridsternast zur Folge haben. Wie der Parameterbereich eingeschränkt werden kann ist beispielhaft in Abbildung 8.1 skizziert. Auf der linken Seite des Bildes sind die absoluten Werte der Parameter p_{trans} und $\Delta\epsilon$ schattiert, die gewissen Einschränkungen genügen, auf der rechten Seite sind die gleichen Werte um die Energiedichte in der hadronischen Phase an der Stelle des Phasenübergangs normiert. Da in diesem Fall das Kriterium durch GW170817 bereits durch die hadronische Zustandsgleichung bedient ist, wird für diese Einschränkung kein Bereich schattiert. Wo der Parameterraum braun gefärbt ist überschneiden sich NICER (grün schattiert) und die Einschränkung durch die Maximalmasse (rot schattiert). Da noch ein rot schattierter Bereich zu sehen ist, wird deutlich, dass die Radiusangabe von NICER die deutlichste Einschränkung an diese Zustandsgleichung darstellt. Der grau schattierte Bereich steht für Zwillingssterne, wobei Parametersätze gemeint sind, die zwei Sterne mit exakt der gleichen Masse, aber einem unterschiedlichen Radius aufweisen. Dies ist nicht zu verwechseln mit

dem grün gefärbten Bereich, der das Gebiet darstellt, in dem es realistisch möglich ist durch Messungen von Masse und Radius zu überprüfen, ob ein Phasenübergang in Neutronensternen stattfindet. Hier wird davon ausgegangen, dass zwei Sterne vorliegen, deren Masse sich maximal um $0.05\,M_\odot$ unterscheidet, aber deren Radien mindestens 1 km auseinander liegen. Dieses Szenario kann nur mit einem Phasenübergang gewährleistet werden, aber erfordert nicht zwangsläufig, dass die Masse-Radius Beziehung unterbrochen wird. Insbesondere wenn hohe Werte von p_{trans} vorliegen wird der Massezuwachs bei steigenden Zentraldrücken geringer und solche "Pseudozwillinge" können auftreten.

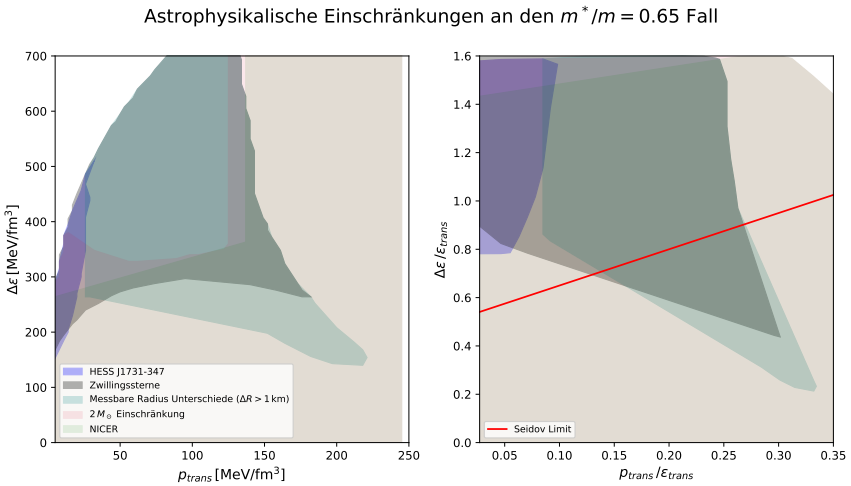

Figure 8.1.: Einschränkungen an den Parameterraum durch astrophysikalische Beobachtungen am Beispiel unserer Zustandsgleichung für eine effektive Masse von $m^*/m = 0.65$.

Zusammenfassend haben wir unter Verwendung einer vielseitigen Zustandsgleichung eine Parameterstudie über Hybridsterne durchgeführt, die alle aktuellen astrophysikalischen Einschränkungen berücksichtigt. Wir stellen fest, dass Phasenübergänge in Neutronensternen nicht zwangsläufig erforderlich sind, um mit den beobachteten Daten überein zu stimmen, aber auch nicht ausgeschlossen werden können. Der Parameterraum, der Hybridsterne zulässt, wird durch Messungen wie NICER [Miller et al., 2019, Riley et al., 2019, Raaijmakers et al., 2019, Miller et al., 2021, Riley et al., 2021, Raaijmakers et al., 2021] auf hohe Übergangsdrücke begrenzt [Christian et al., 2019, Christian and Schaffner-Bielich, 2022], doch andere Ergebnisse wie GW170817 [Abbott et al., 2017, Abbott et al., 2019] und die neue HESS J1731-347 [Doroshenko et al., 2022] Messung deuten auf extrem kleine Werte von p_{trans} [Christian and Schaffner-Bielich, 2020, Chris-

tian and Schaffner-Bielich, 2021] hin. Mithilfe von genaueren Masse-, Radius- und gezeitlichen Verformbarkeitsbestimmungen sollte es in naher Zukunft möglich sein starke Indikatoren wie Zwillingssterne für Phasenübergänge zu finden oder die Präsenz von Phasenübergängen in Neutronensternen auszuschließen.

9. Danksagung

Zu guter Letzt danke ich den Menschen, die mich bei meiner Doktorarbeit unterstützt haben. Zuallererst ist hier selbstverständlich mein Betreuer Prof. Dr. Jürgen Schaffner-Bielich zu nennen, der mich nicht nur dazu ermutigte, die Arbeit überhaupt zu beginnen, sondern auch währenddessen immer ein offenes Ohr und motivierende Worte hatte. Auch mein Zweitgutachter Prof. Dr. Carsten Greiner ist nicht zu vergessen, mit dem ich noch nie ein Gespräch geführt habe, aus dem ich nicht selbstsicherer herausgegangen bin, als ich hineinging. Weiterhin gebührt dem zu früh verstorbenen Dr. Andreas Zacchi ein besonderer Dank; er war immer eine Inspiration.

Eine unbeschreibliche Hilfe waren alle, die meine Doktorarbeit Korrektur gelesen haben, um die vielen Rechtschreibfehler zu beheben, die sonst zweifelsohne zu finden gewesen wären. Hier sind besonders Sarah Sophia Wörner, Prof. Dr. Debarati Chatterjee und Rolf-Jürgen Christian hervorzuheben. Auch möchte ich Sarah Louisa Pitz und Stephan Wystub an dieser Stelle für das Probelesen und einige sehr hilfreiche Kommentare danken.

Besonders danke ich dem Ehepaar Giersch, dir mir mit dem großzügigen Giersch Stipendium die finanzielle Sicherheit gegeben haben, um mich auf meine Doktorarbeit konzentrieren zu können. Schließlich möchte ich meiner Familie danken, die häufig mehr an mich geglaubt hat als ich selbst.

Bibliography

[Abbott et al., 2017] Abbott, B. P., Abbott, R., Abbott, T. D., et al. (2017). GW170817: Observation of Gravitational Waves from a Binary Neutron Star Inspiral. *Phys. Rev. Lett.*, 119(16):161101.

[Abbott et al., 2019] Abbott, B. P., Abbott, R., Abbott, T. D., et al. (2019). Properties of the binary neutron star merger GW170817. *Phys. Rev.*, X9(1):011001.

[Abbott et al., 2018] Abbott, B. P. et al. (2018). GW170817: Measurements of neutron star radii and equation of state. *Phys. Rev. Lett.*, 121(16):161101.

[Abbott et al., 2020] Abbott, R., Abbott, T. D., Abraham, S., Acernese, F., and K. Ackley, e. a. (2020). GW190814: Gravitational waves from the coalescence of a 23 solar mass black hole with a 2.6 solar mass compact object. *The Astrophysical Journal*, 896(2):L44.

[Adhikari et al., 2021] Adhikari, D. et al. (2021). Accurate Determination of the Neutron Skin Thickness of ^{208}Pb through Parity-Violation in Electron Scattering. *Phys. Rev. Lett.*, 126(17):172502.

[Adhikari et al., 2022] Adhikari, D. et al. (2022). Precision Determination of the Neutral Weak Form Factor of Ca48. *Phys. Rev. Lett.*, 129(4):042501.

[Agrawal, 2010] Agrawal, B. (2010). Equations of state and stability of color-superconducting quark matter cores in hybrid stars. *Phys. Rev.*, D81:023009.

[Alcock et al., 1986] Alcock, C., Farhi, E., and Olinto, A. (1986). Strange stars. *Astrophys. J.*, 310:261.

[Alford et al., 2005] Alford, M., Braby, M., Paris, M., and Reddy, S. (2005). Hybrid stars that masquerade as neutron stars. *Astrophys.J.*, 629:969–978.

[Alford et al., 2015] Alford, M. G., Burgio, G., Han, S., Taranto, G., and Zappalà, D. (2015). Constraining and applying a generic high-density equation of state". *Phys. Rev.*, D92(8):083002.

[Alford et al., 2013] Alford, M. G., Han, S., and Prakash, M. (2013). Generic conditions for stable hybrid stars. *Phys. Rev. D*, 88(8):083013.

[Alford et al., 2014] Alford, M. G., Han, S., and Prakash, M. (2014). Generic Conditions for Stable Hybrid Stars. *JPS Conf.Proc.*, 1:013041.

[Alford and Sedrakian, 2017] Alford, M. G. and Sedrakian, A. (2017). Compact stars with sequential QCD phase transitions. *Phys. Rev. Lett.*, 119(16):161104.

[Alvarez-Castillo et al., 2019] Alvarez-Castillo, D. E., Blaschke, D. B., Grunfeld, A. G., and Pagura, V. P. (2019). Third family of compact stars within a nonlocal chiral quark model equation of state. *Phys. Rev.*, D99(6):063010.

[Annala et al., 2022] Annala, E., Gorda, T., Katerini, E., Kurkela, A., Nättilä, J., Paschalidis, V., and Vuorinen, A. (2022). Multimessenger Constraints for Ultradense Matter. *Phys. Rev. X*, 12(1):011058.

[Annala et al., 2018] Annala, E., Gorda, T., Kurkela, A., and Vuorinen, A. (2018). Gravitational-wave constraints on the neutron-star-matter Equation of State. *Phys. Rev. Lett.*, 120(17):172703.

[Antoniadis et al., 2013] Antoniadis, J., Freire, P. C., Wex, N., Tauris, T. M., Lynch, R. S., van Kerkwijk, M. H., Kramer, M., Bassa, C., Dhillon, V. S., Driebe, T., Hessels, J. W. T., Kaspi, V. M., Kondratiev, V. I., Langer, N., Marsh, T. R., McLaughlin, M. A., Pennucci, T. T., Ransom, S. M., Stairs, I. H., van Leeuwen, J., Verbiest, J. P. W., and Whelan, D. G. (2013). A Massive Pulsar in a Compact Relativistic Binary. *Science*, 340:6131.

[Baade and Zwicky, 1934a] Baade, W. and Zwicky, F. (1934a). On super-novae. *Proc. Nat. Acad. Sci. U.S.*, 20:254.

[Baade and Zwicky, 1934b] Baade, W. and Zwicky, F. (1934b). Supernovae and cosmic rays. *Phys. Rev.*, 45:138.

[Bardeen et al., 1966] Bardeen, J., Thorne, K. S., and Meltzer, D. W. (1966). A catalogue of methods for studying the normal modes of radial pulsation of general-relativistic stellar models. *Astrophysical Journal*, 145:505.

[Bauswein et al., 2019] Bauswein, A., Bastian, N.-U. F., Blaschke, D. B., Chatziioannou, K., Clark, J. A., Fischer, T., and Oertel, M. (2019). Identifying a first-order phase transition in neutron star mergers through gravitational waves. *Phys. Rev. Lett.*, 122(6):061102.

[Baym et al., 1971] Baym, G., Pethick, C., and Sutherland, P. (1971). The ground state of matter at high densities: Equation of state and stellar models. *Astrophys. J.*, 170:299–317.

[Bejger et al., 2017] Bejger, M., Blaschke, D., Haensel, P., Zdunik, J. L., and Fortin, M. (2017). Consequences of a strong phase transition in the dense matter equation of state for the rotational evolution of neutron stars. *Astron. Astrophys.*, 600:A39.

[Berezhiani et al., 2003] Berezhiani, Z., Bombaci, I., Drago, A., Frontera, F., and Lavagno, A. (2003). Gamma-ray bursts from delayed collapse of neutron stars to quark matter stars. *Astrophys.J.*, 586:1250–1253.

[Bhattacharyya et al., 2005] Bhattacharyya, A., Ghosh, S. K., Hanauske, M., and Raha, S. (2005). Rotating twin stars and signature of quark-hadron phase transition. *Phys. Rev. C*, 71(4):048801.

[Bhattacharyya et al., 2017] Bhattacharyya, S., Bombaci, I., Logoteta, D., and Thampan, A. V. (2017). Two coexisting families of compact stars: observational implications for millisecond pulsars. *Astrophys. J.*, 848(1):65.

[Birkhan et al., 2017] Birkhan, J. et al. (2017). Electric dipole polarizability of ^{48}Ca and implications for the neutron skin. *Phys. Rev. Lett.*, 118(25):252501.

[Blaschke and Alvarez-Castillo, 2016] Blaschke, D. and Alvarez-Castillo, D. E. (2016). High-mass twins & resolution of the reconfinement, masquerade and hyperon puzzles of compact star interiors. *AIP Conf. Proc.*, 1701(1):020013.

[Blaschke et al., 2020] Blaschke, D., Alvarez-Castillo, D. E., Ayriyan, A., Grigorian, H., Lagarni, N. K., and Weber, F. (2020). *Astrophysical aspects of general relativistic mass twin stars*, pages 207–256.

[Blaschke and Cierniak, 2021] Blaschke, D. and Cierniak, M. (2021). Studying the onset of deconfinement with multi-messenger astronomy of neutron stars. *Astron. Nachr.*, 342(1-2):227–233.

[Bodmer, 1971] Bodmer, A. R. (1971). Collapsed nuclei. *Phys. Rev. D*, 4:1601.

[Boguta, 1981] Boguta, J. (1981). Density dependence of the single-particle potential in nuclear matter. *Physics Letters B*, 106(4):250–254.

[Boguta and Bodmer, 1977] Boguta, J. and Bodmer, A. R. (1977). Relativistic Calculation of Nuclear Matter and the Nuclear Surface. *Nucl. Phys.*, A292:413–428.

[Boguta and Stöcker, 1983] Boguta, J. and Stöcker, H. (1983). Systematics of Nuclear Matter Properties in a Nonlinear Relativistic Field Theory. *Physics Letters B*, 120(4-6):289–293.

[Bombaci et al., 2021] Bombaci, I., Drago, A., Logoteta, D., Pagliara, G., and Vidaña, I. (2021). Was gw190814 a black hole–strange quark star system? *Phys. Rev. Lett.*, 126:162702.

[Bombaci et al., 2009] Bombaci, I., Logoteta, D., Panda, P. K., Providencia, C., and Vidana, I. (2009). Quark matter nucleation in hot hadronic matter. *Phys. Lett. B*, 680:448–452.

[Bombaci et al., 2016] Bombaci, I., Logoteta, D., Vidaña, I., and Providência, C. (2016). Quark matter nucleation in neutron stars and astrophysical implications. *Eur. Phys. J. A*, 52(3):58.

[Bombaci et al., 2007] Bombaci, I., Lugones, G., and Vidana, I. (2007). Effects of color superconductivity on the nucleation of quark matter in neutron stars. *Astron. Astrophys.*, 462:1017–1022.

[Bombaci et al., 2008] Bombaci, I., Panda, P. K., Providencia, C., and Vidana, I. (2008). Metastability of hadronic compact stars. *Phys. Rev. D*, 77:083002.

[Bombaci et al., 2004] Bombaci, I., Parenti, I., and Vidana, I. (2004). Quark deconfinement and implications for the radius and the limiting mass of compact stars. *Astrophys. J.*, 614:314–325.

[Bonanno and Sedrakian, 2012] Bonanno, L. and Sedrakian, A. (2012). Composition and stability of hybrid stars with hyperons and quark color-superconductivity. *Astron.Astrophys.*, 539:A16.

[Cameron, 1959] Cameron, A. G. W. (1959). Neutron star models. *Astrophys. J.*, 130:884.

[Carbone and Schwenk, 2019] Carbone, A. and Schwenk, A. (2019). Ab initio constraints on thermal effects of the nuclear equation of state. *Phys. Rev. C*, 100(2):025805.

[Cerdá-Durán and Elias-Rosa, 2018] Cerdá-Durán, P. and Elias-Rosa, N. (2018). Neutron stars formation and Core Collapse Supernovae. *Astrophys. Space Sci. Libr.*, 457:1–56.

[Chen et al., 2011] Chen, H., Baldo, M., Burgio, G., and Schulze, H.-J. (2011). Hybrid stars with the Dyson-Schwinger quark model. *Phys.Rev.*, D84:105023.

[Chen and Piekarewicz, 2014] Chen, W.-C. and Piekarewicz, J. (2014). Building relativistic mean field models for finite nuclei and neutron stars. *Phys. Rev.*, C90(4):044305.

[Christian and Schaffner-Bielich, 2020] Christian, J.-E. and Schaffner-Bielich, J. (2020). Twin stars and the stiffness of the nuclear equation of state: ruling out strong phase transitions below $1.7n_0$ with the new NICER radius measurements. *Astrophys. J. Lett.*, 894(1):L8.

[Christian and Schaffner-Bielich, 2021] Christian, J.-E. and Schaffner-Bielich, J. (2021). Supermassive Neutron Stars Rule Out Twin Stars. *Phys. Rev. D*, 103(6):063042.

[Christian and Schaffner-Bielich, 2022] Christian, J.-E. and Schaffner-Bielich, J. (2022). Confirming the Existence of Twin Stars in a NICER Way. *Astrophys. J.*, 935(2):122.

[Christian et al., 2018] Christian, J.-E., Zacchi, A., and Schaffner-Bielich, J. (2018). Classifications of Twin Star Solutions for a Constant Speed of Sound Parameterized Equation of State. *Eur. Phys. J.*, A54(2):28.

[Christian et al., 2019] Christian, J.-E., Zacchi, A., and Schaffner-Bielich, J. (2019). Signals in the tidal deformability for phase transitions in compact stars with constraints from GW170817. *Phys. Rev.*, D99(2):023009.

[Coelho et al., 2010] Coelho, J., Lenzi, C., Malheiro, M., Marinho, R.M., J., and Fiolhais, M. (2010). Investigation of the existence of hybrid stars using Nambu-Jona-Lasinio models. *Int.J.Mod.Phys.*, D19:1521–1524.

[Coughlin et al., 2018] Coughlin, M. W. et al. (2018). Constraints on the neutron star equation of state from AT2017gfo using radiative transfer simulations. *Mon. Not. Roy. Astron. Soc.*, 480(3):3871–3878.

[Cromartie et al., 2019] Cromartie, H. T., E. Fonseca, S. M. R., and P. B. Demorest, e. a. (2019). Relativistic Shapiro delay measurements of an extremely massive millisecond pulsar. *Nat. Astron.*, 4(1):72–76.

[Damour and Nagar, 2009] Damour, T. and Nagar, A. (2009). Relativistic tidal properties of neutron stars. *Phys. Rev.*, D80:084035.

[Demorest et al., 2010] Demorest, P., Pennucci, T., Ransom, S., Roberts, M., and Hessels, J. (2010). Shapiro Delay Measurement of A Two Solar Mass Neutron Star. *Nature*, 467:1081–1083.

[Dexheimer et al., 2021] Dexheimer, V., Gomes, R. O., Klähn, T., Han, S., and Salinas, M. (2021). GW190814 as a massive rapidly rotating neutron star with exotic degrees of freedom. *Phys. Rev. C*, 103(2):025808.

[Di Clemente et al., 2022] Di Clemente, F., Drago, A., and Pagliara, G. (2022). Is the compact object associated with HESS J1731-347 a strange quark star?

[Doroshenko et al., 2022] Doroshenko, V., Suleimanov, V., Pühlhofer, G., and Santangelo, A. (2022). A strangely light neutron star within a supernova remnant. *Nature Astronomy*, 6:1444–1451.

[Drago et al., 2016] Drago, A., Lavagno, A., Pagliara, G., and Pigato, D. (2016). The scenario of two families of compact stars. *Eur. Phys. J.*, A52(2):40.

[Drago and Pagliara, 2016] Drago, A. and Pagliara, G. (2016). The scenario of two families of compact stars. *Eur. Phys. J.*, A52(2):41.

[Drago and Pagliara, 2018] Drago, A. and Pagliara, G. (2018). Merger of two neutron stars: predictions from the two-families scenario. *Astrophys. J.*, 852(2):L32.

[Drischler et al., 2016] Drischler, C., Carbone, A., Hebeler, K., and Schwenk, A. (2016). Neutron matter from chiral two- and three-nucleon calculations up to N^3LO. *Phys. Rev.*, C94(5):054307.

[Drischler et al., 2021] Drischler, C., Han, S., Lattimer, J. M., Prakash, M., Reddy, S., and Zhao, T. (2021). Limiting masses and radii of neutron stars and their implications. *Phys. Rev. C*, 103(4):045808.

[Duerr, 1956] Duerr, H.-P. (1956). Relativstic effects in nuclear forces. *Phys. Rev.*, 103:469.

[Duyvendak, 1942] Duyvendak, J. J. L. (1942). Further data bearing in the identification of the crab nebula with the supernova of 1054 a. d. part i. the ancient oriental chronicles. *Proc. Astr. Soc. Pac.*, 54:91.

[Evans et al., 2021] Evans, M. et al. (2021). A Horizon Study for Cosmic Explorer: Science, Observatories, and Community.

[Fattoyev, 2022] Fattoyev, F. (2022). private communication. Equations of state shared in the context of a different project.

[Fattoyev et al., 2020] Fattoyev, F. J., Horowitz, C. J., Piekarewicz, J., and Reed, B. (2020). GW190814: Impact of a 2.6 solar mass neutron star on the nucleonic equations of state. *Phys. Rev. C*, 102(6):065805.

[Fischer et al., 2018] Fischer, T., Bastian, N.-U. F., Wu, M.-R., Baklanov, P., Sorokina, E., Blinnikov, S., Typel, S., Klähn, T., and Blaschke, D. B. (2018). Quark deconfinement as a supernova explosion engine for massive blue supergiant stars. *Nature Astron.*, 2(12):980–986.

[Fischer et al., 2011] Fischer, T., Sagert, I., Pagliara, G., Hempel, M., Schaffner-Bielich, J., Rauscher, T., Thielemann, F.-K., Kappeli, R., Martinez-Pinedo, G., and Liebendörfer, M. (2011). Core-collapse supernova explosions triggered by a quark-hadron phase transition during the early post-bounce phase. *Astrophys. J. Suppl.*, 194:39.

[Flanagan and Hinderer, 2008] Flanagan, E. E. and Hinderer, T. (2008). Constraining neutron star tidal Love numbers with gravitational wave detectors. *Phys. Rev.*, D77:021502.

[Fonseca et al., 2016] Fonseca, E., Pennucci, T. T., Ellis, J. A., and other (2016). The NANOGrav Nine-year Data Set: Mass and Geometric Measurements of Binary Millisecond Pulsars. *Astrophys. J.*, 832(2):167.

[Fraga et al., 2002] Fraga, E. S., Pisarski, R. D., and Schaffner-Bielich, J. (2002). New class of compact stars at high density. *Nucl. Phys.*, A702:217–223.

[Furnstahl and Serot, 2000] Furnstahl, R. J. and Serot, B. D. (2000). Parameter counting in relativistic mean field models. *Nucl. Phys. A*, 671:447–460.

[Gandolfi et al., 2012] Gandolfi, S., Carlson, J., and Reddy, S. (2012). The maximum mass and radius of neutron stars and the nuclear symmetry energy. *Phys.Rev.*, C85:032801.

[Gendreau et al., 2012] Gendreau, K. C., Arzoumanian, Z., and Okajima, T. (2012). The Neutron star Interior Composition ExploreR (NICER): an Explorer mission of opportunity for soft x-ray timing spectroscopy. In Takahashi, T., Murray, S. S., and den Herder, J.-W. A., editors, *Society of Photo-Optical Instrumentation Engineers (SPIE) Conference Series*, volume 8443 of *Society of Photo-Optical Instrumentation Engineers (SPIE) Conference Series*, page 844313. International Society for Optics and Photonics, SPIE.

[Ghosh et al., 2022] Ghosh, S., Pradhan, B. K., Chatterjee, D., and Schaffner-Bielich, J. (2022). Multi-Physics Constraints at Different Densities to Probe Nuclear Symmetry Energy in Hyperonic Neutron Stars. *Front. Astron. Space Sci.*, 9:864294.

[Glendenning, 1985] Glendenning, N. K. (1985). Neutron stars are giant hypernuclei? *Astrophys. J.*, 293:470.

[Glendenning, 2000] Glendenning, N. K. (2000). *Compact Stars — Nuclear Physics, Particle Physics, and General Relativity*. Springer, New York, second edition.

[Glendenning and Kettner, 2000] Glendenning, N. K. and Kettner, C. (2000). Non-identical neutron star twins. *Astron. Astrophys.*, 353:L9.

[Godzieba et al., 2021] Godzieba, D. A., Radice, D., and Bernuzzi, S. (2021). On the maximum mass of neutron stars and GW190814. *Astrophys. J.*, 908(2):122.

[Gomes et al., 2019] Gomes, R. O., Dexheimer, V., Han, S., and Schramm, S. (2019). Can magnetic fields (de)stabilize twin stars? *Mon. Not. Roy. Astron. Soc.*, 485(4):4873–4877.

[Gong et al., 2001] Gong, Z., Zejda, L., Dappen, W., and Aparicio, J. M. (2001). Generalized Fermi-dirac functions and derivatives: properties and evaluation. *Comput. Phys. Commun.*, 136:294.

[Haensel et al., 1986] Haensel, P., Zdunik, J. L., and Schaeffer, R. (1986). Strange quark stars. *Astron. Astrophys.*, 160:121.

[Hagen et al., 2015] Hagen, G. et al. (2015). Neutron and weak-charge distributions of the ^{48}Ca nucleus. *Nature Phys.*, 12(2):186–190.

[Hebeler et al., 2013] Hebeler, K., Lattimer, J. M., Pethick, C. J., and Schwenk, A. (2013). EQUATION OF STATE AND NEUTRON STAR PROPERTIES CONSTRAINED BY NUCLEAR PHYSICS AND OBSERVATION. *The Astrophysical Journal*, 773(1):11.

[Hempel et al., 2016] Hempel, M., Heinimann, O., Yudin, A., Iosilevskiy, I., Liebendoerfer, M., and Thielemann, F.-K. (2016). Hot third family of compact stars and the possibility of core-collapse supernova explosions. *Phys. Rev.*, D94(10):103001.

[Hewish et al., 1968] Hewish, A., Bell, S. J., Pilkington, J. D. H., Scott, P. F., and Collins, R. A. (1968). Observation of a rapidly pulsating radio source. *Nature*, 217:709.

[Hinderer, 2008] Hinderer, T. (2008). Tidal Love numbers of neutron stars. *Astrophys. J.*, 677:1216–1220.

[Hinderer et al., 2010] Hinderer, T., Lackey, B. D., Lang, R. N., and Read, J. S. (2010). Tidal deformability of neutron stars with realistic equations of state and their gravitational wave signatures in binary inspiral. *Phys. Rev.*, D81:123016.

[Hobbs et al., 2012] Hobbs, G., Coles, W., Manchester, R. N., Keith, M. J., Shannon, R. M., Chen, D., Bailes, M., Bhat, N. D. R., Burke-Spolaor, S., Champion, D., Chaudhary, A., Hotan, A., Khoo, J., Kocz, J., Levin, Y., Oslowski, S., Preisig, B., Ravi, V., Reynolds, J. E., Sarkissian, J., van Straten, W., Verbiest, J. P. W., Yardley, D., and You, X. P. (2012). Development of a pulsar-based time-scale. *Mon. Not. R. Astron. Soc.*, 427:2780–2787.

[Hornick et al., 2018] Hornick, N., Tolos, L., Zacchi, A., Christian, J.-E., and Schaffner-Bielich, J. (2018). Relativistic parameterizations of neutron matter and implications for neutron stars. *Phys. Rev.*, C98(6):065804.

[Horowitz and Piekarewicz, 2001] Horowitz, C. J. and Piekarewicz, J. (2001). The neutron radii of lead and neutron stars. *Phys. Rev.*, C64:062802.

[Hulse and Taylor, 1975] Hulse, R. A. and Taylor, J. H. (1975). Discovery of a pulsar in a binary system. *Astrophys. J.*, 195:L51–L53.

[Huth et al., 2022] Huth, S. et al. (2022). Constraining Neutron-Star Matter with Microscopic and Macroscopic Collisions. *Nature*, 606:276–280.

[Itoh, 1970] Itoh, N. (1970). Hydrostatic Equilibrium of Hypothetical Quark Stars. *Prog.Theor.Phys.*, 44:291.

[Ivanenko and Kurdgelaidze, 1965] Ivanenko, D. D. and Kurdgelaidze, D. F. (1965). Hypothesis concerning quark stars. *Astrophys.*, 1:251.

[Jakobus et al., 2021] Jakobus, P., Motornenko, A., Gomes, R. O., Steinheimer, J., and Stoecker, H. (2021). The possibility of twin star solutions in a model based on lattice QCD thermodynamics. *Eur. Phys. J. C*, 81(1):41.

[Jiang et al., 2022] Jiang, J.-L., Ecker, C., and Rezzolla, L. (2022). Bayesian analysis of neutron-star properties with parameterized equations of state: the role of the likelihood functions.

[Johnson and Teller, 1955] Johnson, M. H. and Teller, E. (1955). Classical field theory of nuclear forces. *Phys. Rev.*, 98:783–787.

[Kämpfer, 1981] Kämpfer, B. (1981). On stabilizing effects of relativity in cold spheric stars with a phase transition in the interior. *Phys. Lett.*, 101B:366–368.

[Kämpfer, 1981] Kämpfer, B. (1981). On the Possibility of Stable Quark and Pion Condensed Stars. *J.Phys.*, A14:L471–L475.

[Keller et al., 2022] Keller, J., Hebeler, K., and Schwenk, A. (2022). Nuclear equation of state for arbitrary proton fraction and temperature based on chiral effective field theory and a Gaussian process emulator.

[Kochankovski et al., 2022] Kochankovski, H., Ramos, A., and Tolos, L. (2022). Equation of state for hot hyperonic neutron star matter. *Mon. Not. Roy. Astron. Soc.*, 517(1):507–517.

[Kurkela et al., 2014] Kurkela, A., Fraga, E. S., Schaffner-Bielich, J., and Vuorinen, A. (2014). Constraining neutron star matter with QCD.

[Landau, 1932] Landau, L. D. (1932). On the theory of stars. *Physik. Zeits. Sowjetunion*, 1:285.

[Landry and Chakravarti, 2022] Landry, P. and Chakravarti, K. (2022). Prospects for constraining twin stars with next-generation gravitational-wave detectors.

[Lattimer, 2023] Lattimer, J. M. (2023). Constraints on Nuclear Symmetry Energy Parameters. *Particles*, 6:30–56.

[Lattimer and Lim, 2013] Lattimer, J. M. and Lim, Y. (2013). Constraining the Symmetry Parameters of the Nuclear Interaction. *Astrophys.J.*, 771:51.

[Li and Han, 2013] Li, B.-A. and Han, X. (2013). Constraining the neutron-proton effective mass splitting using empirical constraints on the density dependence of nuclear symmetry energy around normal density. *Phys. Lett.*, B727:276–281.

[Lighthill, 1950] Lighthill, M. J. (1950). On the instability of small planetary cores (II). *Mon. Not. Roy. Astron. Soc.*, 110:339.

[LIGO Collaboration, 2023] LIGO Collaboration (2023). Latest update on start of next observing run (o4).

[Lim et al., 2021] Lim, Y., Bhattacharya, A., Holt, J. W., and Pati, D. (2021). Radius and equation of state constraints from massive neutron stars and GW190814. *Phys. Rev. C*, 104(3):L032802.

[Machleidt and Entem, 2011] Machleidt, R. and Entem, D. R. (2011). Chiral effective field theory and nuclear forces. *Phys. Rept.*, 503:1–75.

[Maggiore et al., 2020] Maggiore, M. et al. (2020). Science Case for the Einstein Telescope. *JCAP*, 03:050.

[Martinez et al., 2015] Martinez, J. G., Stovall, K., Freire, P. C. C., Deneva, J. S., Jenet, F. A., McLaughlin, M. A., Bagchi, M., Bates, S. D., and Ridolfi, A. (2015). Pulsar J0453+1559: A Double Neutron Star System with a Large Mass Asymmetry. *Astrophys. J.*, 812(2):143.

[Maslov et al., 2019] Maslov, K., Yasutake, N., Ayriyan, A., Blaschke, D., Grigorian, H., Maruyama, T., Tatsumi, T., and Voskresensky, D. N. (2019). Hybrid equation of state with pasta phases and third family of compact stars. *Phys. Rev. C*, 100(2):025802.

[Masuda et al., 2013] Masuda, K., Hatsuda, T., and Takatsuka, T. (2013). Hadron-Quark Crossover and Massive Hybrid Stars with Strangeness. *Astrophys. J.*, 764:12.

[Mendes et al., 2022] Mendes, M., Fattoyev, F. J., Cumming, A., and Gale, C. (2022). Fast Neutrino Cooling in the Accreting Neutron Star MXB 1659-29. *Astrophys. J.*, 938(2):119.

[Miller et al., 2021] Miller, M. C. et al. (2021). The Radius of PSR J0740+6620 from NICER and XMM-Newton Data. *Astrophys. J. Lett.*, 918(2):L28.

[Miller et al., 2019] Miller, M. C., Lamb, F. K., Dittmann, A. J., et al. (2019). PSR J0030+0451 Mass and Radius from NICER Data and Implications for the Properties of Neutron Star Matter. *Astrophys. J. Lett.*, 887:L24.

[Mintz et al., 2010] Mintz, B. W., Fraga, E. S., Pagliara, G., and Schaffner-Bielich, J. (2010). Nucleation of quark matter in protoneutron star matter. *Phys. Rev.*, D81:123012.

[Montana et al., 2019] Montana, G., Tolos, L., Hanauske, M., and Rezzolla, L. (2019). Constraining twin stars with GW170817. *Phys. Rev. D*, 99(10):103009.

[Most et al., 2019] Most, E. R., Papenfort, L. J., Dexheimer, V., Hanauske, M., Schramm, S., Stöcker, H., and Rezzolla, L. (2019). Signatures of quark-hadron phase transitions in general-relativistic neutron-star mergers. *Phys. Rev. Lett.*, 122(6):061101.

[Most et al., 2020] Most, E. R., Papenfort, L. J., Weih, L. R., and Rezzolla, L. (2020). A lower bound on the maximum mass if the secondary in GW190814 was once a rapidly spinning neutron star. *Mon. Not. Roy. Astron. Soc.*, 499(1):L82–L86.

[Most et al., 2018] Most, E. R., Weih, L. R., Rezzolla, L., and Schaffner-Bielich, J. (2018). New constraints on radii and tidal deformabilities of neutron stars from GW170817. *Phys. Rev. Lett.*, 120(26):261103.

[Mueller and Serot, 1996] Mueller, H. and Serot, B. D. (1996). Relativistic mean field theory and the high density nuclear equation of state. *Nucl. Phys.*, A606:508–537.

[Müller et al., 2019] Müller, B., Tauris, T. M., Heger, A., Banerjee, P., Qian, Y. Z., Powell, J., Chan, C., Gay, D. W., and Langer, N. (2019). Three-Dimensional Simulations of Neutrino-Driven Core-Collapse Supernovae from Low-Mass Single and Binary Star Progenitors. *Mon. Not. Roy. Astron. Soc.*, 484(3):3307–3324.

[Nathanail et al., 2021] Nathanail, A., Most, E. R., and Rezzolla, L. (2021). GW170817 and GW190814: tension on the maximum mass. *Astrophys. J. Lett.*, 908(2):L28.

[Negele and Vautherin, 1973] Negele, J. W. and Vautherin, D. (1973). Neutron star matter at subnuclear densities. *Nucl. Phys.*, A207:298–320.

[Nieder et al., 2020] Nieder, L. et al. (2020). Discovery of a Gamma-ray Black Widow Pulsar by GPU-accelerated Einstein@Home. *Astrophys. J.*, 902(2):L46.

[Nunes et al., 2020] Nunes, R. C., Coelho, J. G., and de Araujo, J. C. N. (2020). Weighing massive neutron star with screening gravity: a look on PSR J0740 + 6620 and GW190814 secondary component. *Eur. Phys. J. C*, 80(12):1115.

[Oertel et al., 2017] Oertel, M., Hempel, M., Klahn, T., and Typel, S. (2017). Equations of state for supernovae and compact stars. *Rev. Mod. Phys.*, 89(1):015007.

[Oppenheimer and Volkoff, 1939] Oppenheimer, J. R. and Volkoff, G. M. (1939). On massive neutron cores. *Phys. Rev.*, 55:374.

[Ozel and Freire, 2016] Ozel, F. and Freire, P. (2016). Masses, radii, and the equation of state of neutron stars. *Annu. Rev. Astron. Astrophys.*, 54(1):401–440.

[Ozel et al., 2012] Ozel, F., Psaltis, D., Narayan, R., and Villarreal, A. S. (2012). On the Mass Distribution and Birth Masses of Neutron Stars. *Astrophys. J.*, 757:55.

[Pang et al., 2021] Pang, P. T. H., Tews, I., Coughlin, M. W., Bulla, M., Van Den Broeck, C., and Dietrich, T. (2021). Nuclear Physics Multimessenger Astrophysics Constraints on the Neutron Star Equation of State: Adding NICER's PSR J0740+6620 Measurement. *Astrophys. J.*, 922(1):14.

[Paschalidis et al., 2018] Paschalidis, V., Yagi, K., Alvarez-Castillo, D., Blaschke, D. B., and Sedrakian, A. (2018). Implications from GW170817 and I-Love-Q relations for relativistic hybrid stars. *Phys. Rev.*, D97(8):084038.

[Pili et al., 2016] Pili, A. G., Bucciantini, N., Drago, A., Pagliara, G., and Del Zanna, L. (2016). Quark deconfinement in the proto-magnetar model of long gamma-ray bursts. *Mon. Not. Roy. Astron. Soc.*, 462(1):L26–L30.

[Postnikov et al., 2010] Postnikov, S., Prakash, M., and Lattimer, J. M. (2010). Tidal Love Numbers of Neutron and Self-Bound Quark Stars. *Phys. Rev.*, D82:024016.

[Pradhan et al., 2023] Pradhan, B. K., Chatterjee, D., Gandhi, R., and Schaffner-Bielich, J. (2023). Role of vector self-interaction in neutron star properties. *Nucl. Phys. A*, 1030:122578.

[Raaijmakers et al., 2021] Raaijmakers, G., Greif, S. K., Hebeler, K., Hinderer, T., Nissanke, S., Schwenk, A., Riley, T. E., Watts, A. L., Lattimer, J. M., and Ho, W. C. G. (2021). Constraints on the Dense Matter Equation of State and Neutron Star Properties from NICER's Mass–Radius Estimate of PSR J0740+6620 and Multimessenger Observations. *Astrophys. J. Lett.*, 918(2):L29.

[Raaijmakers et al., 2019] Raaijmakers, G., Riley, T. E., Watts, A. L., et al. (2019). A NICER view of PSR J0030+0451: Implications for the dense matter equation of state. *Astrophys. J. Lett.*, 887:L22.

[Radice et al., 2018] Radice, D., Perego, A., Zappa, F., and Bernuzzi, S. (2018). GW170817: Joint Constraint on the Neutron Star Equation of State from Multimessenger Observations. *Astrophys. J.*, 852(2):L29.

[Regge and Wheeler, 1957] Regge, T. and Wheeler, J. A. (1957). Stability of a Schwarzschild singularity. *Phys. Rev.*, 108:1063–1069.

[Riley et al., 2021] Riley, T. E. et al. (2021). A NICER View of the Massive Pulsar PSR J0740+6620 Informed by Radio Timing and XMM-Newton Spectroscopy. *Astrophys. J. Lett.*, 918(2):L27.

[Riley et al., 2019] Riley, T. E., Watts, A. L., Bogdanov, S., et al. (2019). A NICER View of PSR J0030+0451: Millisecond Pulsar Parameter Estimation. *Astrophys. J. Lett.*, 887:L21.

[Roca-Maza et al., 2015] Roca-Maza, X., Viñas, X., Centelles, M., Agrawal, B. K., Colo', G., Paar, N., Piekarewicz, J., and Vretenar, D. (2015). The neutron skin thickness from the measured electric dipole polarizability in ^{68}Ni, ^{120}Sn, and ^{208}Pb. *Phys. Rev.*, C92:064304.

[Romani et al., 2022] Romani, R. W., Kandel, D., Filippenko, A. V., Brink, T. G., and Zheng, W. (2022). PSR J0952−0607: The Fastest and Heaviest Known Galactic Neutron Star. *Astrophys. J. Lett.*, 934(2):L18.

[Rosenfeld, 1974] Rosenfeld, L. (1974). Discussion of the report of d. pines. In *Astrophysics and Gravitation: Proceedings of the Sixteenth Solvay Conference on Physics*, Bruxelles. Editions de l'Université Bruxelles.

[Sagert et al., 2006] Sagert, I., Hempel, M., Greiner, C., and Schaffner-Bielich, J. (2006). Compact stars for undergraduates. *Eur.J.Phys.*, 27:577–610.

[Sagert et al., 2009] Sagert, I., Hempel, M., Pagliara, G., Schaffner-Bielich, J., Fischer, T., Mezzacappa, A., Thielemann, F.-K., and Liebendörfer, M. (2009). Signals of the QCD phase transition in core-collapse supernovae. *Phys. Rev. Lett.*, 102:081101.

[Schaffner-Bielich, 2020] Schaffner-Bielich, J. (2020). *Compact Star Physics*. Cambridge University Press.

[Schaffner-Bielich et al., 2002] Schaffner-Bielich, J., Hanauske, M., Stöcker, H., and Greiner, W. (2002). Phase transition to hyperon matter in neutron stars. *Phys. Rev. Lett.*, 89:171101.

[Schertler et al., 2000] Schertler, K., Greiner, C., Schaffner-Bielich, J., and Thoma, M. H. (2000). Quark phases in neutron stars and a 'third family' of compact stars as a signature for phase transitions. *Nucl. Phys.*, A677:463.

[Seidov, 1971] Seidov, Z. (1971). The Stability of a Star with a Phase Change in General Relativity Theory. *Sov. Astron, 15 (347)*.

[Serot and Walecka, 1986] Serot, B. D. and Walecka, J. D. (1986). The Relativistic Nuclear Many Body Problem. *Adv. Nucl. Phys.*, 16:1–327.

[Shirke et al., 2022] Shirke, S., Ghosh, S., and Chatterjee, D. (2022). Constraining the equation of state of hybrid stars using recent information from multidisciplinary physics.

[Shlomo et al., 2006] Shlomo, S., Kolomietz, V. M., and Colò, G. (2006). Deducing the nuclear-matter incompressibility coefficient from data on isoscalar compression modes. *Europ. Phys. J A*, 30(1):23–30.

[Sieniawska et al., 2019] Sieniawska, M., Turczanski, W., Bejger, M., and Zdunik, J. L. (2019). Tidal deformability and other global parameters of compact stars with strong phase transitions. *Astron. Astrophys.*, 622:A174.

[Skyrme, 1958] Skyrme, T. (1958). The effective nuclear potential. *Nuclear Physics*, 9(4):615–634.

[Suwa et al., 2018] Suwa, Y., Yoshida, T., Shibata, M., Umeda, H., and Takahashi, K. (2018). On the minimum mass of neutron stars. *Mon. Not. Roy. Astron. Soc.*, 481(3):3305–3312.

[Tan et al., 2020] Tan, H., Noronha-Hostler, J., and Yunes, N. (2020). Neutron Star Equation of State in light of GW190814. *Phys. Rev. Lett.*, 125(26):261104.

[Tews et al., 2018] Tews, I., Margueron, J., and Reddy, S. (2018). Critical examination of constraints on the equation of state of dense matter obtained from GW170817. *Phys. Rev.*, C98(4):045804.

[Tews et al., 2021] Tews, I., Pang, P. T. H., Dietrich, T., Coughlin, M. W., Antier, S., Bulla, M., Heinzel, J., and Issa, L. (2021). On the Nature of GW190814 and Its Impact on the Understanding of Supranuclear Matter. *Astrophys. J. Lett.*, 908(1):L1.

[Thorne, 1998] Thorne, K. S. (1998). Tidal stabilization of rigidly rotating, fully relativistic neutron stars. *Phys. Rev.*, D58:124031.

[Todd-Rutel and Piekarewicz, 2005] Todd-Rutel, B. G. and Piekarewicz, J. (2005). Neutron-Rich Nuclei and Neutron Stars: A New Accurately Calibrated Interaction for the Study of Neutron-Rich Matter. *Phys. Rev. Lett.*, 95:122501.

[Tolman, 1939] Tolman, R. C. (1939). Static solutions of einstein's field equations for spheres of fluid. *Phys. Rev.*, 55:364.

[Tolos et al., 2017a] Tolos, L., Centelles, M., and Ramos, A. (2017a). Equation of State for Nucleonic and Hyperonic Neutron Stars with Mass and Radius Constraints. *Astrophys. J.*, 834(1):3.

[Tolos et al., 2017b] Tolos, L., Centelles, M., and Ramos, A. (2017b). The Equation of State for the Nucleonic and Hyperonic Core of Neutron Stars. *Publ. Astron. Soc. Austral.*, 34:e065.

[Tootle et al., 2022] Tootle, S., Ecker, C., Topolski, K., Demircik, T., Järvinen, M., and Rezzolla, L. (2022). Quark formation and phenomenology in binary neutron-star mergers using V-QCD. *SciPost Phys.*, 13:109.

[Tsaloukidis et al., 2022] Tsaloukidis, L., Koliogiannis, P. S., Kanakis-Pegios, A., and Moustakidis, C. C. (2022). Twin stars as probes of the nuclear equation of state: effects of rotation through the PSR J0952-0607 pulsar and constraints via the tidal deformability from the GW170817 event.

[Tsokaros et al., 2020] Tsokaros, A., Ruiz, M., and Shapiro, S. L. (2020). GW190814: Spin and equation of state of a neutron star companion. *Astrophys. J.*, 905(1):48.

[Typel et al., 2010] Typel, S., Röpke, G., Klähn, T., Blaschke, D., and Wolter, H. H. (2010). Composition and thermodynamics of nuclear matter with light clusters. *Phys. Rev.*, C81:015803.

[Walecka, 1974] Walecka, J. D. (1974). A theory of highly condensed matter. *Ann. Phys. (N.Y.)*, 83:491.

[Watts et al., 2016] Watts, A. L. et al. (2016). Colloquium : Measuring the neutron star equation of state using x-ray timing. *Rev. Mod. Phys.*, 88(2):021001.

[Weih et al., 2020] Weih, L. R., Hanauske, M., and Rezzolla, L. (2020). Postmerger gravitational-wave signatures of phase transitions in binary mergers. *Phys. Rev. Lett.*, 124:171103.

[Wystub et al., 2021] Wystub, S., Dengler, Y., Christian, J.-E., and Schaffner-Bielich, J. (2021). Constraining exotic compact stars composed of bosonic and fermionic dark matter with gravitational wave events.

[Yakovlev et al., 2012] Yakovlev, D., Haensel, P., Baym, G., and Pethick, C. (2012). Lev landau and the concept of neutron stars. *Physics-Uspekhi*, 56.

[Yasutake et al., 2014] Yasutake, N., Lastowiecki, R., Benic, S., Blaschke, D., Maruyama, T., and Tatsumi, T. (2014). Finite-size effects at the hadron-quark transition and heavy hybrid stars. *Phys.Rev.*, C89(6):065803.

[Zacchi et al., 2016] Zacchi, A., Hanauske, M., and Schaffner-Bielich, J. (2016). Stable hybrid stars within a SU(3) Quark-Meson-Model. *Phys. Rev.*, D93(6):065011.

[Zacchi et al., 2015] Zacchi, A., Stiele, R., and Schaffner-Bielich, J. (2015). Compact stars in a SU(3) Quark-Meson Model. *Phys. Rev.*, D92(4):045022.

[Zacchi et al., 2017] Zacchi, A., Tolos, L., and Schaffner-Bielich, J. (2017). Twin Stars within the SU(3) Chiral Quark-Meson Model. *Phys. Rev.*, D95(10):103008.

[Zdunik and Haensel, 2013] Zdunik, J. and Haensel, P. (2013). Maximum mass of neutron stars and strange neutron-star cores. *Astron.Astrophys.*, 551:A61.

[Zdunik et al., 2006] Zdunik, J. L., Bejger, M., Haensel, P., and Gourgoulhon, E. (2006). Phase transitions in rotating neutron stars cores: back bending, stability, corequakes and pulsar timing. *Astron. Astrophys.*, 450:747–758.

[Zhang and Li, 2020] Zhang, N.-B. and Li, B.-A. (2020). GW190814's secondary component with mass $(2.50 - 2.67)\ M_\odot$ as a super-fast pulsar. *Astrophys. J.*, 902(1):38.

[Zhang and Chen, 2022] Zhang, Z. and Chen, L.-W. (2022). Bayesian Inference of the Symmetry Energy and the Neutron Skin in ^{48}Ca and ^{208}Pb from CREX and PREX-2.